NTNU – Trondheim
Norwegian University of
Science and Technology

The Effect of Magnetic Field and Sulphide-Pollution on Corrosion Behaviour of Nickel-Aluminium Bronze in Seawater

Marte Sørtveit Mørkve

Preface

The present work has been written in the course TMT4900 as a part of the Master`s degree programme at the Department of Materials Science and Engineering at the Norwegian University of Science and Technology. Professor II Otto Lunder and Professor Roy Johnsen have supervised the work together with Ph.D Hedda Nordby Krogstad. The experimental work has been performed at the SINTEF and NTNU Corrosion Laboratory between February 2015 and May 2015.

I would like to thank both of my supervisors, Professor II Otto Lunder and Professor Roy Johnsen, for guidance and help during this project. A special thanks goes to Professor Roy Johnsen for being available for questions and discussion whenever needed.

My gratitude goes to Ph. D Hedda Nordby Krogstad for helping me in the lab and supporting me when problems have occurred. Thank you for many useful discussions and for sharing your knowledge throughout this project.

Further, I would like to thank Christian Lauritsen and my family for their support throughout the semester. Finally, a big thank you goes to all my co-students for making five years at NTNU memorable.

_____

Marte Sørtveit Mørkve
Trondheim, 12/6-15

Abstract

The objective with this work was to investigate the corrosion behaviour of nickel-aluminium bronze (NAB) in both pure and sulphide-polluted seawater, and possible synergy effects with an applied magnetic field (MF).

Two different test setups were used for electrochemical measurements in this work, i.e. with and without a MF. A MF in the range of 0,15-0,28 Tesla was applied. The corrosion testing included open circuit potential (OCP) measurements, linear polarization resistance (LPR) and potentiodynamic polarization curves under a range of experimental conditions. pH measurements were performed to support the observations from OCP measurements. The sulphide-polluted test solution was made by adding $Na_2S \cdot xH_2O$ to synthetic seawater (SSW). Sulphide contents of 1, 10 and 100 ppmW were investigated in this work. After ended test period, some samples were subjected to macroscopic and microscopic surface characterization by 3D light microscope, scanning electron microscope (SEM) and energy dispersive X-ray spectroscopy (EDS) analysis. X-ray diffraction (XRD) was used for characterization of corrosion products. Long-term experiments were performed in the Sealab at Brattøra, while all other tests were done at the SINTEF and NTNU Corrosion Laboratory.

The results from OCP measurements revealed an increase in the potential to more positive values in the presence of sulphide. The MF had limited effect on OCP for fresh NAB in both pure SSW and sulphide-polluted SSW, while the OCP of long-term NAB shifted to more negative values in the presence of a MF. A protective oxide layer was developed on the surface of NAB after nine weeks of immersion in natural seawater, and the corrosion current density was found to be 1,5 mA/m^2. The corrosion rate was calculated to be 33 times higher for fresh NAB compared to long-term NAB in unpolluted seawater. A higher corrosion rate was calculated for fresh NAB in the presence of a MF. However, the limiting cathodic current density decreased when a MF was applied. The addition of sulphide to SSW accelerated the rate of charge transfer of oxygen reduction reaction. Several corrosion craters were observed beneath the corrosion products after immersion in 10 ppmW sulphide-polluted SSW.

Sammendrag

Formålet med denne oppgaven var å undersøke korrosjonsegenskapene til nikkel-aluminium bronse (NAB) i både rent og sulfidforurenset sjøvann, og mulige synergieffekter med et påført magnetfelt (MF).

To ulike testoppsett ble brukt for elektrokjemiske målinger i dette arbeidet, det vil si med og uten et magnetfelt. Styrken på det påførte magnetfeltet var 0,15-0,28 Tesla. Korrosjonstesting inkluderte måling av åpen krets potensial (OCP), lineær polarisasjonsmotstand (LPR) og potensiodynamiske polarisasjonskurver ved ulike eksperimentelle forhold. Målinger av pH ble utført for å støtte observasjonene fra OCP målinger. Sulfidforurenset testløsning ble laget ved å tilsette $Na_2S \cdot xH_2O$ til syntetisk sjøvann (SSW). Sulfidinnhold på 1, 10 og 100 ppmW ble undersøkt i dette arbeidet. Etter testperioden ble noen prøver utsatt for makroskopisk og mikroskopisk overflatekarakterisering ved 3D lysmikroskop, scanning elektronmikroskop og EDS-analyse. Røntgendiffraksjon ble brukt for å karakterisere korrosjonsprodukter. Langtidsforsøkene ble utført i Sealab på Brattøra, mens samtlige andre tester ble gjort på SINTEF og NTNU korrosjonslaboratorium.

Resultater fra OCP målingene viste en økning i potensial til mer positive verdier i nærvær av sulfid. Magnetfeltet hadde ingen påvirkning på OCP til fersk NAB verken i rent SSW eller i sulfidforurenset SSW, mens OCP for langtids NAB ble endret til mer negative verdier under påvirkning av et MF. Et beskyttende oksidlag ble utviklet på overflaten til NAB etter ni uker i naturlig sjøvann, og korrosjonsstrømtettheten ble funnet til å være 1,5 mA/m². Korrosjonshastigheten ble beregnet til å være 33 ganger høyere for fersk NAB i forhold til langtids NAB. En høyere korrosjonshastighet ble beregnet for fersk NAB i nærvær av et MF. Midlertidig avtok den begrensende katodiske strømtettheten når et MF ble påført. Tilsetting av sulfid til SSW akselererte hastigheten av ladningsoverføring av oksygen-reduksjonsreaksjonen. Det ble observert flere korrosjonskrater under korrosjonsprodukter etter neddykking i 10 ppmW sulfidforurenset SSW.

Table of contents

Abbreviations and symbols

	Unit	Explanation
A	m^2	Area
Ag/AgCl	-	Silver/silver chloride reference electrode
b	V/decade	Tafel slope constant
B	Tesla	External magnetic field
∇B	Tesla	Magnetic field gradient
bcc	-	Body-centred cubic
C	mole/cm^3	Concentration
CE	-	Counter electrode
cph	-	Closed packed hexagonale
CR	mm/year	Corrosion rate
D	cm^2/s	Diffusion coefficient
E	mV	Potential
EDS	-	Energy dispersive X-ray spectroscopy
EHT	kV	Accelerating voltage
F	C/mole	Faradays constant
fcc	-	Face-centred cubic
HB	-	Brinell hardness scale
i	mA/m^2	Current density
i$_{corr}$	mA/m^2	Corrosion current density
i$_{lim}$	mA/m^2	Limiting current density
I	mA	Current
IPM	-	Department of Engineering Design and Materials
J	C/cm^2	Flux of ions
LPR	-	Linear polarization resistance
M	g/mole	Molar mass
MF	-	Magnetic field
MHD	-	Magnetohydrodynamic
n	-	Number of electrons
$Na_2S \cdot xH_2O$	-	Sodium sulphide hydrate
NAB	-	Nickel-aluminium bronze
OCP	-	Open circuit potential

ρ	g/cm^3	Density
ppmW	-	Parts per million by weight
R	Ω	Resistance
R$_p$	Ωm^2	Polarization resistance
REF	-	Reference electrode
SE	-	Secondary electron
SEM	-	Scanning electron microscopy
SFE	-	Stacking fault energy
SHE	-	Standard hydrogen electrode
SSW	-	Synthetic seawater
SW	-	Seawater
XRD	-	X-ray diffraction
WD	-	Working distance
WE	-	Working electrode
δ	cm	Thickness of Nernst diffusion layer
χ_m	H/m	Magnetic permeability
μ_0	-	Magnetic susceptibility

1 Introduction

1.1 Background

Nickel-aluminium bronze (NAB) is a copper-based alloy with high strength and toughness, along with good corrosion resistance. The corrosion resistance in seawater rely on the formation of an adherent, protective surface film [1]. Due to its many favourable properties, NAB is widely used in seawater service [2]. The alloy shows excellent resistance towards corrosion fatigue and cavitation, and is for that reason frequently used in marine propeller, pumps and valves [3]. However, NAB has proven to suffer minor selective phase corrosion under crevices, and severe corrosion has been observed in the presence of sulphide-pollution [2].

Associated with an industrial application, a component of NAB is exposed to seawater, in the presence of a strong magnetic field (MF). Recently, severe corrosion attacks have been observed at this component. The component is galvanic connected to stainless steel without any cathodic protection, and exposed to sulphide-polluted seawater in e.g. polluted harbours during outfitting of ships. The component is continuously exposed to a MF generated by permanent magnets. NAB has been used for the same purpose in seawater, but in the absence of an applied MF, without suffering from corrosion.

The observed, accelerated corrosion of NAB may be due to magnetic forces, sulphide-pollution, galvanic contact or synergy effects. Sulphide-pollution in seawater is not uncommon, and it is well known that this will affect the corrosion properties of copper alloys, as sulphides react with the protective oxide layer [4]. The effect of magnetic forces on corrosion mechanism of NAB is still a relatively unexplored area, and needs further investigation.

1.2 Aim of work

In this work, the corrosion behaviour of NAB will be investigated based on available literature and own results from experimental work. The evaluation of experimental results

will include corrosion rates and properties of corroded surfaces, performed by linear polarization resistance, potentiodynamic polarization curves and surface characterization under a range of experimental conditions.

The main objective of this project is to understand the corrosion mechanism of NAB, exposed in both pure and sulphide-polluted seawater, with and without an applied MF. The galvanic corrosion of NAB when connected to a more noble metal and seawater flow will not be investigated due to limited time. This work will especially focus on the possible synergy effects between sulphide-pollution and a MF.

2 Theoretical background

The first part of this chapter provides relevant theory of NAB. An introduction to NAB is presented and then, the microstructure and properties of the alloy are described. The second part of this chapter presents literature related to corrosion and other degradation mechanisms of NAB in seawater, followed by corrosion in sulphide-polluted seawater. The last part contains theory related to MF, and the influence of magnetic forces on the mechanism of corrosion.

2.1 Microstructure and properties

2.1.1 Introduction to nickel-aluminium bronze

NAB typically contains 80 % copper, 10 % aluminium and 5 % each of iron and nickel [1, 2]. This alloy is most commonly used for production of valves, large propellers and pumps, due to its excellent resistance towards cavitation damage [3, 5]. In clean, turbulent seawater NAB offers a good combination of high mechanical strength and low general corrosion rate of 0,06 mm/year [2]. NAB is for that reason widely used in seawater service. The corrosion resistance rely on the formation of a thin, protective layer of corrosion products that prevents further attack. NAB shows higher resistance towards cavitation, erosion-corrosion and corrosion fatigue compared with other copper alloys, but is prone to minor selective phase attack under crevices [3]. Its properties are due to the alloying elements, which will be discussed later in this section. Some mechanical properties of NAB are listed in Table 2.1. The values given in the table are minimum values.

Table 2.1 Mechanical properties of NAB [6].

Mechanical properties	Values
Tensile strength [N/mm^2]	650
Yield strength [N/mm^2]	250
Elongation [%]	18
Hardness [HB]	140

2.1.2 Microstructure of nickel-aluminium bronze

NAB is an alloy with complex microstructure, consisting of a copper-rich α-matrix with several intermetallic κ-phases [1, 2]. Figure 2.1 presents the phases normally found in sound NAB casting. The various phases have dissimilar corrosion potential, due to different chemical composition. The phases and chemical composition of NAB can vary significantly between samples but also within the same sample [7].
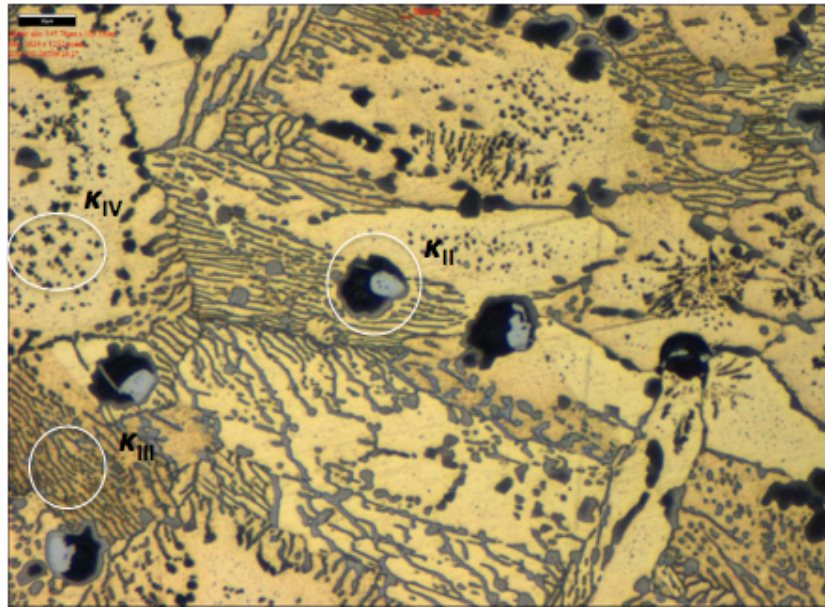
Figure 2.1 Illustration of a typical microstructure in sound NAB casting, showing the α-matrix with intermetallic κ particles. κ_I particles, γ-2 phase, β- phases are not shown.

The α- phase

The α-phase is a copper-rich solid solution with a face-centred cubic (fcc) crystal structure, containing up to 8 % aluminium and some dissolved nickel, iron and manganese [1, 7, 8]. The chemical composition remains quite constant with temperature except of the iron content, which reduces with temperature as the κ-phases precipitates. The α-phase increases the ductility of the alloy [1]. The α-phase appears bright in Figure 2.1.

The β- phase

The β-phase is a high temperature phase having a body-centred cubic (bcc) crystal structure, and contributes to higher tensile strength and is less ductile than the α-phase [1]. This phase has a high content of aluminium, and if quenched from high temperature the phase is retained as martensitic β phase. But if the cooling rate is slower, the β phase decomposes into fine eutectoid of $\alpha + \kappa$, as seen in Figure 2.2. Details about the κ phases will be further discussed later in this section.
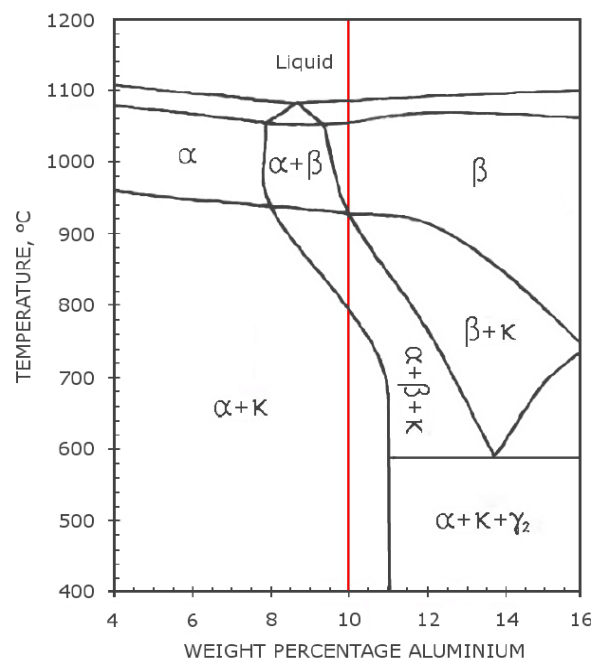
Figure 2.2 Phase diagram of Cu-Al-Fe-Ni [1]. The red line represents 10 % aluminium.

The martensite β- phase

Martensite β-phase, or retained β-phase, is the result of β-phase as it cools to room temperature. This phase has a closed packed hexagonal (cph) crystal structure, and is quite anodic to the α-phase due to the higher content of aluminium [1]. It is for that reason detrimental to the corrosion properties. The martensite β-phase is not present in Figure 2.1.

The γ-2 phase

The γ-2 phase is an aluminium-rich phase based on Cu_9Al_4, and is prone to corrosion due to its high content of aluminium. This phase is hard and brittle, which makes it detrimental to the mechanical properties of the alloy [1, 9]. By controlling the composition and cooling rate,

the formation of γ-2 phase can be avoided [10]. This phase is normally not found in NAB with 10 % aluminium, and is not present in Figure 2.1.

The κ-phases

The κ-phases are intermetallic particles that precipitate from the molten material upon cooling, having different shape, size and chemical composition [11]. The κ phases adsorb aluminium from the matrix, increasing the amount of aluminium that can be added to the alloy without the risk of formation of undesired γ-2 phase [12]. In addition, the κ phases increase the mechanical strength without markedly reducing the ductility. The $\alpha + \kappa$ alloy has the best combination of tensile strength, proof strength and elongation. It also gives excellent corrosion resistance, as it is free of the martensite β and γ-2 phase. There exist four different κ phases, named κ_I, κ_{II}, κ_{III} and κ_{IV}, according to the order they precipitate in the molten material upon cooling. They are distinguishable by a combination of morphology, location and distribution in the microstructure [1, 7]. The κ precipitates are based on either Fe$_3$Al or NiAl, except from the κ_I phase that might be FeAl or a disordered structure. Both the Fe$_3$Al and NiAl structure have an ordered bcc crystal structure [1].

The κ_I particles are the first solid precipitation in the molten material upon cooling. If the iron content exceeds 5%, the κ_I particles act as nucleation points for the α matrix upon cooling. They grow into large, dendritic shaped rosettes in the range of 20-50 μm, and are located at the centre of the α-grains [1]. However, κ_I particles are normally not found if the iron content is lower than 4,5 % or in heat-treated NAB castings [1, 2]. The κ_I particles are not present in Figure 2.1.

The κ_{II} particles take the form as dendritic rosettes, but are smaller than the κ_I particles. They are normally in the range of 5-10 μm in size, and based on bcc structure of Fe$_3$Al with nickel and copper substituting for iron. The κ_{II} particles can be observed as dark rosettes in Figure 2.1.

The κ_{III} particles precipitate when the remaining β-phase decomposes into a fine eutectoid of $\alpha + \kappa_{III}$. This phase has lamellar or globular form, and grows normal to the α/β boundary or at the κ_I boundary. The structure is based on NiAl with iron and copper substituting for nickel [1]. The κ_{III} particles can be seen as dark lamellar in Figure 2.1.

The κ_{IV} particles precipitate as fine particles ($<2\ \mu m$) within the α grains if the cooling rate is sufficiently slow. The structure is based on Fe$_3$Al [1]. The κ_{IV} particles can be seen as dark, fine particles within the α matrix in Figure 2.1.

2.1.3 The role of alloying elements

The properties of NAB are due to the addition of alloying elements, such as aluminium, iron and nickel. Aluminium and iron are primarily responsible for the mechanical properties of the alloy, while nickel mainly improves the corrosion resistance [1].

Aluminium is the main alloying element in NAB, and contributes to higher tensile strength, resulting in higher resistance towards cavitation and erosion [10]. In addition, the excellent corrosion resistance is a result of the adherent, aluminium-rich layer, which is highly protective to the underlying metal. The main effect of nickel is to improve the corrosion resistance, but it also contributes to strength and toughness. Improving the corrosion resistance is a result of the precipitation of NiAl (κ_{III}) from the β-phase. The presence of κ_{III} extends the $\alpha + \kappa$ field to higher content of aluminium, as seen in Figure 2.2. The relationship of nickel to aluminium content decides if the γ-2 phase may be avoided, which is possible if the rule given in Equation (2.1) is fulfilled [1]:

$$Al \leq 8,2 + \frac{Ni}{2} \qquad\qquad \textbf{(2.1)}$$

However, no further advantages arise from increasing the nickel content above 5 %.

The presence of iron refines the structure of NAB and tends to break up any γ-2 formed into a discontinuous form [3]. Addition of iron also contributes to the precipitation of intermetallic Fe$_3$Al particles, resulting in increased strength and hardness of the $\alpha + \kappa$ alloy. No further advantages occur from increasing the iron content above 4,5 %, and too high iron content may reduce the resistance towards cavitation damages [1].

2.2 Corrosion of nickel-aluminium bronze

Corrosion is an electrochemical process, comprising an anodic and a cathodic reaction, which occurs when alloys or metals are in contact with an electrolyte. The metal will dissolve into metal ions at the anode, and corrosion may for that reason be described as a metal attack [13]. In unpolluted and aerated seawater, the anodic dissolution of NAB is associated with the formation of cuprous ions, Cu^+, as shown in Equation (2.2). The reduction of oxygen is the predominant cathodic reaction, and can be seen in Equation (2.3) [7, 10, 14].

$$Cu\ (s) \rightarrow Cu^+\ (aq) +\ e^- \qquad\qquad \textbf{(2.2)}$$

$$O_2(g) + 2H_2O(l) + 4e^- \rightarrow 4OH^-(aq) \qquad\qquad \textbf{(2.3)}$$
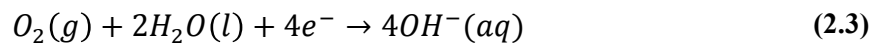
The corrosion resistance of NAB rely on the formation of an adherent, protective surface film, and is discussed further in the next section. However, NAB has proven not to be immune to corrosion. The corrosion process of NAB may be described as selective phase corrosion, which is caused by the difference in electrochemical potential of the various phases [5]. This might occur under crevices, beneath marine growth, deposits or in galvanic contact, but the corrosion attack will be minimal as long as the alloy is free of γ-2 phase [3]. The difference in electrochemical potential between the phases may vary, and is in excess of 100 mV between the α phase and γ_2 phase [1].

2.2.1 The formation of a protective oxide layer

The corrosion resistance of copper alloys in seawater rely on the ability to form an adherent, protective oxide film. The Pourbaix diagram for pure copper in seawater at 25 °C is shown in Figure 2.3.
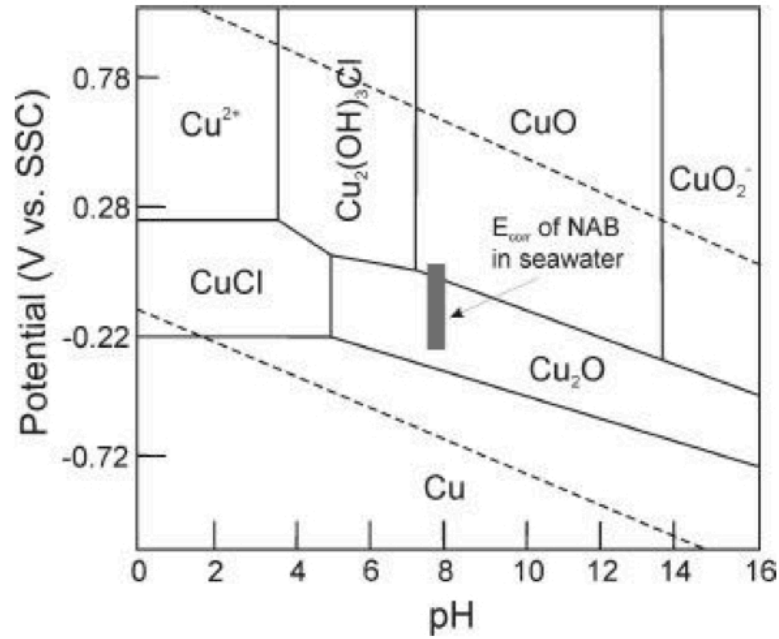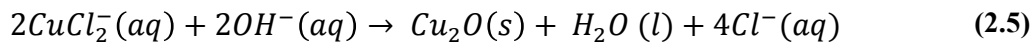
Figure 2.3 Pourbaix diagram for pure copper in seawater at 25 °C [14].

This Pourbaix diagram shows that cuprous oxide, Cu_2O, is the most stable oxide at -210 mV vs Ag/AgCl, which is OCP of NAB, in seawater with a pH of value 8,2 [14]. The formation of Cu_2O is shown in Equation (2.4) and (2.5):

$$Cu\ (s) +\ 2\ Cl^-(aq)\ \rightarrow CuCl_2^-\ (aq) +\ e^- \qquad \textbf{(2.4)}$$

$$2CuCl_2^-(aq) + 2OH^-(aq) \rightarrow\ Cu_2O(s) +\ H_2O\ (l) + 4Cl^-(aq) \qquad \textbf{(2.5)}$$
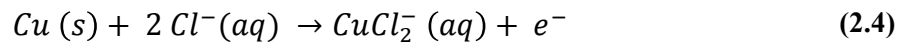
As the oxide film grows, the diffusion through it becomes difficult due to an ohmic drop across the oxide film, resulting in the transformation of cuprous oxide to cupric oxide, CuO [14]. This can be seen in Equation (2.6):

$$Cu_2O\ (s) +\ H_2O\ (l) \rightarrow 2CuO\ (s) + 2H^+\ (aq) + 2e^- \qquad \textbf{(2.6)}$$
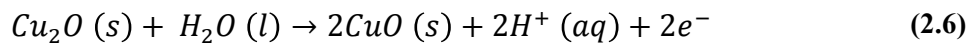
After longer exposure times in seawater a green corrosion product of $Cu_2(OH)_3Cl$, called atacamite, might be formed on the surface outside the Cu_2O film [15], according to Equation (2.7):

$$Cu_2O\ (s) +\ 2H_2O\ (l) + Cl^-\ (aq) \rightarrow\ Cu_2(OH)_3Cl\ (s) + H^+\ (aq) + 2e^- \qquad \textbf{(2.7)}$$
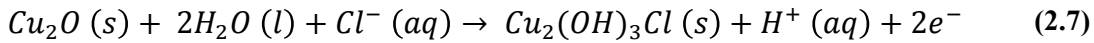
The protective oxide film on NAB has been reported to consist of both aluminium oxide and copper oxides [1]. The formation of aluminium oxide, Al_2O_3, can be seen in Equation (2.8) [16]:

$$2Al\ (s) + 3H_2O(l)\ \rightarrow\ Al_2O_3(aq) + 6H^+(aq) + 6e^- \qquad \textbf{(2.8)}$$

The oxide layer is aluminium-rich adjacent to the bare metal, while the outer part mainly consists of copper oxides [1]. Aluminium will oxidize preferentially, and when the formation of Al_2O_3 is completed, preferential oxidation of copper occurs at the surface of the corrosion pr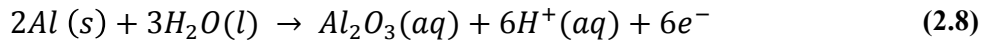oducts. This results in a double oxide layer. The aluminium oxide hampers the ionic transport across the corrosion layer, and hence decreases the anodic reaction rate. The copper oxides reduce the rate of charge transfer, and hence decrease the rate of cathodic reaction [17].

In fresh seawater the protective oxide layer forms rapidly and protects the underlying metal against corrosion, reducing the corrosion rate by a factor of 20-30 [17]. The oxide layer has been reported to be in order of 900-1000 nm thick [7]. The time for the oxide layer to fully develop depends on the temperature of the seawater [18]. If damage occurs on an existing oxide layer, or the formation of the layer is inhibited, the bare metal will be exposed to seawater and corrosion may propagate. Damages may arise because of mechanically attack such as cavitation, erosion and corrosion fatigue, or chemically attack caused by sulphides.

2.2.2 Cavitation and erosion

Cavitation may be described as the formation and collapse of gas bubbles resulting from localized pressure changes in the liquid. The gas bubbles are formed in the liquid in regions where the pressure in the liquid drops to or below its vapour pressure. As the bubbles are subjected to a higher pressure, they collapse producing a shock wave that may damage the material by fatigue [3, 8, 19, 20], as illustrated in Figure 2.4. Cavitation normally occurs in components where the liquid is being driven trough at high velocities, such as propellers or

valves [8]. The damage associated with cavitation is due to a combination of corrosion and mechanical forces [3].

The oxide layer may be damaged by the collapse of bubbles causing a continuous formation of fresh surfaces. The bare metal exposed to seawater may suffer from corrosion, causing a shift in the corrosion potential of NAB towards the active direction, i.e. in the positive direction. The anodic and cathodic current of NAB were reported to increase by an order of magnitude in the presence of cavitation [19]. However, the damage caused by corrosion is relatively small compared with the damage caused by the collapse of bubbles.
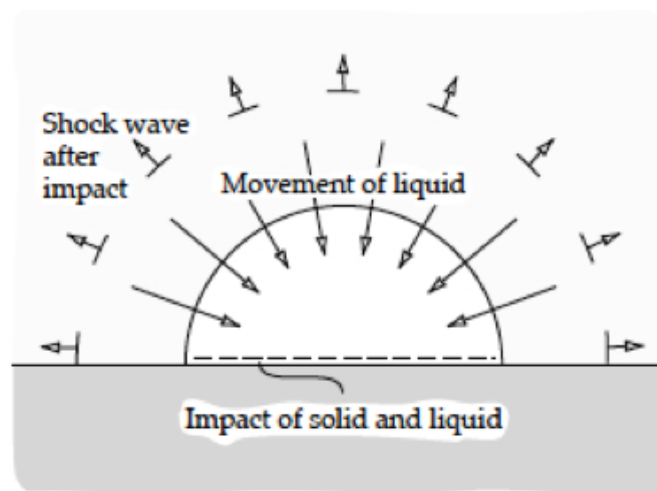
Figure 2.4 Mechanism of bubble collapses, resulting in a shock wave of liquid [21].

The resistance towards cavitation erosion of aluminium bronzes increases with the content of aluminium, due to higher hardness and lower stacking fault energy (SFE) [20]. The relation between SFE and content of aluminium is illustrated in Figure 2.5. For materials with low SFE, cross-slip become more difficult, resulting in less mobility for the dislocations. The strength of a material is inversely related to dislocations mobility, i.e. the strength of the material increases with less mobility of the dislocations [22]. Zhang and Fang reported that the resistance towards cavitation erosion is favoured by high ultimate resilience, high strain energy, high hardness, high fatigue limit and high ductility [20].
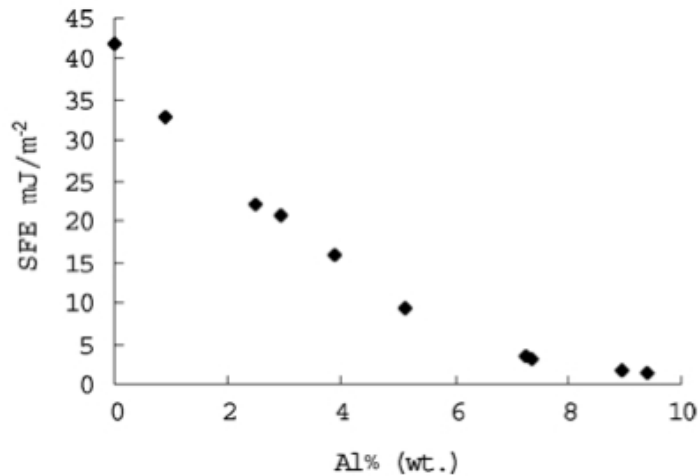
Figure 2.5 The relation between SFE and content of aluminium (wt. %) in aluminium bronzes [20].

The critical flow velocity to avoid erosion of NAB is 20-25 m/s in clean seawater, but if any solid particles are present, this value will be reduced [18]. Seawater flowing over a surface creates a shear stress [23]. If the shear stress is higher than the binding force between the metal and a protective surface film, the film will be removed, locally exposing bare metal [1, 24]. The critical flow velocity depends on the size and concentration of abrasive particles and the geometry of the component [18]. The impingement angle is also important for the erosion rate of a material [25]. NAB is a ductile material, i.e. the worst impingement angle is 20-30 °[21]. Large iron-rich κ_I and κ_{II} precipitates may contribute to cavitation damage, while small κ_{III} and κ_{IV} precipitates can provide the resistance towards cavitation erosion [1].

2.2.3 Localized corrosion

Copper alloys are generally susceptible to localized corrosion in the presence of pollutants such as sulphides and ammonia [26]. The effect of sulphide-pollution on corrosion properties of NAB will be further discussed in the next section. Crevice and pitting corrosion of NAB may occur when coupled to a more noble alloy, but can be avoided by cathodic protection [1, 3, 5]. Marine growth or other deposits on the surface of the metal may create a crevice. In natural seawater, the crevice corrosion rate of NAB has been reported to be in the range of 0,7-1,0 mm/year compared with 0,25 mm/year for stainless steel [7]. Localized corrosion occurs when an oxide film exist on the surface.

The corrosion of NAB takes form as selective phase corrosion attack [7]. In seawater with a pH value of 8,2 the α-phase is initially anodic to the κ_{III} (NiAl) phase, and will corrode preferentially at the α/κ_{III} interface. Corrosion initiates over the whole surface as shown in Figure 2.6, but low corrosion rate has been reported [1]. As corrosion products are formed on the surface of NAB, a pitting-like mechanism occurs under the corrosion deposits, as illustrated in Figure 2.7.
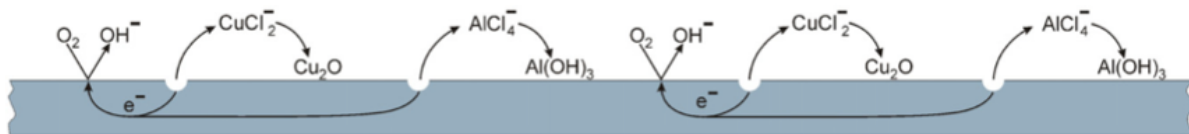
Figure 2.6 Schematic illustration of the initiation of corrosion of NAB inside and outside a crevice [7].
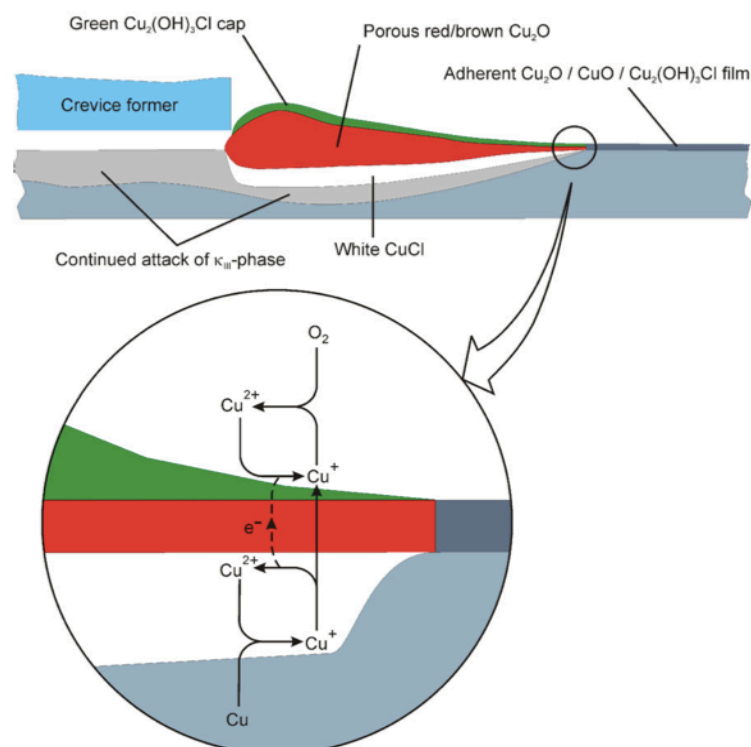

Figure 2.7 Schematic illustration of a pitting-like mechanism of NAB under corrosion deposits [7].

The corrosion products, consisting of copper and aluminium ions, undergo hydrolysis in contact with seawater, resulting in a local acid environment. When the pH falls to 3, the κ_{III} phase, rich in aluminium, becomes anodic to the copper rich α-phase and corrodes

13

preferentially. The corrosion rate has been reported to be in the range of 0,7-1,1 mm/year [1]. The corrosion products have been suggested to consist of CuCl, CuO, Cu_2O and $Cu_2(OH)_3Cl$, which are ordered in a layered structure, as seen in Figure 2.7. The white CuCl covers the pit interior, keeping the concentration of copper ions low, due to the low solubility of CuCl [7]. A red, porous layer of Cu_2O forms on the top of the CuCl layer, working as a membrane across the mouth of the pit. The outside surface will act as a cathode, while the inside surface as an anode. The cathodic reactions are the reduction of cupric ions and oxygen, while the anodic reaction is the oxidation of cuprous ions to cupric ions [27]. The corrosion rate increases with the potential difference between the outside and inside surface of the pit [1]. The pit is reported to grow peripherally rather than laterally, contrary to the mechanisms of stainless steels [7].

Figure 2.8 a) and b) show SEM images of selective corrosion of the α-phase and κ_{III} phase, respectively.

a)   b)
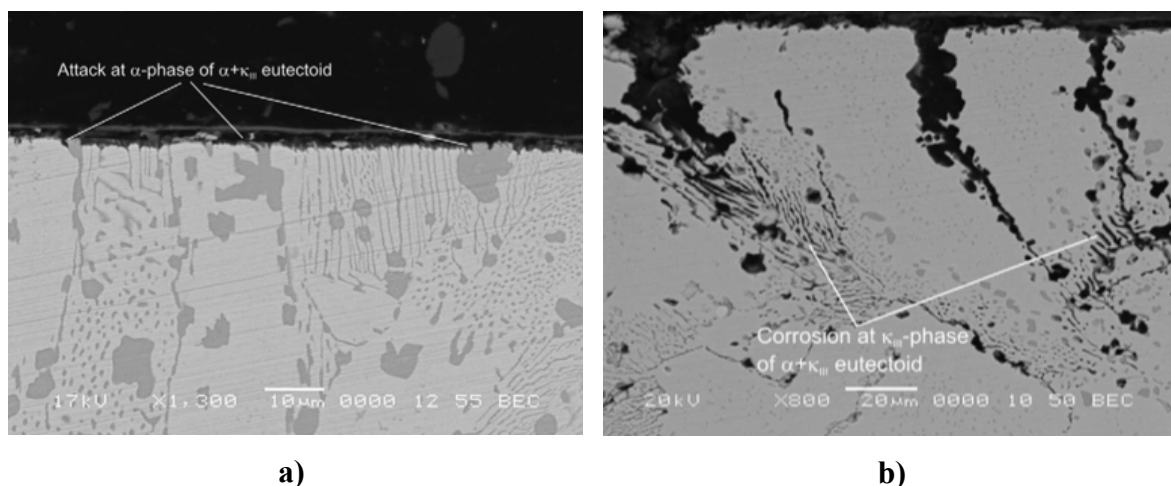
Figure 2.8 SEM images of a) corroded α-phase in the $\alpha + \kappa_{III}$ eutectoid after one month immersion in 3,5 % NaCl solution, and b) corroded κ_{III} phase in the $\alpha + \kappa_{III}$ eutectoid after 6,5 months immersion in 3,5 % NaCl solution [7].

### 2.2.4 Corrosion fatigue

Corrosion fatigue is a result of repeated imposition of cyclic stress below those that would cause failure under constant load, and depends on both the corrosion resistance and the mechanical strength of the material. In corrosive environments, the cyclic stress level before failure is reduced [3]. Ship propellers and pumps are subjected to corrosion fatigue [23]. NAB

has high resistance towards corrosion fatigue both under high frequency and low frequency loading conditions [3].

2.2.5 Sulphide-pollution

Sulphide-pollution in seawater arises from either decomposing of organic matter or from industrial waste charge. It may also occur when the seawater conditions support the growth of sulphate reducing bacteria [4, 18, 28]. Stagnant conditions tend to increase the possibility for sulphide-pollution. It is well known that copper alloys corrode at accelerated rates in sulphide-polluted seawater. The sulphides are powerful reducing agents and may interfere with the protective oxide layer on the metal, to form a porous layer mainly consisting of copper sulphide [1, 4]. The overall reaction between sulphide and copper can be seen in Equation (2.9) [29]:

$$4Cu(s) + 2S^{2-}(aq) + O_2(g) + 2H_2O(l) \rightarrow 2Cu_2S\,(s) + 4OH^-(aq) \qquad \textbf{(2.9)}$$
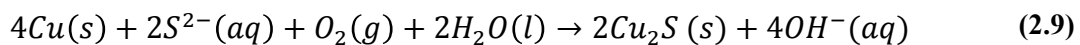
The Cu_2S layer is poorly adhered to the metal surface compared to the oxide layer formed in clean seawater, resulting in an increase in corrosion rate. It will also easily erode away when subjected to high flow rates [1].

The main effect of copper sulphide is to increase the rate of charge transfer of the oxygen reduction reaction that occurs on the surface of the corrosion layer. As a result, the overall corrosion rate is controlled by diffusion of reaction species to the electrode surface, and depends strongly on the flow velocity [4]. The corrosion behaviour of NAB in sulphide-polluted seawater depends on the content of dissolved oxygen. Maximum corrosion rates of NAB are measured for fresh surfaces exposed in aerated and sulphide-polluted seawater [30]. The formation of Cu_2S reduces the concentration of free copper ions in the electrolyte, giving an active shift in the corrosion potential, e.g. in the positive direction [4].

When NAB, covered by a Cu_2S layer, is transferred to fresh and aerated seawater, the porous copper sulphide layer will be replaced by an oxide film with time [30]. However, the Cu_2S layer needs to be totally removed from the surface before the corrosion rate decreases to normal values obtained in fresh seawater. This has been reported to take up to 9 days [23].

For NAB propellers, a Cu_2S layer may arise in e.g. polluted seawater in harbours during outfitting and start-up periods. When the ships travel into fresh and aerated seawater the corrosion rate of NAB will be very high until a protective, oxide layer is formed.

2.3 Magnetic field

A MF may affect electrochemical reactions by altering the rates of both charge transfer and mass transport [31]. The effect of a MF on mass transport is more frequently reported in the literature compared to charge transfer. The understanding of how a MF affects corrosion mechanism is still a subject under discussion. Some authors claim that a MF can reduce the corrosion rate [32], while others claim that it increases the corrosion rate [31, 33]. To understand how a MF interferes with mass transport and charge transfer, it is necessary to look at the typical forces acting in aqueous electrolyte, listed in Table 2.2.

Table 2.2 Typical forces acting in aqueous electrolytes with and without an applied MF [34].

Force	Typical value $[N/m^3]$
Driving force for diffusion	10^{10}
Driving force for electromigration	10^{10}
Driving force for convection	10^5
Driving force for natural convection	10^3
Paramagnetic force	10^4
Field gradient force	10^1
Lorentz force	10^3
Electrokinetic force	10^3
Magnetic damping force	10^1

The four first forces in Table 2.2 are dominating in the absence of a MF. The five last forces are only present when a MF is applied, and may be responsible for the observed effects of a MF. The paramagnetic and field gradient force depend on magnetic properties of the electrolyte, while the others are related to the movement of charged particles [34]. The Lorentz force is the most documented one, and will be further explained in the next section, together with the field gradient force. The magnetic damping force becomes significant when

the conductivity exceeds $\sim 10^6 \, S/m$, and is negligible in aqueous electrolytes with low conductivity. The conductivity of aqueous solutions is in the order of $\sim 10^2$, and the magnetic damping force will for that reason not be further described [34]. The electrokinetic force is not discussed further either, as it is only referred to in one of the cited references in this report. The paramagnetic force will not be discussed in this report, as the significant contribution of the magnetic forces are from the Lorentz force and the field gradient force [35]. It is worth to notice that the typical values of the magnetic forces in Table 2.2 are very small compared to the forces of migration and diffusion.

### 2.3.1 The effect of magnetic forces on mass transport

It is well known that a MF may induce convection in the electrolyte in an electrochemical cell. The Lorentz force, called the magnetohydrodynamic (MHD) force from now, is capable of moving charged particles in both non-uniform and uniform applied MF, and is the main contribution to changes in the convection. This effect is called the magnetohydrodynamic phenomena, and arises from interaction between a MF and moving charges [36]. The MHD force is described by the Lorentz equation given in Equation (2.10).

$$\boldsymbol{F}_{MHD} = \boldsymbol{J} \times \boldsymbol{B} \qquad\qquad (2.10)$$

where $\boldsymbol{J}$ is the flux of ions (C/cm^2) and $\boldsymbol{B}$ is the external MF (Tesla).

The magnitude of the MHD force, $\boldsymbol{F}_{MHD}$, depends on the strength and orientation of the MF, as illustrated in Figure 2.9. If the electrode is oriented orthogonal to the MF, the MHD force causes rotation in the plane of the electrode surface, while if oriented parallel to the MF, the MHD force is directed to one side of the electrode [35]. The parallel configuration is the worst scenario with respect to the corrosion rate, because the MHD force will supply fresh electrolyte to the electrode surface, and hence increases the corrosion current. In the orthogonal configuration, the MHD force causes a cyclotron-like fluid flow near the electrode surface. This does not bring fresh electrolyte to the surface, and will not increase the current [35]. The MHD force may for that reason be neglected in the perpendicular orientation [37].
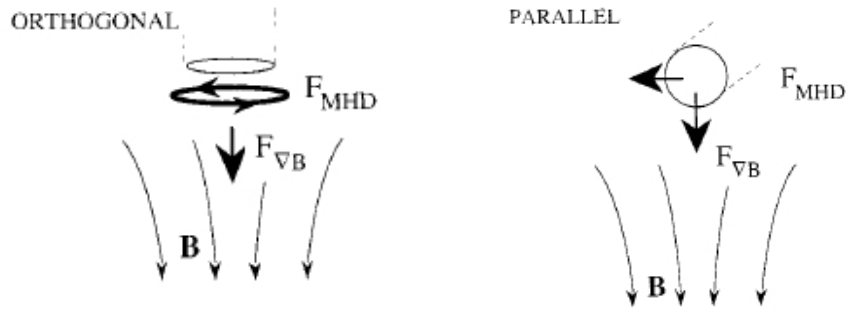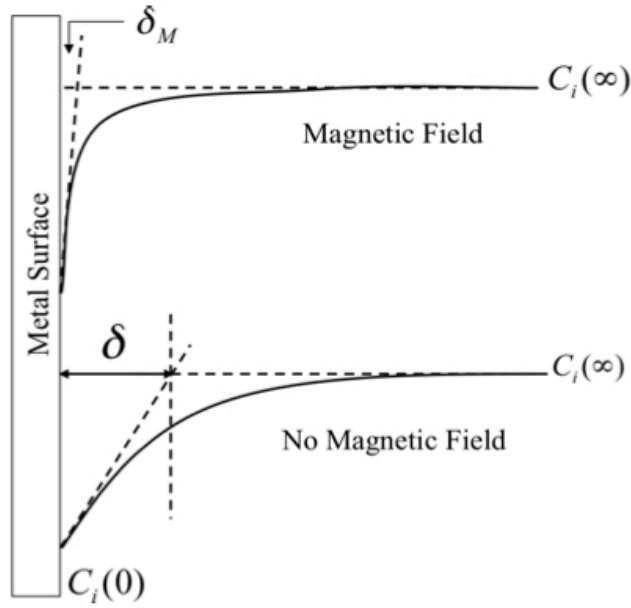
Figure 2.9 Schematic illustration of the direction of the MHD force, F$_{MHD}$, and the field gradient force, $F_{\nabla B}$, in two different configurations, e.g. orthogonal and parallel [35].

The field gradient force, F$_{\nabla B}$, is absent in a uniform MF where $\nabla B = 0$ [34, 35]. As seen in Figure 2.9, the field gradient force is independent of the orientation of the MF with respect to the electrode. The force is directed downward away from the electrode surface in both the parallel and perpendicular configuration. The field gradient force is in order of 10 N/m^3, which is only 1 % of the MHD force, as shown in Table 2.2. The field gradient force is expressed by Equation (2.11):

$$\boldsymbol{F}_{\nabla B} = \frac{\chi_m c \boldsymbol{B} \nabla B}{\mu_0} \qquad\qquad \textbf{(2.11)}$$

where χ_m is the magnetic susceptibility, ∇B is the magnetic field gradient, c is concentration, μ_0 is magnetic permeability and $\boldsymbol{B}$ is the external MF. This force describes the tendencies of paramagnetic and diamagnetic molecules to move towards or away from regions of higher strength of the MF, respectively [35].

The induced convection adjacent to the electrode surface reduces the thickness of the Nernst diffusion layer, δ, as illustrated in Figure 2.10.

Figure 2.10 Schematic illustration of how a MF interferes with mass transport. The thickness of the Nernst diffusion layer, δ, decreases when a MF is applied due to the increased convection [38].

According to Equation (2.12), the limiting current density, i_{lim}, is inversely proportional to the thickness of the Nernst diffusion layer [39]. As a result, the limiting current density is increased in the presence of a MF and may cause changes in the kinetics of the electrochemical system.

$$i_{lim} = -\frac{nFD_R C_{Rb}}{\delta} \qquad (2.12)$$

where n is the number of electrons transferred, F is Faradays constant, D_R is the diffusion coefficient of reactant, C_{Rb} is the bulk concentration of reactant and δ is the thickness of the Nernst diffusion layer [39]. The effect of an external MF is strongest when the electrochemical system is mass transfer controlled [38, 40].

2.3.2 The effect of magnetic forces on charge transfer

The effect of a MF on charge transfer reactions is still a subject of controversy. Several authors state that a MF will interfere with charge transfer [31, 41], while others state that it will not [42]. No available literature related to copper alloys on the effect of MF on charge transfer reactions was found.

Kelly states that the rate of charge transfer reactions may be altered due to interactions between the interfacial potential difference at the metal/electrolyte interface and the MF [31]. Kelly performed experiments on an electrochemical system including titanium immersed in H_2-saturated 1 M H_2SO_4 solution. Both the anodic dissolution of titanium and reduction of hydrogen were under activation control. The author observed that the dissolution of titanium increased maximum by a factor of 2,5 when exposed to a MF [31].

Devos et.al performed electrochemical impedance spectroscopy on different electrochemical systems exposed to a homogeneous MF under charge transfer, mass transfer and mixed control. The author's observed no influence of a MF on the charge transfer reaction, for MF up to 1 Tesla and parallel configuration [42].

Lu and Yang measured the open circuit potential, OCP, of an iron electrode immersed in acidic and neutral aqueous solutions when imposing a MF of 0,4 Tesla. They observed a positive shift in OCP in both the acidic and neutral solutions, the shift being more pronounced in acidic solution. When the MF was removed, the OCP shifted to more negative values in acidic solution. An applied MF had a strong effect on the hydrogen reaction, while the oxygen reduction was reported to not be effected [41]. In 1 M KNO_3 solution, OCP was reported to increase with 60 mV and 200 mV in the positive direction for zinc and iron, respectively [43]. Contrary, the OCP of Nd-Fe-B magnets in aerated 3,5 wt% NaCl was reported to shift in the negative direction when they were magnetized [44].

3 Experimental work

The objective with the experimental work was to study the corrosion behaviour of NAB in sulphide-polluted seawater, in the presence of an applied MF. This section provides material specification of the tested material and presents the experimental procedures and test setups. The experimental work consisted of OCP measurements, linear polarization resistance (LPR) and potentiodynamic polarization curves, under a range of experimental conditions. Surface characterization was performed after ended test period, by 3D optical microscope, scanning electron microscope (SEM) and energy dispersive X-ray spectroscopy (EDS). X-ray diffraction (XRD) was used for characterization of corrosion products.

3.1 Test materials and sample preparation

In this work, samples of NAB with dimensions of approximately 35x35x2 mm, was used as test material in all the experiments. The chemical composition of the NAB is shown in Table 3.1 and mechanical properties are given in the Material Datasheet in Appendix A. Square samples were machined from a propeller supplied by Brunvoll in Molde at the workshop at the Department of Engineering Design and Materials (IPM). All the samples contained a hole in one of the corner, where a platinum wire was connected to give electrical connection. For samples used in tests with an applied MF, a welding rod was preferred instead of a platinum wire, due to its stiffness. The welding rod was mounted onto the NAB samples. An isolation sock and silicon were used to prevent galvanic effects and direct contact with the seawater. This sample preparation was also done for the samples placed in Sealab. Figure 3.1 shows photos of prepared specimens.

Prior to corrosion testing, the samples were grinded with $600 \, \mu m$ SiC grit paper. All the samples were subjected to the same cleaning procedure before immersion, which included cleaning in water and ethanol followed by air-drying.

Table 3.1 Chemical composition of cast NAB used in the experimental work [6].

| Element	Min wt %	Max wt %
Al	9,0	10
Cr	-	0,005
Cu	79,0	81,5
Fe	4,0	5,0
Mg	-	0,04
Mn	0,5	1,0
Ni	4,5	5,5
Pb	-	0,02
Si	-	0,05
Sn	-	0,08
Zn	-	0,2

a)   b)

Figure 3.1 The pictures show a) test specimen with rod mounted onto the upper end for electrical connection and b) test specimen with a platinum wire mounted onto the upper corner for electrical connection. The test specimen in a) was used for long-term experiments in Sealab, and for tests in the presence of a MF.

3.2 Reference electrode

A silver-silver chloride electrode (Ag/AgCl), immersed in a saturated potassium chloride (KCl) solution, was used as a reference electrode in all experiments in this work. The reaction in the reference electrode is given in Equation (3.1):

$$AgCl\ (s) +\ e^- \leftrightarrow Ag\ (s) +\ Cl^-\ (aq) \tag{3.1}$$
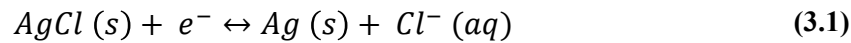
All potentials mentioned in this report are with respect to the Ag/AgCl reference electrode, and its potential is approximately $+199\ mV_{SHE}$[45]. A tube filled with test solution and a cotton string established electrical connection between the test solution and the reference electrode.

3.3 Test solution

Synthetic seawater

Synthetic seawater (SSW) was used as test solution for experiments performed in the SINTEF and NTNU Corrosion laboratory, later called Corrosion Lab in this report. Its preparation was in accordance with ASTM D 1141 [46], and the chemical composition is given in Table 3.2. A standard pH meter (PHM 92, Radiometer Copenhagen) was used for pH measurements of the test solution. The pH-measuring electrode was calibrated with reference solutions prior to use. The pH of SSW was approximately 7,9 during the test period. The temperature of the test solution was kept at room temperature, 21 °C $\pm$ 2 °C, during the period of experiment.

In another part of the work, a sulphide-polluted test solution was used. This was made by adding $Na_2S \cdot xH_2O$ to SSW to give the desired sulphide content, resulting in a slightly basic test solution. In this work, the content of sulphide is given in parts per million by weight (ppmW).

Natural seawater

Circulating, natural seawater in the Sealab at Brattøra was used for long-term experiments. Natural seawater was pumped from 80-metre depth in the Trondheim fjord into a container where the samples were placed. The temperature of the seawater was approximately $10\,°C$ during the test period. The container hold in excess of 300 litre seawater, and the continuous replacement was 2,4 litre/min.

Table 3.2 Chemical composition of the SSW used in the experimental work [46].

| Compound	Concentration [g/L]
NaCl	24,53
$MgCl_2$	5,20
Na_2SO_4	4,09
$CaCl_2$	1,16
KCl	0,695
$NaHCO_3$	0,201
KBr	0,101
H_3BO_3	0,027
$SrCl_2$	0,025
NaF	0,003

3.4 Corrosion testing

Electrochemical measurements were performed under a range of experimental conditions. Two different test setups were used for electrochemical testing in this project, i.e. with and without an applied MF. This section presents the test setups and apparatus used for electrochemical measurements. The test matrix is given in section 3.6.

3.4.1 Electrochemical measurements

Recording of LPR measurements and potentiodynamic polarization curves were performed to obtain the corrosion rates. LPR gives a value for the polarization resistance, R_P, of the test specimen, while polarization curves give the corrosion rate by extrapolating the linear regions of the anodic and cathodic curves. R_P and Tafel constants, b_a and b_c, obtained from the polarization curves were used to calculate the corrosion rate from the Stern Geary equation given in Equation C.1 in Appendix C. The corrosion rates calculated from both LPR and polarization curves were compared.

A three-electrode setup, as illustrated in Figure 3.2, was used for electrochemical measurements. The working electrode (WE) is the test specimen whereas a platinum electrode was used as a counter electrode (CE) in all experiments. A Gamry Interface 1000 potentiostat was used to polarize the samples. Air bubbling by an aquarium pump was applied to secure that the test solution was saturated with oxygen, and to give some stirring in the electrolyte, preventing stagnant conditions.
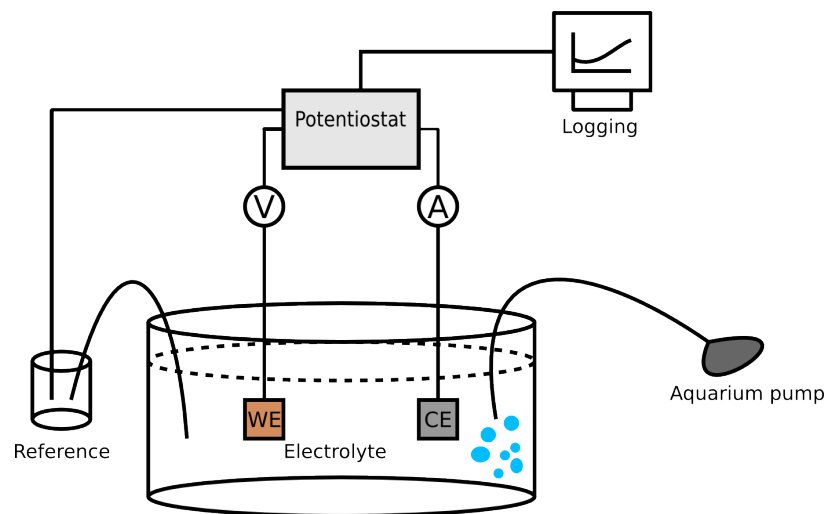

Figure 3.2 Schematic presentation of the three-electrode system used for electrochemical measurements. The notation CE and WE refer to the counter electrode and test specimen, respectively. The potentiostat measures the potential, *V*, between the reference electrode and test specimen by applying a current, *A*, between the WE and the CE.

The LPR measurements were performed by polarizing the sample 10 mV in both the cathodic and anodic direction starting from the open circuit potential (OCP). Polarization curves were recorded by polarizing the sample 500 mV in the cathodic and anodic direction, by moving 10

mV per minute from OCP. The cathodic curve was recorded prior to the anodic curve in both LPR and polarization curves. After the cathodic curve was obtained, the sample was left to freely corrode for at least one hour to retrieve OCP, and then the anodic curve was recorded. The reason for this is to prevent changes in the surface conditions due to corrosion. Figure 3.3 shows a photo of the test setup used for electrochemical measurements without an applied MF. Numbered components are specified in Table 3.3.
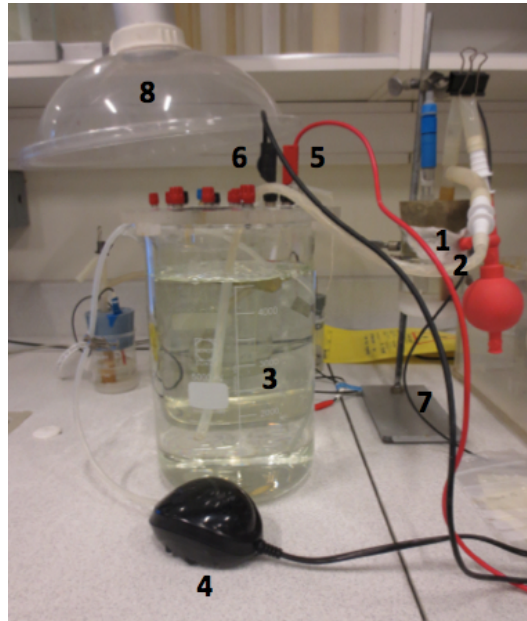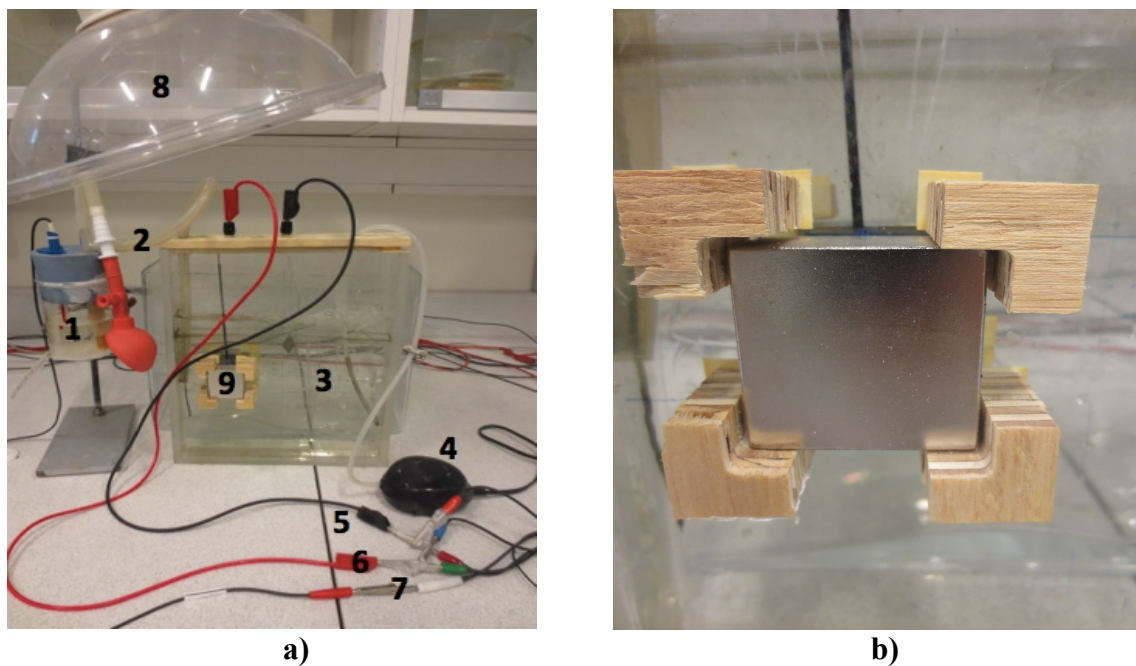

Figure 3.3 An overview of the test setup used for corrosion testing without an applied MF. Numbered components are specified in Table 3.3.

Table 3.3 Numbered components in the test setup showed in Figure 3.3 and Figure 3.4

| Item #	Explanation
1	Reference electrode (Ag/AgCl)
2	Tube filled with electrolyte and cotton string (salt bridge)
3	Container with test specimen (NAB), counter electrode (Pt) and electrolyte
4	Aquarium pump
5	Counter electrode connection
6	Working electrode connection
7	Reference connection
8	Fume hood

3.4.2 Electrochemical measurements under influence of magnetic field

A container delivered from the workshop at IPM was applied for electrochemical measurements under influence of an applied MF, and is shown in Figure 3.4. Numbered components are specified in Table 3.3, except from component number 9. The MF was created using two large NdFeB permanent magnets (40x40x20mm), corresponding to number 9 in Figure 3.4, separated by a distance of 5,6 cm. Pieces of wood were glued on the container to hold the magnets in place. The field intensity was measured by a GM07 Hirst Gaussmeter with a transverse probe, and varied between 0,15-0,28 Tesla in the region where the samples were placed during testing. The samples were oriented parallel to the flux lines of the MF, as this configuration will affect the corrosion rate most (section 2.3.1), and is illustrated in Figure 3.5.

a)   b)

Figure 3.4 The pictures show a) an overview of the test setup used for electrochemical testing with an applied MF and b) a close up picture of how the magnets are fixed. Numbered components are specified in Table 3.3, except from the permanent magnets (number 9).
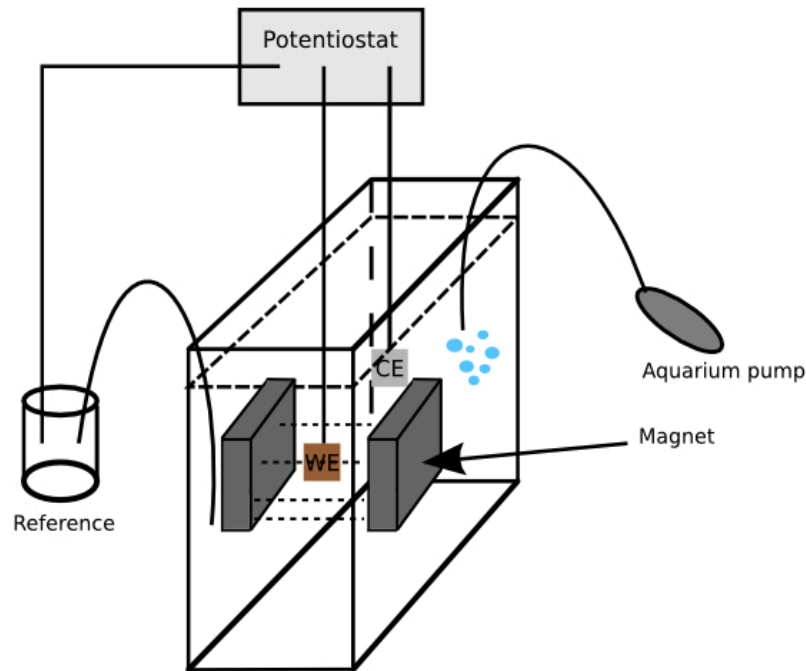
Figure 3.5 Schematic presentation of the test setup used for electrochemical measurements with an applied MF. The MF is generated by two permanent magnets separated by a distance of 5,6 cm. The dashed lines between the magnets show the direction of the magnetic flux lines. Please notice that the sample is placed parallel to the flux lines.

3.4.3 Long-term experiments

Ten samples were freely exposed to circulating, natural seawater in Sealab at Brattøra for nine weeks, to develop a protective surface film. One sample was exposed to a MF of 0,15-0,20 Tesla, while the other samples were freely exposed without a MF. OCP was continuously measured during the test period for only two of the samples, due to limited available channels for corrosion logging. However, OCP was measured manually two times during the test period and compared with OCP for samples that were continuously monitored.

After nine weeks, LPR and polarization curves were recorded manually according to the test setup shown in Figure 3.6. V_1 and V_2 represent two multimeters used to measure the potential over a known resistance (R) of 100 Ω, and the potential of the test specimen (WE), respectively. The current in the circuit was calculated from Ohm´s law by using the measured potential over a resistance, R, while V_2 manipulated the potential of WE. LPR measurements were recorded by polarizing 10 mV from OCP in the cathodic and anodic direction, and allowing the current to stabilize for 5 minutes before reading it´s value. Polarization curves

were recorded for only one of the freely exposed samples, by polarizing the sample 500 mV in the cathodic and anodic direction, by moving 25 mV from OCP each third minute. The remaining samples were taken out from the container and brought to Corrosion Lab, for electrochemical measurements and surface analysis (see test matrix in Table 3.5).
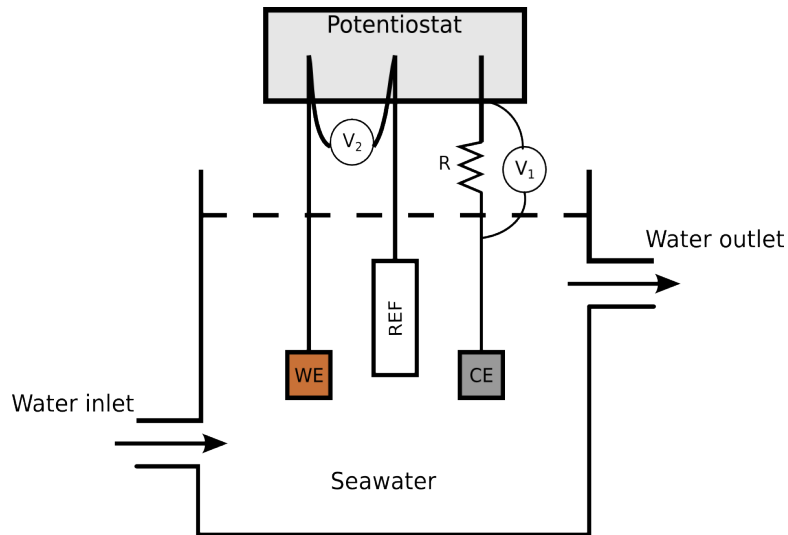
Figure 3.6 A schematic presentation of the test setup used for electrochemical testing in Sealab. V_1 and V_2 measure the potential over a known resistance, R, and the potential of the test specimen (WE), respectively. The notation R represents a resistance of 100 Ω.

3.5 Surface characterization

Samples for surface characterization were freely exposed to the same conditions as for electrochemical measurements. The microstructure and corroded surfaces were examined in a 3D optical microscope. After rinsing in ethanol, the corroded surfaces were characterized by SEM to study the surface morphology. For this purpose a working distance (WD) of approximately 10 mm, an accelerating voltage (EHT) of 15 kV and a secondary electron (SE) detector were used. EDS was applied to identify the chemical composition of the sample surfaces. Remaining corrosion products in the test solution after polarization was investigated by XRD analysis to identify its chemical composition. Prior to the analysis the corrosion products were filtrated out of the solution by a funnel, crushed and dispersed onto a silicon specimen holder.

3.6 Test matrix

The test matrix for the corrosion testing in this work can be divided into two parts. In phase I, the samples were freely exposed under different conditions. The test specimens might be grouped in four, according to Table 3.4, distinguished in the way they were exposed prior to testing.

Table 3.4 Test matrix for phase I of the corrosion testing.

Sample	Treatment prior to testing
Fresh	One hour in SSW
Aged (SSW)	One week in SSW
Aged (x ppmW S)	One week in x ppmW sulphide
Long-term	Nine weeks in natural seawater (Sealab)

In phase II of the corrosion testing, electrochemical measurements and surface analysis were performed according to the test matrix shown in Table 3.5. A total of 35 samples were tested under a range of experimental conditions, i.e. with and without an applied MF, and in both pure and sulphide-polluted SSW. The test matrix specifies the *type* of sample, i.e. treatment before testing (see Table 3.4), and the conditions during electrochemical testing (*test*). Note that the test specimen was *either* polarized or subjected to surface characterization. The notation (-) means that the sample was used for surface analysis. Further, the notation MF means that the test was under influence of an applied magnetic field and S denotes that the test solution was polluted with $Na_2S \cdot xH_2O$.

Some of the long-term samples were freely exposed one week in 10 ppmW sulphide-polluted SSW prior to testing (sample 29-35). Only three were exposed in a MF due to limited test setups. Please notice that this was done after nine weeks of immersion in natural seawater. All tests in the Corrosion Lab were performed in aerated test solutions.

Table 3.5 Test matrix for phase II of the corrosion testing. The notation MF means that the test was under influence of an applied magnetic field, while S means that the test solution was polluted with $Na_2S \cdot xH_2O$. The notation SSW and SW refers to synthetic seawater and seawater, respectively.

Sample#	Type	Test	Sample#	Type	Test
1	Fresh	SSW	**19**	Aged (1 ppmW S)	1 ppmW S
2	Fresh	SSW	**20**	Aged (1 ppmW S)	1 ppmW S
3	Fresh	SSW+ MF	**21**	Aged (1 ppmW S)	-
4	Fresh	SSW+ MF	**22**	Aged (10 ppmW S)	10 ppmW S
5	Fresh	1 ppmW S	**23**	Aged (10 ppmW S)	-
6	Fresh	1 ppmW S	**24**	Aged (100 ppmW S)	100 ppm S
7	Fresh	10 ppmW S	**25**	Aged (100 ppmW S)	-
8	Fresh	10 ppmW S	**26**	Long term (MF)	-
9	Fresh	100 ppmW S	**27**	Long term	-
10	Fresh	100 ppmW S	**28**	Long term	Natural SW
11	Fresh	MF+S*	**29**	Long term	-
12	Fresh	MF+S*	**30**	Long term	10 ppmW S
13	Aged (SSW)	SSW	**31**	Long term	10 ppmW S
14	Aged (SSW)	SSW+ MF	**32**	Long term	10 ppmW S
15	Aged (SSW)	SSW+ MF	**33**	Long term	MF+S*
16	Aged (SSW)	-	**34**	Long term	MF+S*
17	Aged (MF+S**)	MF + S**	**35**	Long term	MF+S*
18	Aged (MF+S**)	-			

*10 ppmW

**1 ppmW

4 Results

This section presents test results from the experimental work according to the test matrix in Table 3.4 and Table 3.5 (see section 3.6). The objective with the electrochemical measurements was to investigate the corrosion behaviour of NAB in sulphide-polluted SSW and possible synergy effects with an applied MF. The results from OCP and pH measurements are presented first. Then the results from electrochemical testing, involving LPR and potentiodynamic polarization curves under a range of experimental conditions, are given. Results from macroscopic and microscopic surface analysis are presented in the end to support observations from the electrochemical testing. This includes 3D light microscope, SEM and EDS analysis. XRD analysis was used for characterization of corrosion products. All potentials mentioned in this work are with respect to the Ag/AgCl reference electrode.

4.1 Open circuit potentials

The OCP was measured prior to all tests, and the duration of OCP measurements varied based on the test matrix in Table 3.4, i.e. OCP was measured one hour for fresh samples, one week for aged samples and nine weeks for long-term samples. Some examples of OCP measurements are shown in Figure 4.1-4.4. The rest are found in Appendix B.

The OCP of fresh NAB was measured one hour in the test solution in which the experiments were performed prior to polarization. Figure 4.1 shows OCP of fresh NAB freely exposed for one hour in both pure and 10 ppmW sulphide-polluted SSW, with and without an applied MF. The general trend was an immediate increase in potential to more positive values for specimens in sulphide-polluted SSW. Conversely, the potential in pure SSW decreased to more negative values, and reached a constant potential after one hour. However, in SSW containing sulphide the potential was still increasing in the positive direction after one hour. The development of OCP of NAB freely exposed in 10 ppmW and 100 ppmW sulphide-polluted SSW without an applied MF can be seen in Figure 4.2. NAB had an OCP of around -770 mV upon immersion in 100 ppmW sulphide solution, increasing spontaneously to -385 mV during half an hour. From this point the potential continued to increase, but with a lower

slope, until it reached the maximum value of –83 mV after 20 hours. After one week, the OCP was around -80 mV. The same trend appears for NAB in 10 ppmW sulphide-containing SSW, where the potential of NAB was -270 mV upon immersion, increasing to -75 mV after 11 hours. After one week, the OCP was around -65 mV.
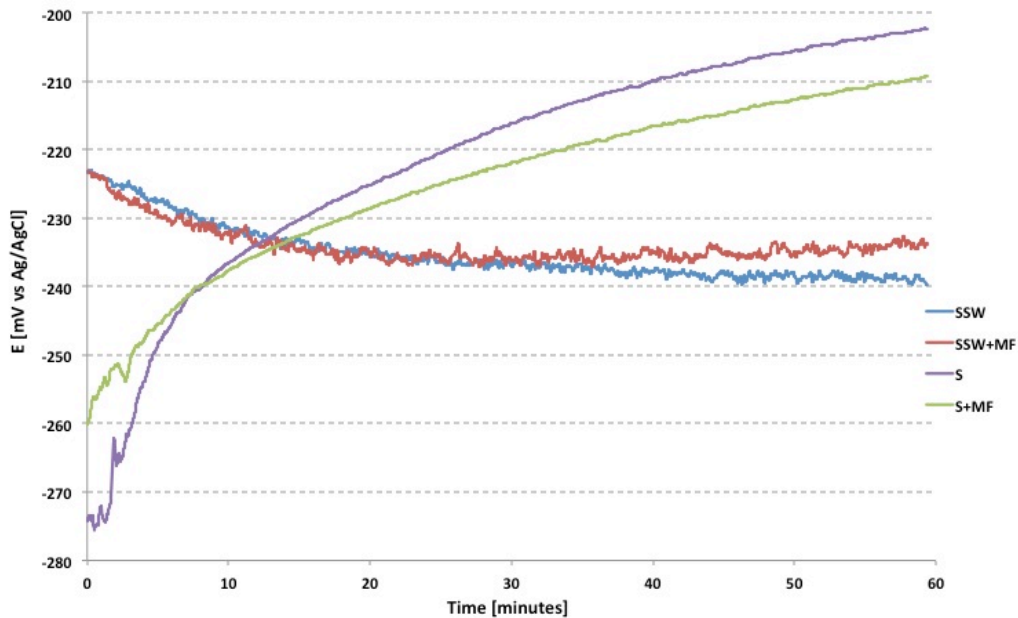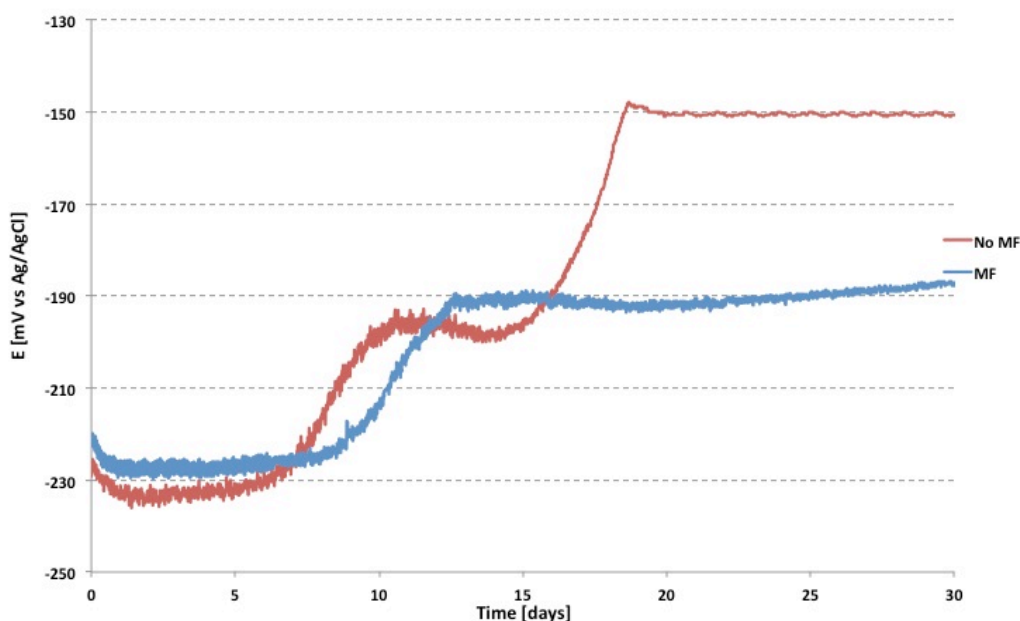

Figure 4.1 OCP of NAB freely exposed in both pure and 10 ppmW sulphide-polluted SSW, with and without a MF, for one hour. The notation MF means that the test was under influence of a magnetic field. The notation S refers to SSW polluted with 10 ppmW sulphide
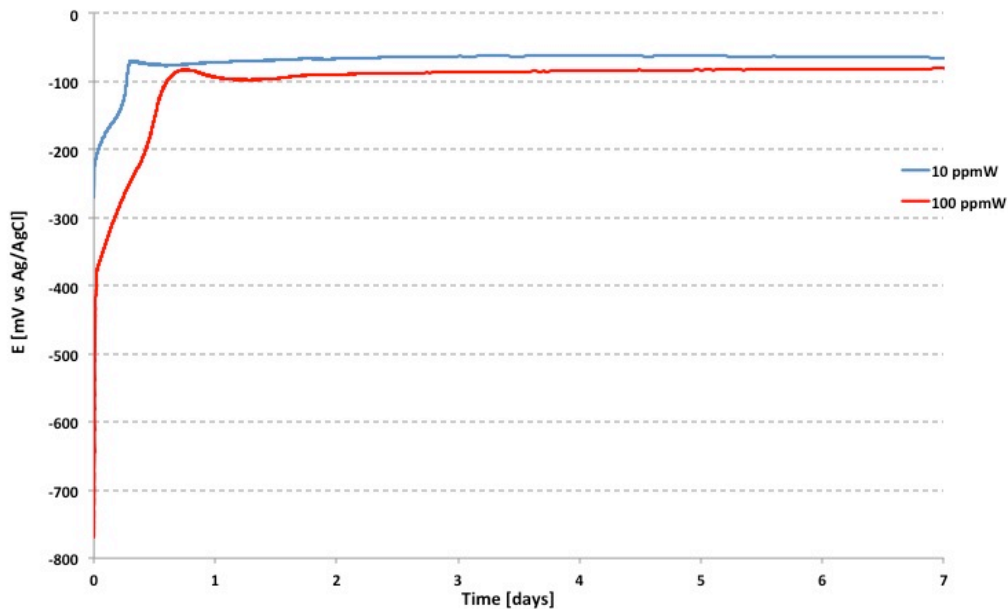
Figure 4.2 OCP of NAB freely exposed in 10 ppmW and 100 ppmW sulphide-polluted SSW without an applied MF for one week.

34

Figure 4.3 shows the development of OCP of freely exposed NAB in natural seawater with and without an applied MF. Upon immersion, the OCP was about -220 mV and -230 mV with and without a MF, respectively, increasing to -190 mV and -150 mV after 30 days. However, when moving the samples to SSW in the Corrosion Lab, the OCP changed to more negative values upon immersion as seen in Figure 4.4.

Figure 4.3 OCP of freely exposed NAB in natural seawater with and without an applied MF for 30 days. The notation MF means that the test was under influence of a magnetic field.

The OCP of long-term NAB freely exposed in 10 ppmW sulphide-polluted SSW with and without an applied MF for one week is present in Figure 4.4. Please notice that this measurement was performed after nine weeks of immersion in natural seawater in Sealab. The OCP is about -330 mV for both samples upon immersion, increasing to -110 mV and -78 mV during the first day with and without a MF, respectively. The potential stabilizes at more positive values than observed in natural seawater (see Figure 4.3). As in natural seawater, the potential of NAB exposed to a MF is more negative than without an applied MF.
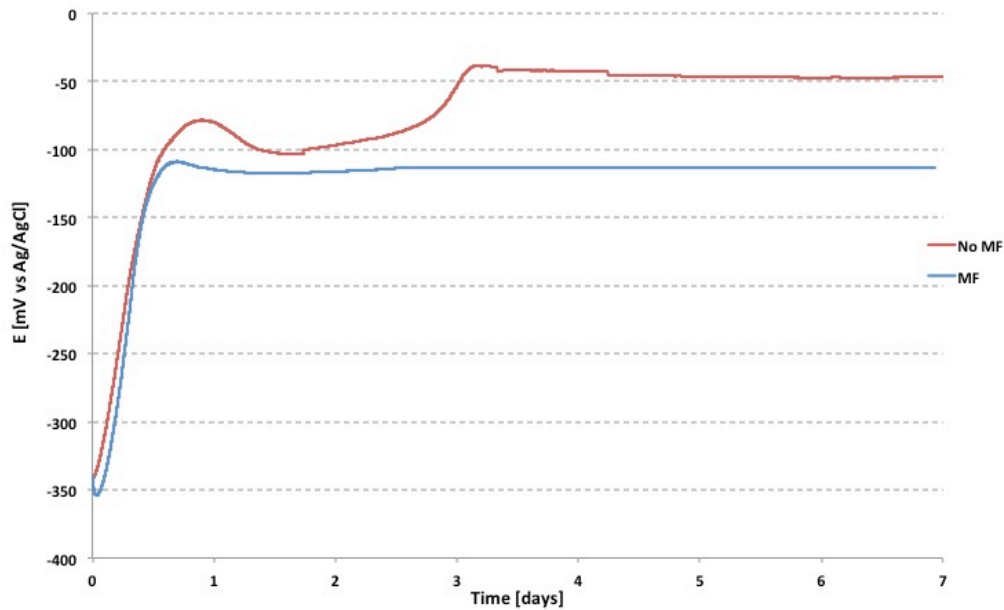
Figure 4.4 OCP of long-term NAB freely exposed in 10 ppmW sulphide-polluted SSW with and without an applied MF, for one week. The notation MF means that the test was under influence of a magnetic field.

4.2 pH measurements

The pH was measured in 10 ppmW and 100 ppmW sulphide-polluted SSW during one week. Prior to testing, the pH of the SSW was measured to be 7,86. The addition of sulphide in SSW revealed an immediate increase in pH level, shown in Table 4.1, the increase being stronger for higher sulphide content. However, the pH level dropped to approximately 7,8 after one day of immersion. In the end of the experiment, the pH was still around 7,8.

Table 4.1 pH measurements of 10 ppmW and 100 ppmW sulphide-polluted SSW.

Test	Start	End
10 ppmW	8,27	7,80
100 ppmW	9,63	7,93

4.3 Potentiodynamic polarization curves

Potentiodynamic polarization curves were recorded according to the test procedure in section 3.4.1. Some examples of polarization curves are given in Figure 4.5-4.11. In this section, polarization curves recorded under different experimental conditions are plotted together, to illustrate tendencies. All polarization curves can be found in Appendix D. Polarization curves recorded in SSW and natural seawater, with and without a MF, are presented first. Afterwards polarization curves recorded in sulphide-polluted SSW, with and without a MF, are shown. All tests were performed under aerated conditions. The OCP measured prior to the electrochemical measurements are given in section 4.1 and Appendix B.

4.3.1 Synthetic- and natural seawater

Polarization curves of fresh NAB in pure SSW with and without an applied MF can be seen in Figure 4.5. The presence of a MF does not affect the polarization behaviour of fresh NAB significantly, but a slightly lower cathodic current density is observed in the presence of a MF.
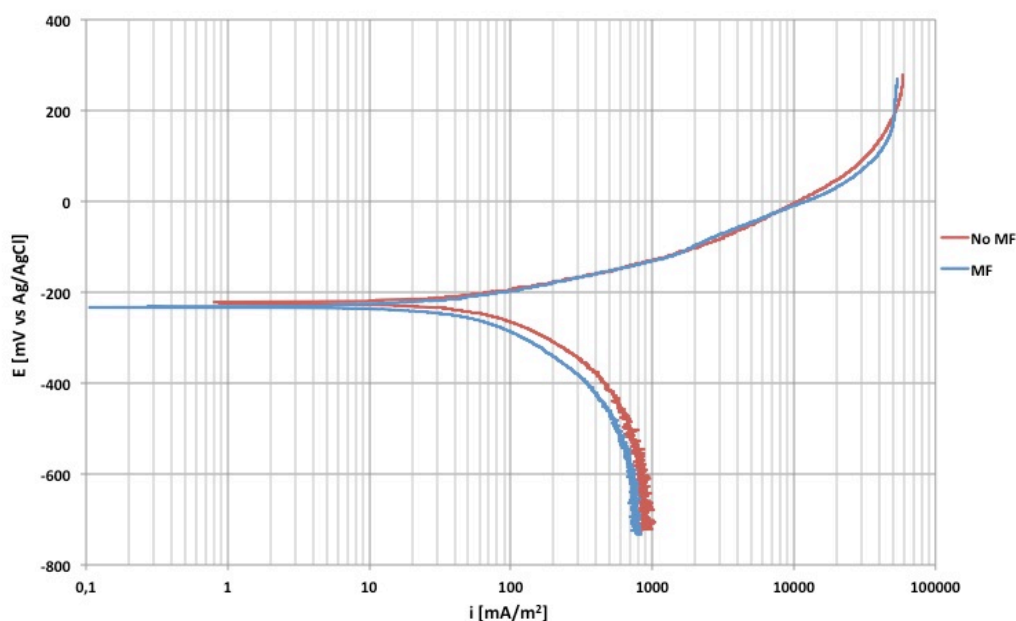
Figure 4.5 Polarization curves of fresh NAB in pure SSW with and without an applied MF. The notation MF means that the test was under influence of a magnetic field.
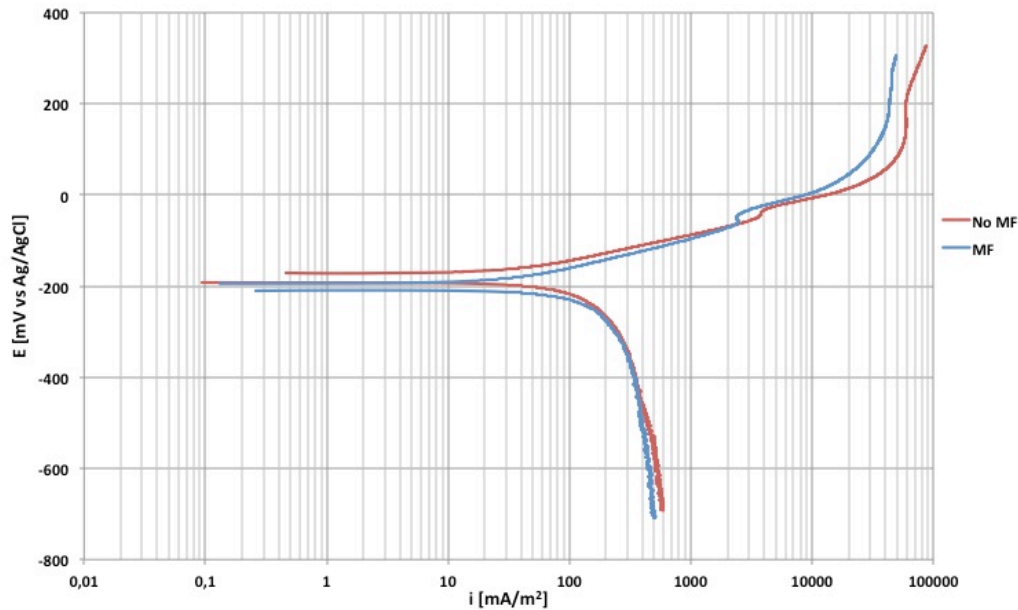
Figure 4.6 shows polarization curves of fresh, aged and long-term samples without an applied MF. The long-term sample was polarized manually in natural seawater, while the fresh and aged samples were polarized in SSW. Fresh and aged NAB show the same trend, but the cathodic current density is lower for the aged sample. Several drops in cathodic current density are observed for long-term NAB. This is not evident for fresh and aged NAB.
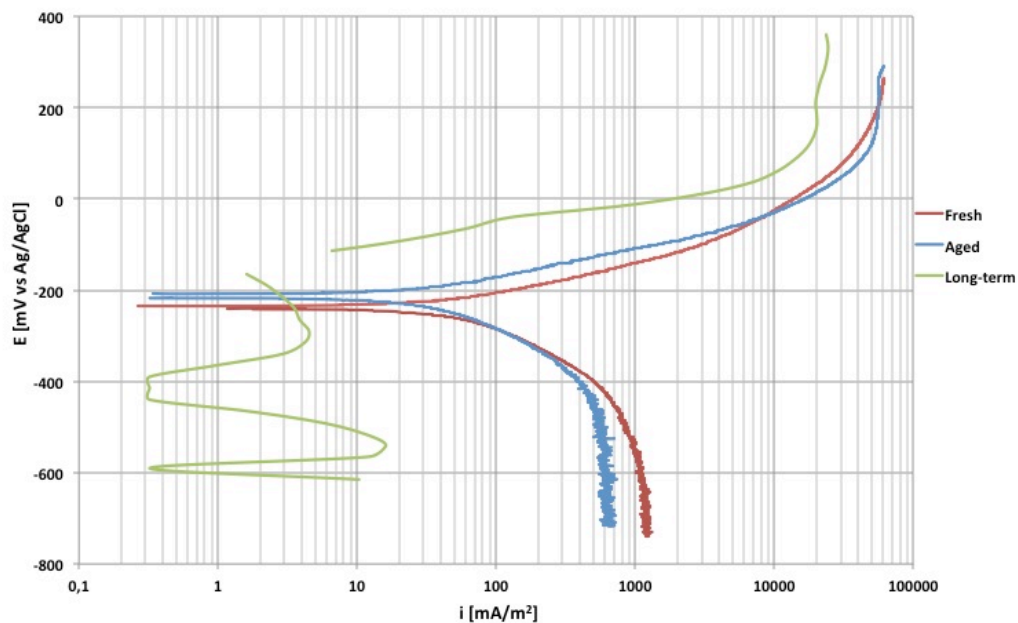
Figure 4.6 Polarization curves of fresh, aged and long-term samples without an applied MF. The curve is recorded in natural seawater for long-term NAB, and in pure SSW for aged and fresh NAB.

4.3.2 Sulphide-polluted synthetic seawater

Polarization curves of fresh samples recorded in 10 ppmW sulphide-polluted SSW with and without an applied MF can be seen in Figure 4.7. Comparison of the polarization curves in Figure 4.5 and Figure 4.7 shows that the rate of charge transfer of the oxygen reduction reaction is accelerated in sulphide-polluted SSW.
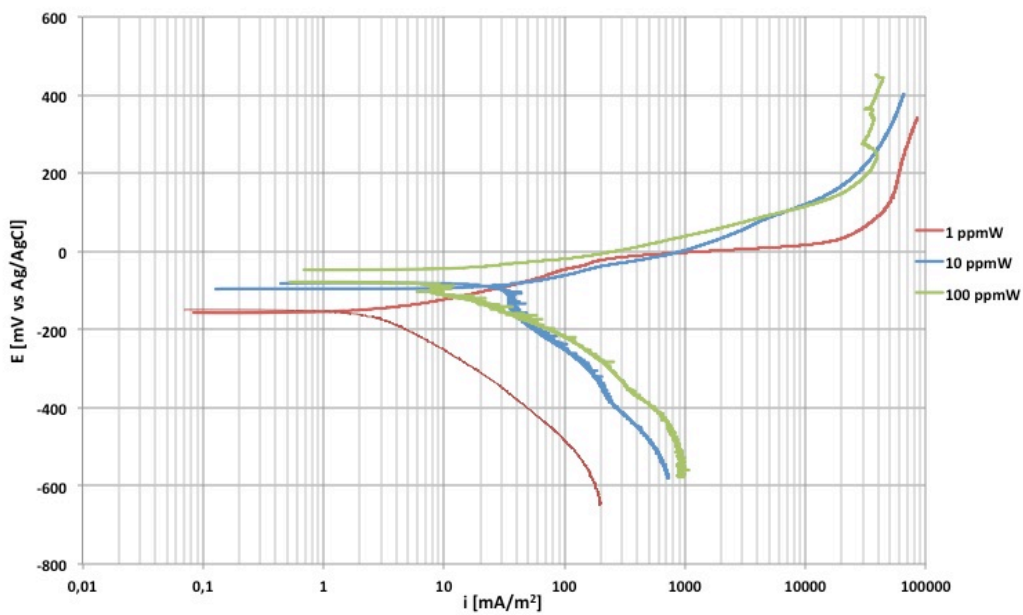
Figure 4.7 Polarization curves of fresh samples in 10 ppmW sulphide-polluted SSW with and without an applied MF. The notation MF means that the test was under influence of a magnetic field.

Polarization curves of fresh and aged samples in sulphide-polluted SSW, without an applied MF, are shown in Figure 4.8 and Figure 4.9, respectively. The general trend was a shift in OCP to more positive values for higher sulphide content (100 ppmW) after cathodic polarization. This is not observed in 1 ppmW and 10 ppmW sulphide-polluted SSW, where the potential retrieve OCP prior to the anodic polarization. According to the test procedure in section 3.4.1, the sample was left to freely corrode one hour prior to anodic polarization, to retrieve its value. The limiting cathodic current density increases with the sulphide content for aged samples in Figure 4.9, while the limiting cathodic current density is approximately similar for fresh samples, independent of the sulphide content.

4 Results
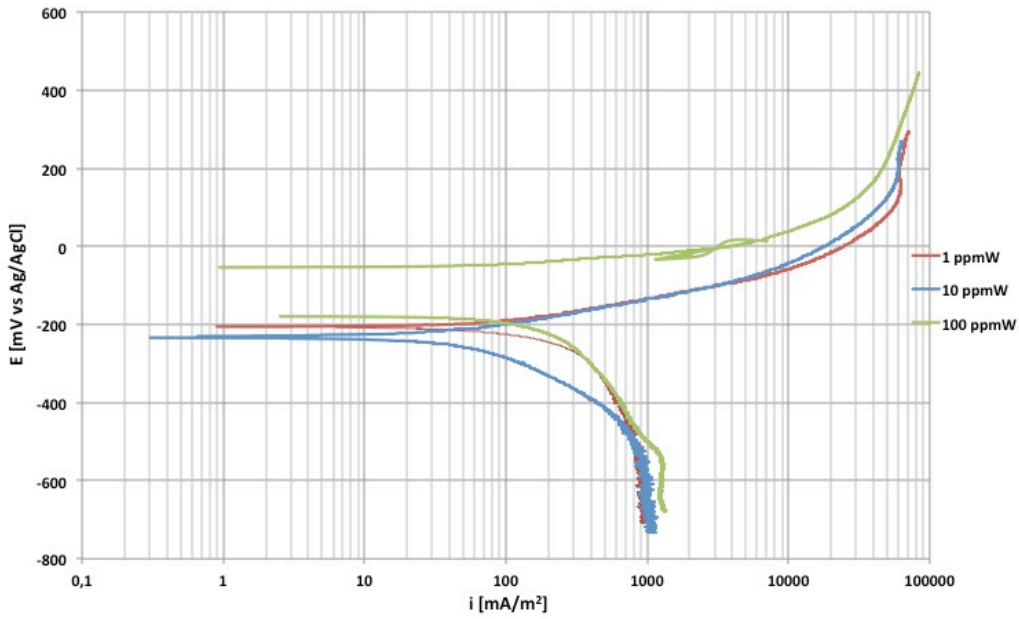
Figure 4.8 Polarization curves of fresh samples in SSW polluted with different sulphide content, in the absence of a MF.
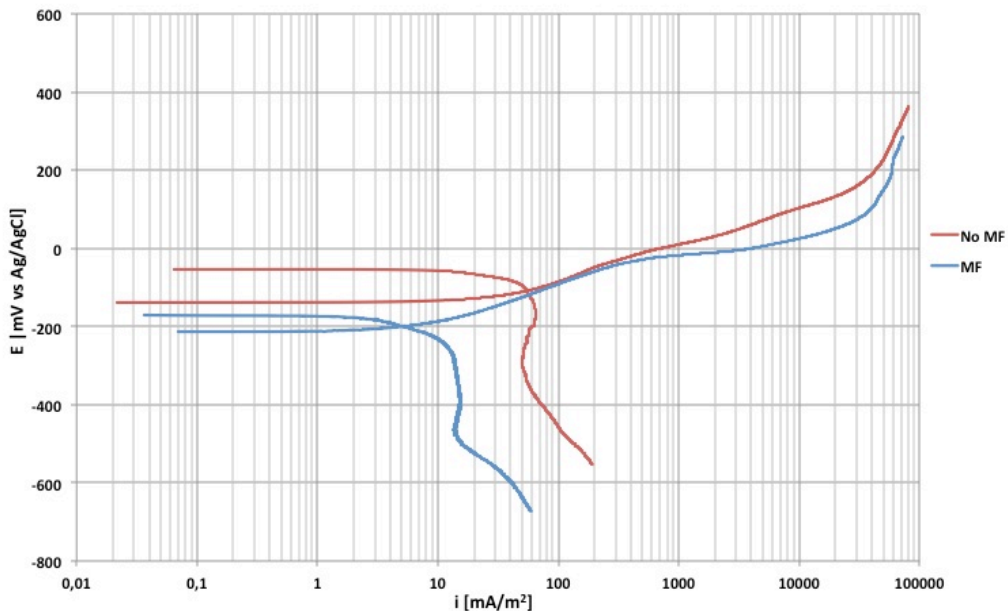

Figure 4.9 Polarization curves of aged samples in SSW polluted with different sulphide content, in the absence of a MF.

Figure 4.10 shows polarization curves of aged and long-term samples recorded in 10 ppmW sulphide-polluted SSW without a MF. The aged sample was placed one week in sulphide-polluted SSW prior to testing. A comparison of polarization curves for long-term samples in 10 ppmW sulphide-polluted SSW with and without an applied MF can be seen in Figure 4.11. The general trend was a decrease in OCP after cathodic polarization. According to the test

40

procedure in section 3.4.1, the sample was left to freely corrode one hour prior to anodic polarization, to retrieve its value. A lower cathodic current density is also observed in the presence of a MF.
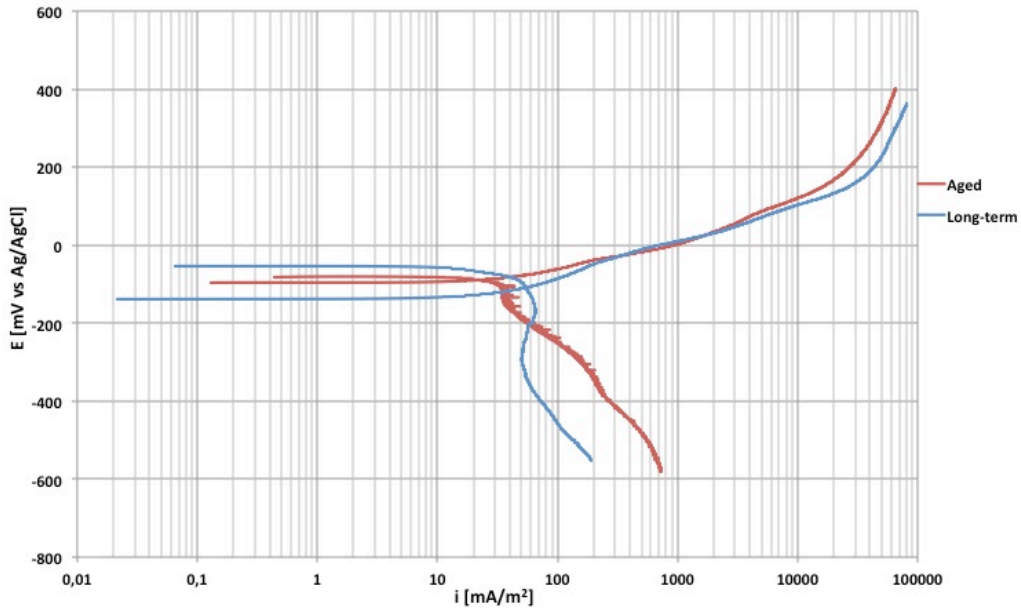

Figure 4.10 Polarization curves of aged and long-term samples in 10 ppmW sulphide-polluted SSW without an applied MF.
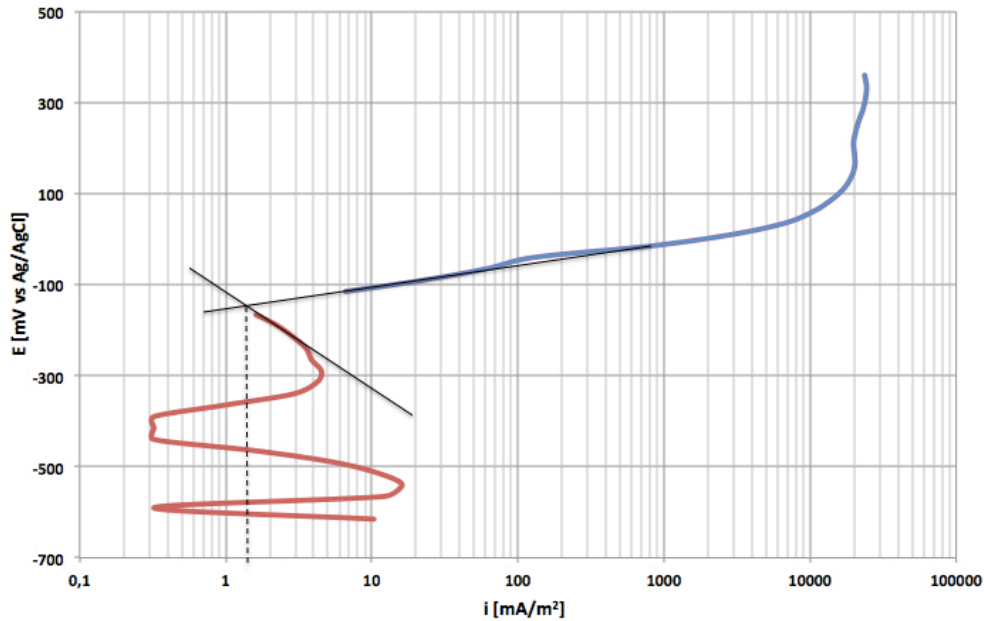

Figure 4.11 Polarization curves of long-term samples in 10 ppmW sulphide-polluted SSW with and without an applied MF.

4 Results

4.4 LPR measurements

The polarization resistance, R_p, obtained from LPR measurements was used to calculate the corrosion current density, i_{corr}, by the Stern-Geary equation given in Equation C.1 (see Appendix C). Tafel slope constants, b_a and b_c, were found by extrapolating the linear regions of the anodic and cathodic polarization curves to OCP. LPR measurements are shown in Appendix E. The corresponding polarization- and overvoltage curves can be found in Appendix D and Appendix F, respectively. Examples of polarization curves and Tafel slopes of fresh NAB immersed in SSW, and long-term NAB immersed in natural seawater are present in Figure 4.12 and Figure 4.13, respectively. Please notice that LPR measurements were not performed for all samples in Table 3.5 in this work.
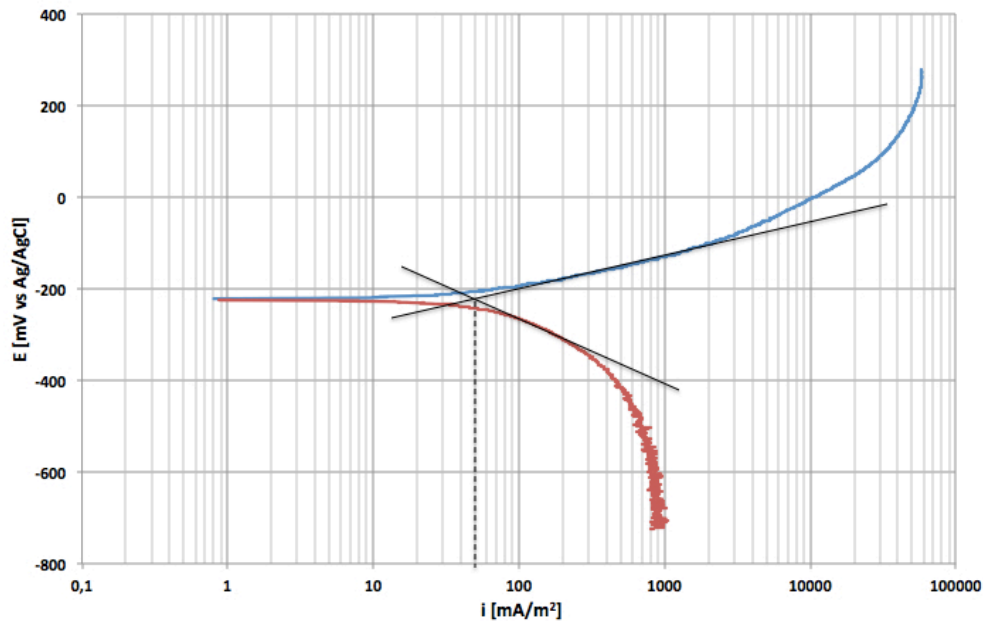
Figure 4.12 Polarization- and overvoltage curves of fresh NAB immersed in SSW. The black, solid lines represent the extrapolation of the linear regions of the anodic and cathodic polarization curves. The dashed line gives the corrosion current density, i_{corr}.

Figure 4.13 Polarization- and overvoltage curves of long-term NAB immersed in natural seawater. The black, solid lines represent the extrapolation of the linear regions of the anodic and cathodic polarization curves. The dashed line gives the corrosion current density, i_{corr}.

The values for Tafel slopes and results from the LPR measurements of fresh, aged and long-term samples are listed in Table 4.2-4.4, respectively. Estimated corrosion current densities by both LPR measurements and polarization curves are compared in Table 4.5. The notation *type* refers to the treatment prior to testing (see test matrix in Table 3.4), while the notation *test* gives the conditions, during electrochemical testing (see test matrix in Table 3.5). If parallel tests were performed, the values in Table 4.2-4.5 are based on the average.

Table 4.2 Values for Tafel slopes and results from the LPR measurements of fresh samples. The notation MF means that the test was under influence of a magnetic field, while S denotes 10 ppmW sulphide-polluted SSW.

Value	SSW	SSW+ MF	S
b_a [V/decade]	0,064	0,062	0,059
b_c [V/decade]	-0,16	-0,20	-0,23
R_P [Ωm^2]	0,351	0,311	0,190

Table 4.3 Values for Tafel slopes and results from LPR measurements of aged samples in 10 ppmW and 100 ppmW sulphide-polluted SSW. The notation S refers to SSW polluted with $Na_2S \cdot xH_2O$.

Value	10 ppmW S	100 ppmW S
b_a [V/decade]	0,062	0,050
b_c [V/decade]	-0,22	-0,14
R_P [Ωm^2]	0,640	0,790

Table 4.4 Values for Tafel slopes and results from LPR measurements of long-term samples. The notation MF means that the test was under influence of a magnetic field, while S denotes 10 ppmW sulphide-polluted SSW.

Value	Natural SW	MF + S	S
b_a [V/decade]	0,043	0,10	0,098
b_c [V/decade]	-0,22	- 0,17	-0,48
R_P [Ωm^2]	11,6	2,26	0,414

Table 4.5 Estimated corrosion current densities of NAB by LPR measurements and polarization curves. The notation MF means that the test was under influence of a magnetic field. The notation S refers to SSW polluted with $Na_2S \cdot xH_2O$.

Type	Test	Corrosion current density, i_{corr} [mA/m^2]	
		LPR	Polarization curves
Fresh	SSW	56	50
Fresh	SSW+ MF	66	60
Fresh	10 ppmW S	107	65
Aged (10 ppmW S)	10 ppmW S	33	21
Aged (100 ppmW S)	100 ppmW S	20	13
Long-term	Natural SW	1,4	1,5
Long-term	10 ppmW S	34	85
Long-term	MF + 10 ppmW S	12	12

4.5 Surface characterization

4.5.1 Macroscopic characterization of corroded surfaces

All sample surfaces were photographed with a digital camera and studied macroscopically after testing. Afterwards the samples were washed, cleaned and rinsed with ethanol. Pictures were taken before and after cleaning, and some examples of sample appearances are present in this section. The appearance of freely exposed NAB after one week of immersion in SSW polluted with 1, 10, and 100 ppmW sulphide can be seen in Figure 4.14. This corresponds to sample 21, 23 and 25 in Table 3.5, respectively. In general, clear variations in appearance were observed for different sulphide contents.

a)   b)   c)

d)   e)   f)
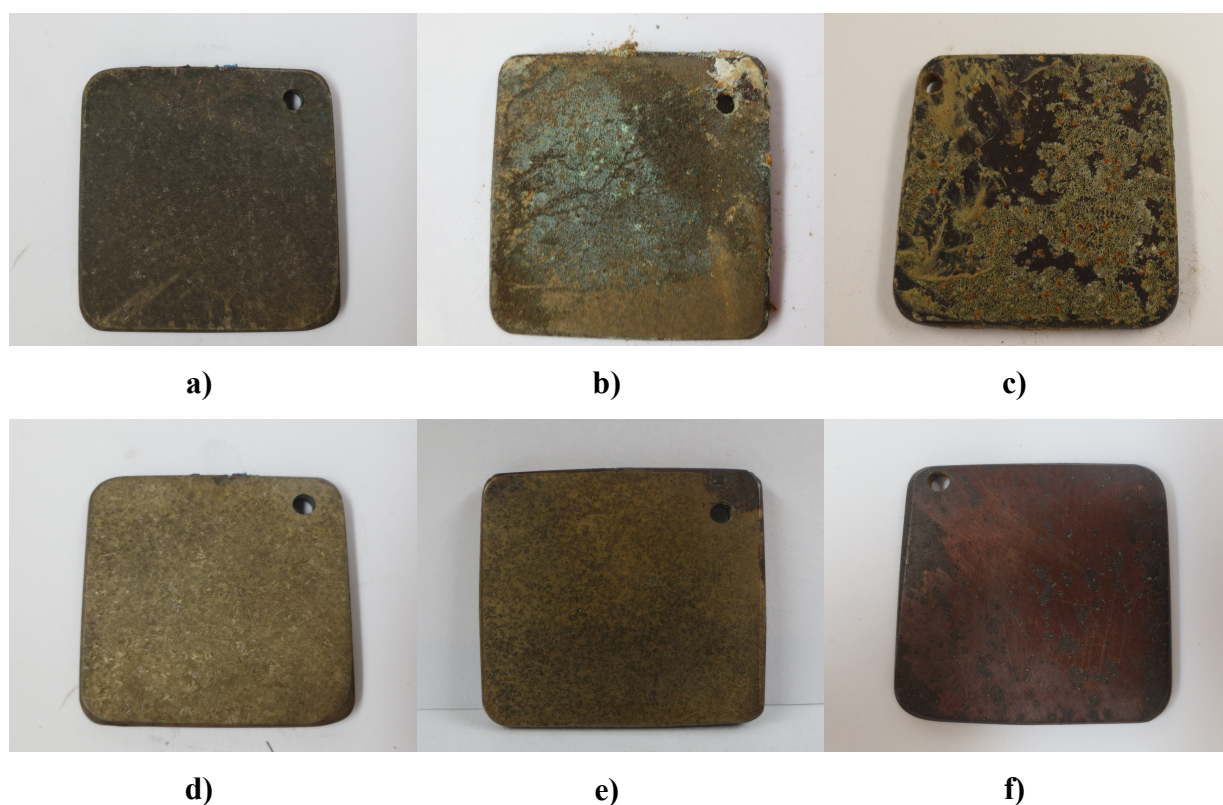
Figure 4.14 Sample appearance of freely exposed NAB after one week of immersion in SSW polluted with a) 1 ppmW, b) 10 ppmW and c) 100 ppmW sulphide. The same samples are shown after cleaning in d), e) and f), respectively.

Figure 4.15 a) shows the sample appearance of freely exposed NAB after nine weeks of immersion in natural seawater without a MF. This corresponds to sample 27 in Table 3.5. Figure 4.15 b) shows the sample appearance after nine weeks of immersion in natural

seawater followed by one week in 10 ppmW sulphide-polluted SSW without a MF. This corresponds to sample 29 in Table 3.5. Clear variations in appearance were observed.

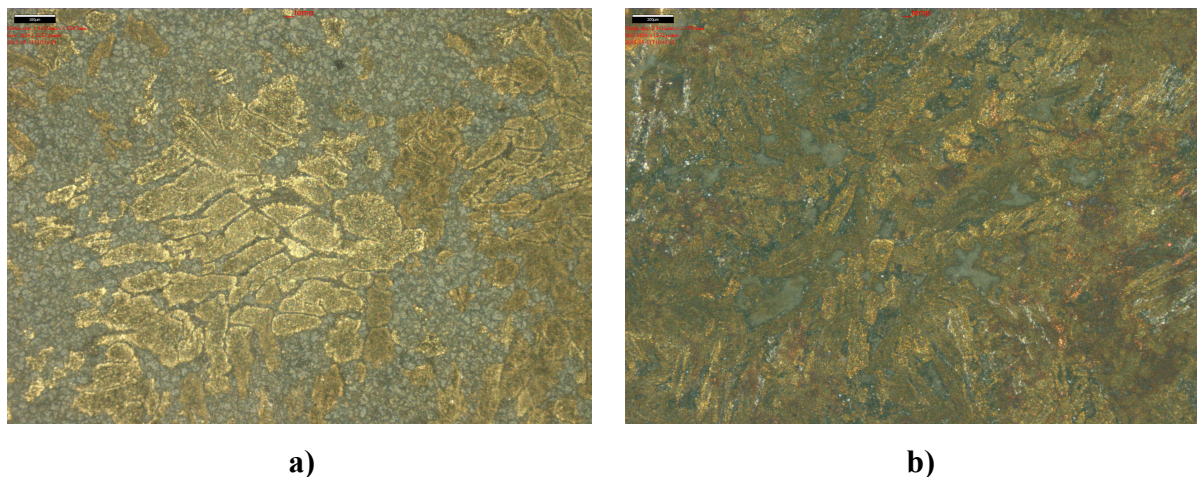a)   b)

Figure 4.15 Sample appearance of freely exposed NAB after a) nine weeks of immersion in natural seawater, and b) followed by one week in 10 ppmW sulphide-polluted SSW without a MF.

4.5.2 Microscopic characterization of corroded surfaces

Some samples, which were not used for electrochemical measurements, were also subjected to microscopic surface analysis (see test matrix in Table 3.5), by a 3D optical microscope and SEM. In the SEM, overview images were taken with low magnification, while EDS analysis were performed for images with higher magnifications. In this section, the pictures are present in the order they were taken, i.e. the 3D optical microscope pictures are shown first and then, a presentation of SEM images and EDS analysis are given.

4.5.2.1 3D optical microscope pictures

Figure 4.16 shows 3D optical microscope picture of freely exposed NAB after a) nine weeks of immersion in natural seawater, and b) followed by one week of exposure in 10 ppmW sulphide-polluted SSW without a MF. This corresponds to sample 27 and 29 in Table 3.5, respectively. Figure 4.17 a) and b) show pictures of freely exposed NAB after one week of immersion in 10 ppmW and 100 ppmW sulphide-polluted SSW without a MF, respectively. This corresponds to sample 23 and 25 in Table 3.5, respectively.

<center>a)   b)</center>

Figure 4.16 The pictures show surfaces of freely exposed NAB after a) nine weeks of immersion in natural seawater, and b) followed by one week in 10 ppmW sulphide-polluted SSW without a MF. The magnification is x10 and x5, respectively.


<center>a)   b)</center>
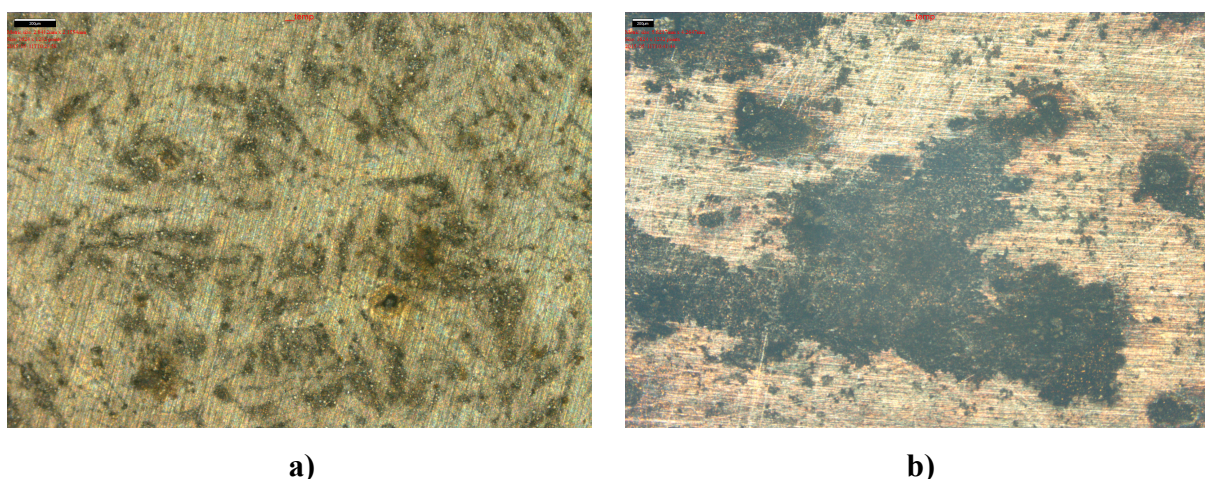
Figure 4.17 The pictures show surfaces of freely exposed NAB after one week of immersion in a) 10 ppmW and b) 100 ppmW sulphide-polluted SSW without a MF. The magnification is x5 and x2,5, respectively.

Corrosion craters were observed on the surfaces shown in Figure 4.16 b) and 4.17 a), and 3D pictures of the craters are present in Figure 4.18 and Figure 4.19, respectively. The hole on the left corner in Figure 4.19 corresponds to the hole where the platinum wire was connected, and is therefore not a crater. The depth-profiles indicated craters in the range of 40 μm to 202 μm. However, corrosion craters were not observed on freely exposed NAB in 100 ppmW sulphide-polluted SSW.
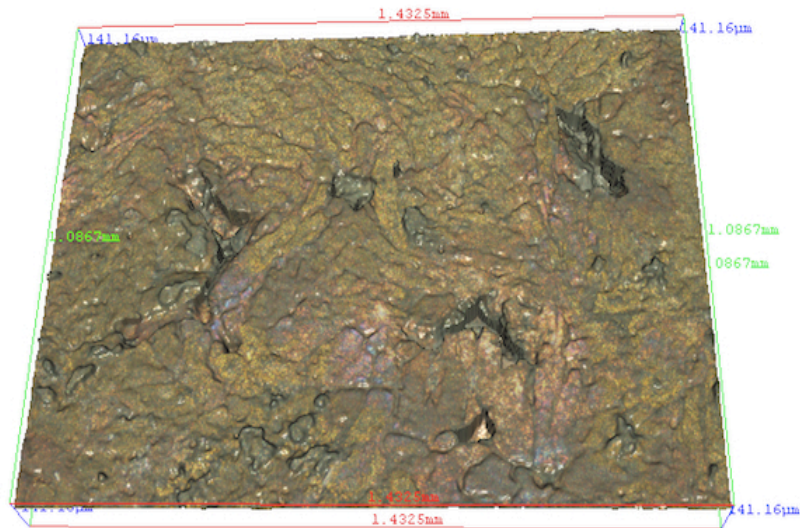
Figure 4.18 3D picture of corrosion craters on the surface of long-term NAB immersed in 10 ppmW sulphide-polluted SSW (sample 29 in Table 3.5).
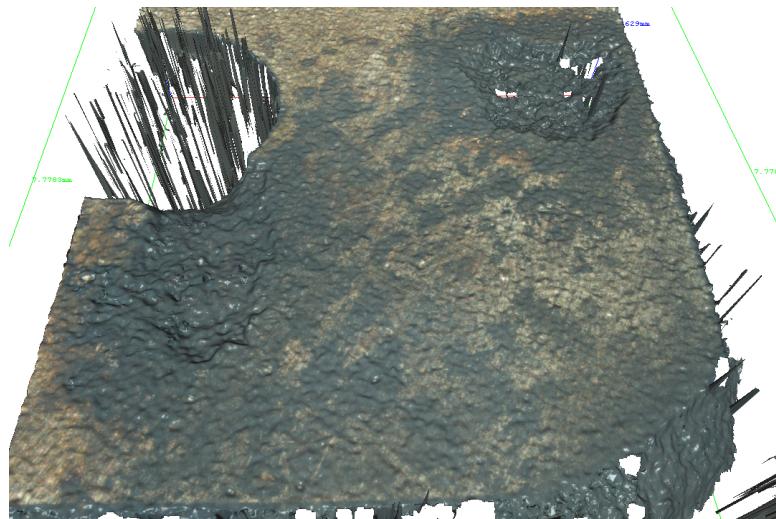

Figure 4.19 3D picture of corrosion craters on the surface of aged NAB, i.e. after one week of immersion in 10 ppmW sulphide-polluted SSW (sample 23 in Table 3.5).

4.5.2.2 SEM images and EDS analysis

Some results from microscopic characterization of the corroded surfaces by SEM and EDS analysis are given in this section. Figure 4.20 a) shows an overview picture of freely exposed NAB after nine weeks of immersion in natural seawater (sample 27 in Table 3.5). The corresponding EDS analysis is given in Figure 4.21, showing a clear variation in the oxygen content between the two spots in Figure 4.20 b).

a)   b)
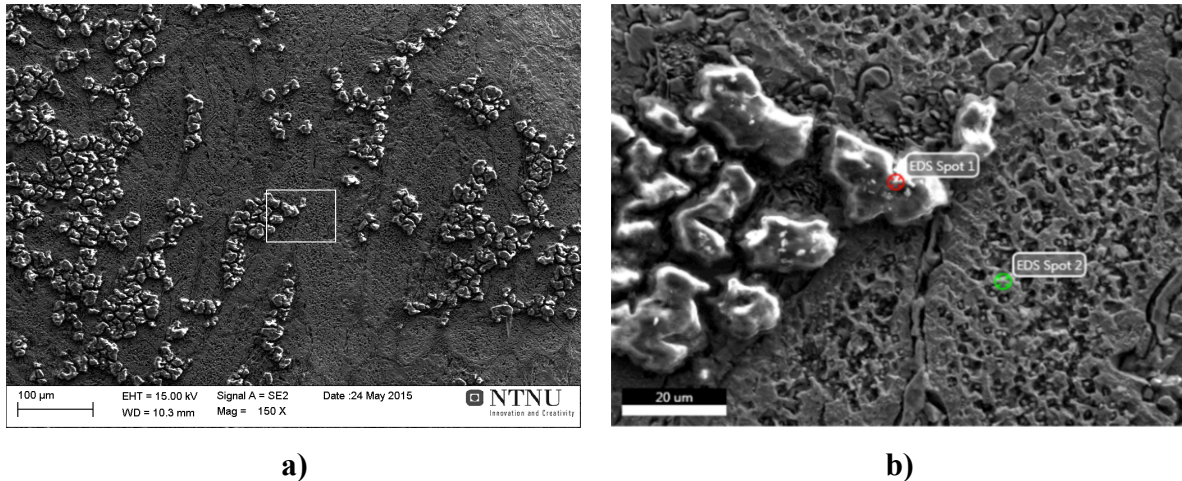
Figure 4.20 SEM images of freely exposed NAB after nine weeks of immersion in natural seawater. Magnification of marked area in a) is shown in b). Spot 1 and 2 in b) refer to the sites where EDS were performed. The EDS analysis of spot 1 and 2 can be seen in Figure 4.21.
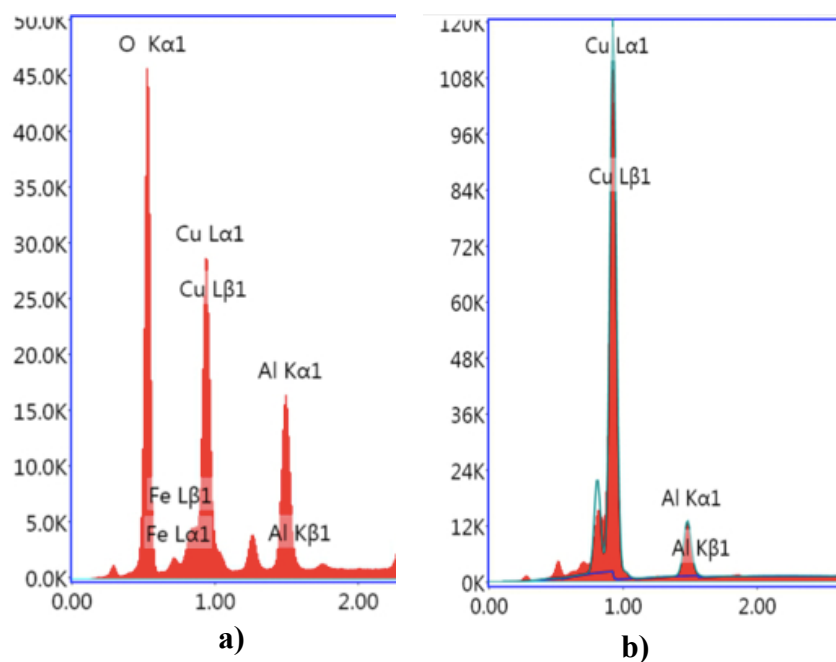

a)   b)
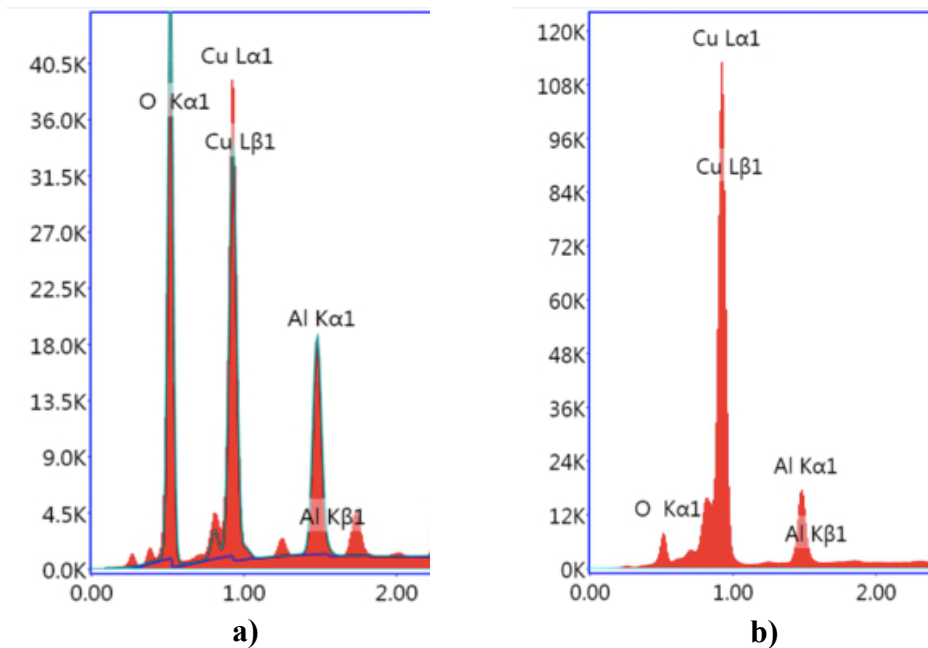
Figure 4.21 EDS analysis of a) spot 1 and b) spot 2 in Figure 4.20 b). The main constituents are Cu, Al and O in both spots.

4 Results

SEM images of freely exposed NAB after one week of immersion in SSW (sample 16 in Table 3.5) are present in Figure 4.22. The corresponding EDS analysis is given in Figure 4.23. Spot 1 and spot 2 in Figure 4.22 b) showed the most interesting information, and are included in this section. Very high oxygen content was observed in spot 1, while no oxygen was detected in spot 2.
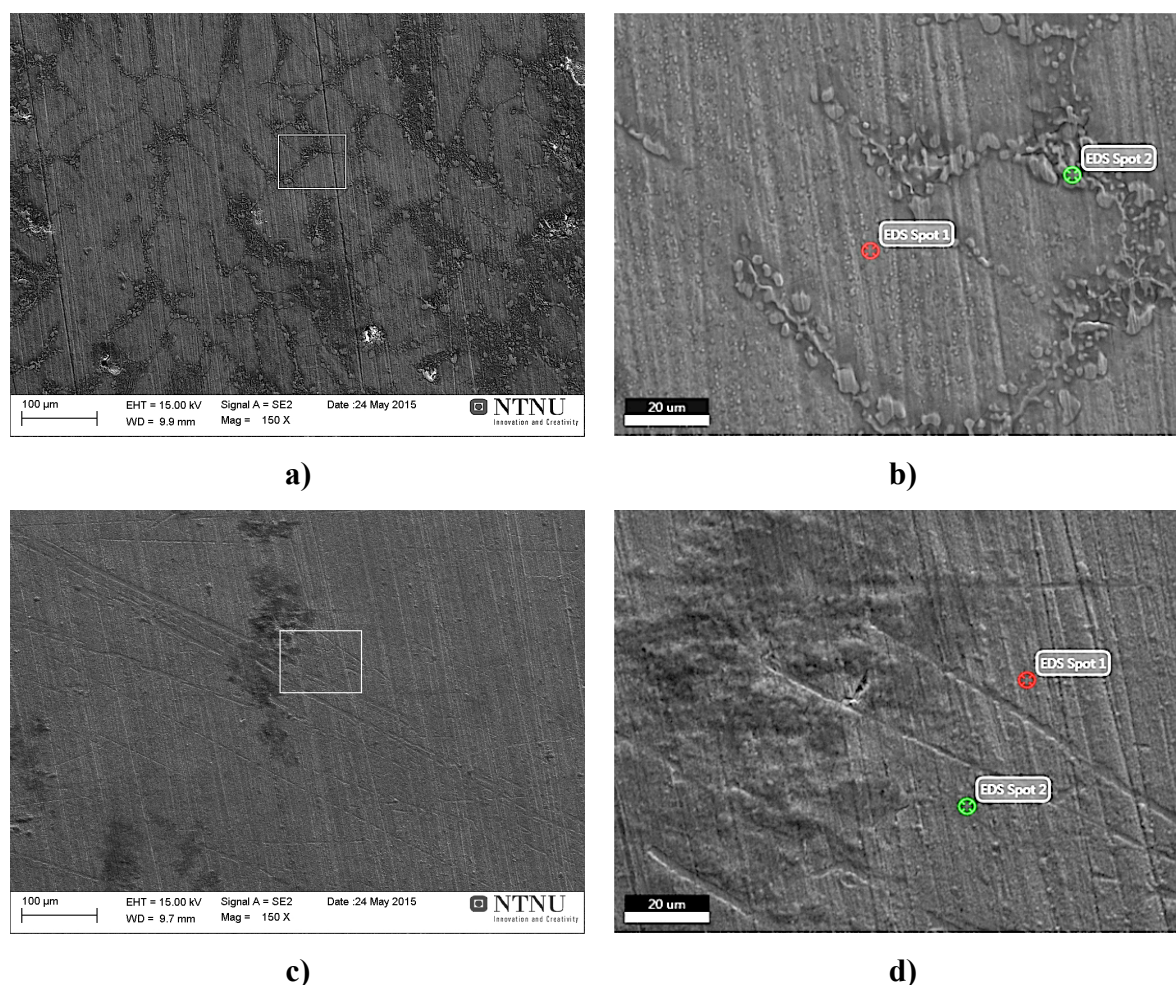

a)   b)
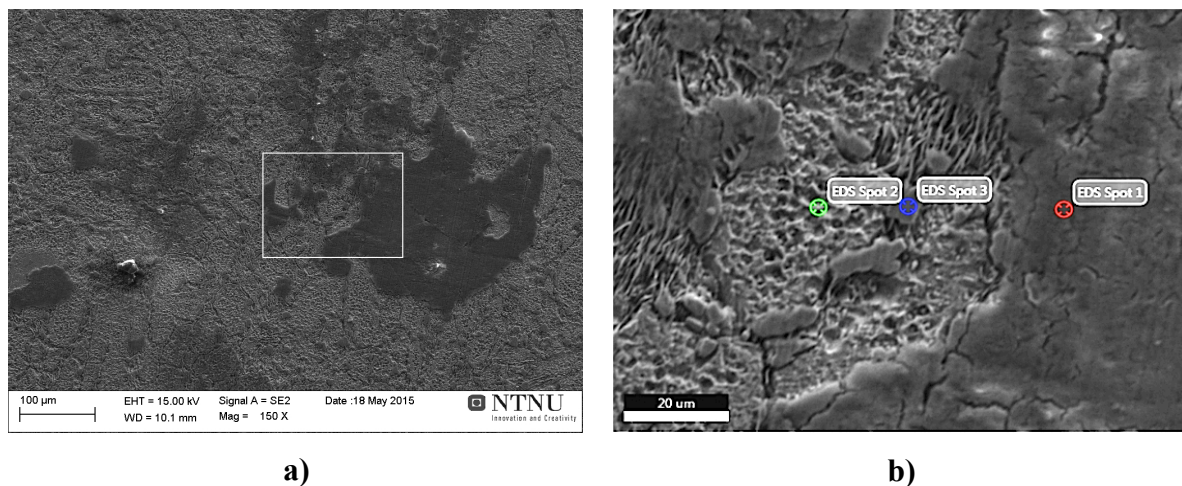
Figure 4.22 SEM images of freely exposed NAB after one week of immersion in SSW. Magnification of marked area in a) is shown in b). Spot 1,2 and 3 in b) refer to the sites where EDS were performed. The EDS analysis of spot 1 and 2 can be seen in Figure 4.23.


a)   b)

Figure 4.23 EDS analysis of a) spot 1 and b) spot 2 in Figure 4.22 b). The main constitutes are Cu, O, Al, and Fe in spot 1, and Cu and Al in spot 2. Spot 3 is not included.

50

Overview pictures of freely exposed NAB after one week of immersion in 10 ppmW and 100 ppmW sulphide-polluted SSW can be seen in Figure 4.24 a) and c), respectively. This corresponds to sample 23 and 25 in Table 3.5, respectively. Magnifications of marked areas are shown in Figure 4.24 b) and d), respectively, where surface grooves from grinding are apparent. The EDS analysis of the spots in Figure 4.24 b) is given in Figure 4.25, showing a clear variation in the main constituents between the two spots. The EDS analysis of spot 1 in Figure 4.24 d) is given in Figure 4.26, showing a very low content of oxygen of the surface film of NAB. Spot 1 and spot 2 revealed approximately the same EDS spectrum.
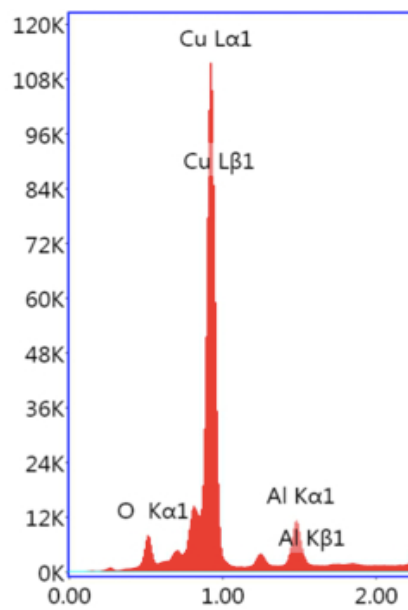

Figure 4.24 SEM images of freely exposed NAB after one week of immersion in SSW polluted with a) 10 ppmW and c) 100 ppmW sulphide. Magnifications of marked area in a) and c) are shown in b) and d), respectively. Spot 1 and 2 in b) and d) refer to the sites where EDS were performed, and the EDS spectrums are shown in Figure 4.25 and Figure 4.26, respectively.

a)

b)
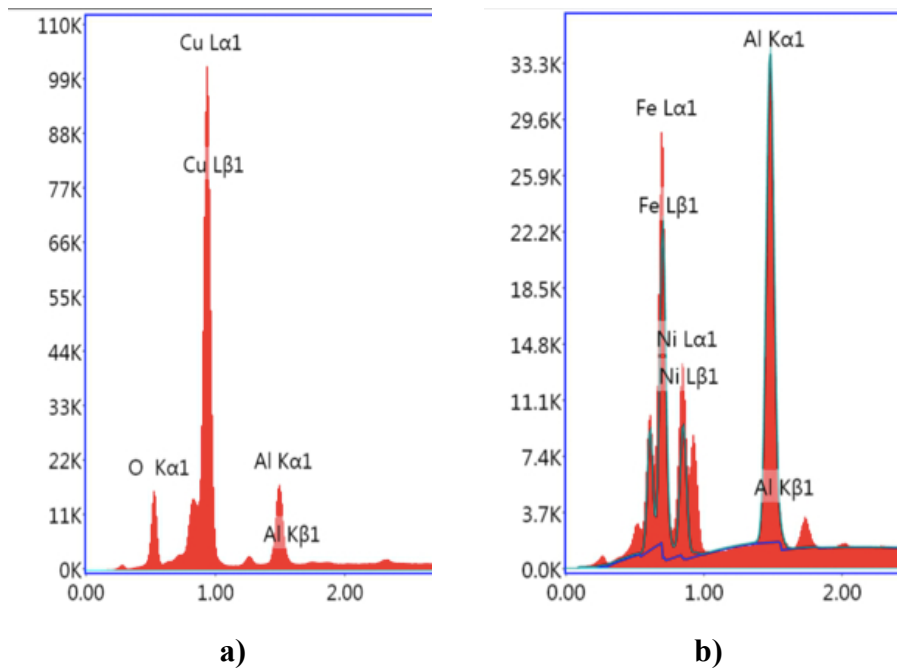
Figure 4.25 EDS analysis of a) spot 1 and b) spot 2 in Figure 4.24 b). The main constituents are Cu, O and Al in spot 1, and Al, Fe and Ni in spot 2.

Figure 4.26 EDS analysis of spot 1 in Figure 4.24 d). The main constituents are Cu, Al and O. Spot 1 and 2 revealed approximately the same EDS spectrum.

Figure 4.27 a) shows an overview picture of freely exposed NAB after nine weeks of immersion in natural seawater, followed by one week in 10 ppmW sulphide-polluted SSW. This corresponds to sample 29 is Table 3.5. The surface is very rough, and a corrosion crater might be observed in Figure 4.27 b).


a)   **b)**
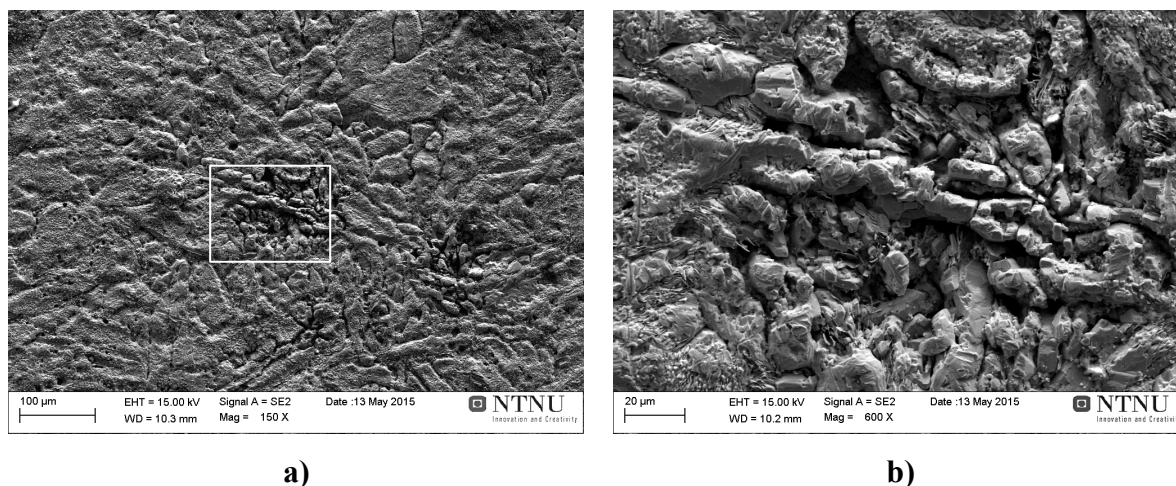
Figure 4.27 SEM images of freely exposed NAB after nine weeks of immersion in natural seawater, followed by one week in 10 ppmW sulphide-polluted seawater. Magnification of marked area in a) is shown in b).

4.5.3 Characterization of corrosion products by XRD analysis

An XRD analysis was performed to identify the composition of the corrosion products of NAB in both pure and 100 ppmW sulphide-polluted SSW. The X-ray diffractograms are shown in Figure 4.28 and Figure 4.29, respectively. XRD analysis revealed corrosion products consisting mainly of aluminum oxide and copper chloride. The corrosion products from the tests with sulphide-polluted SSW also contained copper sulphide.
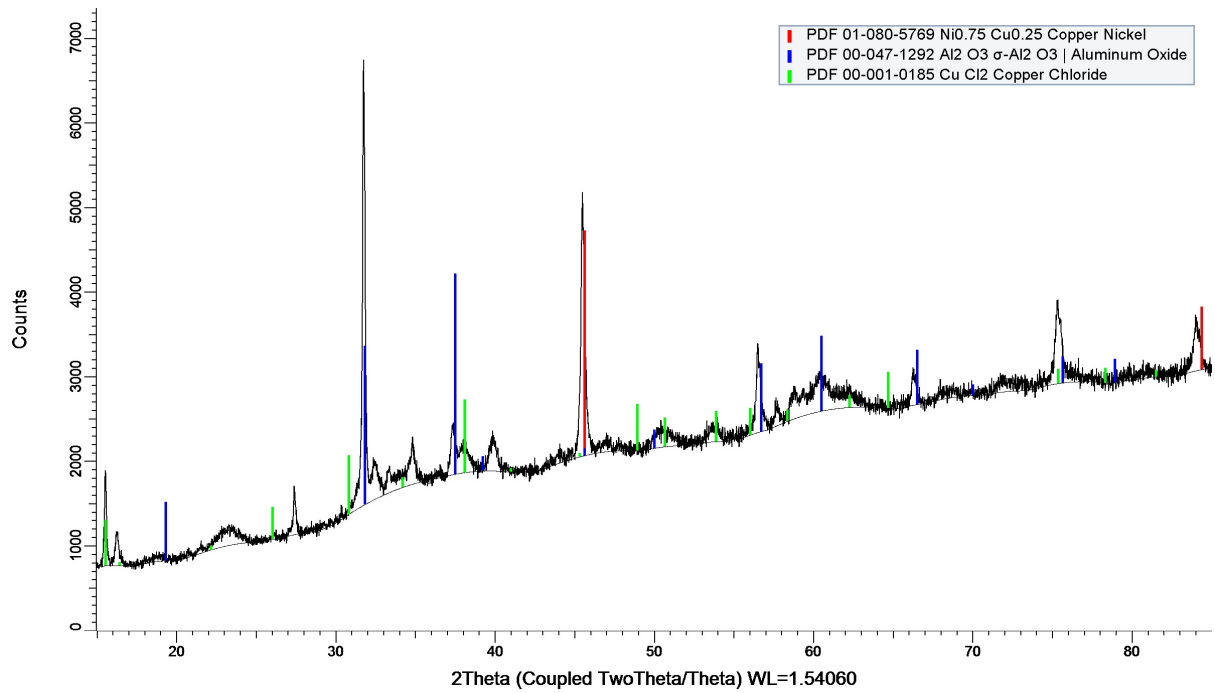
Figure 4.28 X-ray diffractogram of the corrosion products filtrated from the test solution after electrochemical measurements in pure SSW.
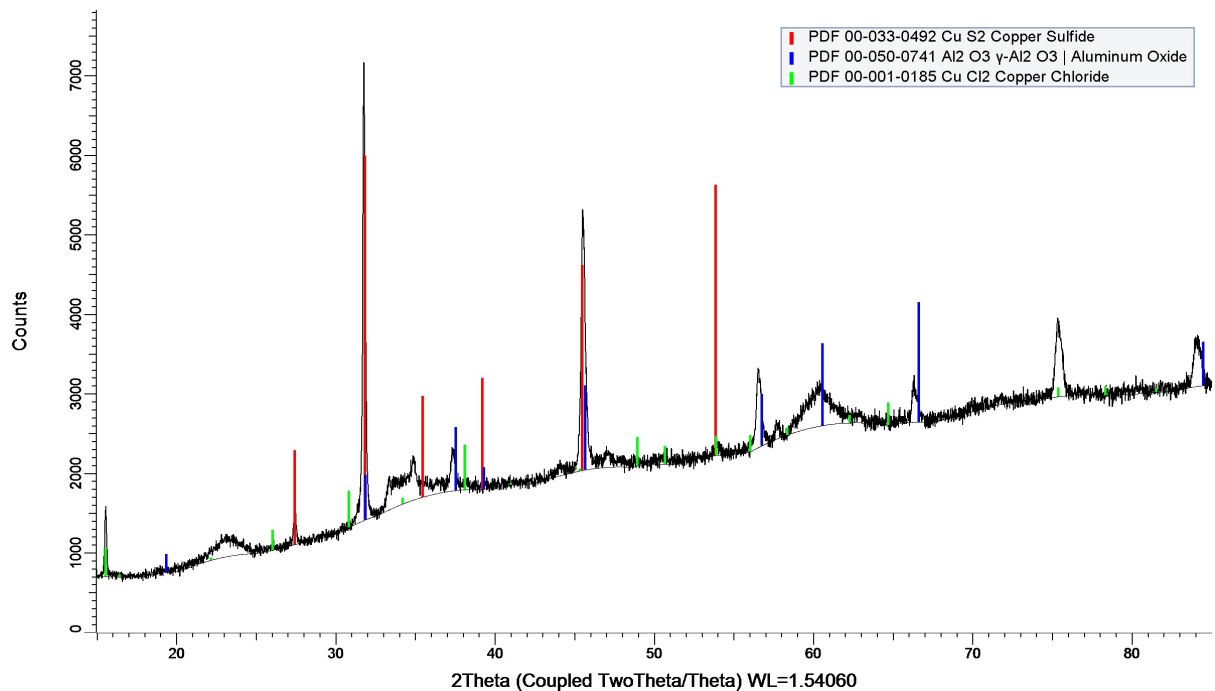
Figure 4.29 X-ray diffractogram of the corrosion products filtrated from the test solution after electrochemical measurements in 100 ppmW sulphide-polluted SSW.

5 Discussion

This section contains a discussion of the most interesting results obtained from the experimental work. The discussion is based on OCP measurements present in section 4.1, potentiodynamic polarization curves shown in section 4.3 and the values for corrosion current densities given in Table 4.5. Observations from electrochemical measurements are linked to the results from pH measurements and surface characterization. The corrosion properties of NAB in synthetic- and natural seawater are discussed first. Afterwards the effect of sulphide-pollution and MF is analysed. Evaluations of the experimental work and sources of error are given in the end, together with some suggestions for further work. All potentials mentioned in this section are given with respect to the Ag/AgCl reference electrode.

5.1 Synthetic- and natural seawater

5.1.1 The formation of a protective oxide layer

The OCP of NAB in natural seawater without an applied MF was measured to be -230 mV upon immersion, as shown in Figure 4.3. This is approximately similar to values reported in the literature for immersion of NAB in natural seawater [1]. The corrosion resistance of NAB is due to the ability to form an adherent, protective oxide film. In Figure 4.3, two sharp noble shifts in potential can be observed. The potential increases to approximately -195 mV by the 13th day, and is assumed to be due to the formation of a protective Cu_2O film, as shown in Equation (2.5). According to the Pourbaix diagram for pure copper in Figure 2.3, Cu_2O is the stable oxide at OCP in seawater with a pH of 8,2. By the 19th day the OCP increases to approximately -150 mV, and may be due to the transformation of Cu_2O to CuO, as shown in Equation (2.6). As the film thickness increases, the potential becomes more noble, i.e. more positive. However, after nine weeks of immersion the potential is still -150 mV. The stabilization of OCP may indicate that it has reached the potential at which atacamite, $Cu_2(OH)_3Cl$, is stable. Atacamite forms on the outside surface of the Cu_2O film, according to Equation (2.7), but will not contribute to further protection of NAB, due to its porosity.

5 Discussion

Visual inspection of NAB after nine weeks of immersion in natural seawater revealed a slightly grey blue corrosion film with no indication of pitting, as seen in Figure 4.15 a). According to the OCP measurements the sample should be covered by atacamite. This is not clearly observed in Figure 4.15 a), but might be due to the quality of the picture. However, the grey blue colour can be due to the CuO film, which covers the red brown Cu_2O layer. SEM images of the surface, see Figure 4.20, indicate a lot of white spots surrounded by a grey matrix. EDS analysis in Figure 4.21 revealed high content of oxygen in the white spots compared to the grey surfaces around, indicating the presence of an oxide layer. EDS also revealed high content of aluminium and copper, and it is assumed that the oxide layer also consist of aluminium oxide. The aluminium oxide is formed according to Equation (2.8). It is apparent that the oxide layer is not homogenous distributed on the surface. This is due to the complex microstructure of NAB, consisting of various phases with different electrochemical potential [1]. The most positive anodic phases will corrode preferentially and will be covered by corrosion products. Longer exposure time in natural seawater would have increased the amount of white spots. The reason why some areas appear white and other grey in the SEM pictures is due to topography.

XRD characterization of the corrosion products from testing in SSW, see Figure 4.28, revealed corrosion products mainly consisting of aluminium oxide and copper chloride. No copper oxides were detected, and this is not in agreement with the analysis of OCP measurements in natural seawater. The chemical composition of SSW and natural seawater is not similar, and might result in different corrosion products. Since NAB contains iron, the XRD analysis should be performed with fixed slit conditions, due to the fluorescence effect of iron. This will give more reliable results.

The anodic polarization curves of fresh, aged and long-term NAB in Figure 4.6 show quite similar trend as those reported in the literature [14]. A lower anodic current density is, however, observed for long-term NAB compared to fresh and aged NAB. This is due the protective, oxide film developed on the sample surface as discussed above. The anodic polarization curve of long-term NAB also shows evidence of a slight steep in the range of -40 to -50 mV, attributed with the transformation of Cu_2O to CuO, according to Equation (2.6). As the protective film becomes thicker, an ohmic drop arises across the corrosion product, resulting in an increased anodic Tafel slope [2, 14].

The cathodic polarization curves of fresh and aged NAB also show the same trend as those reported in the literature [2, 14]. However, several drops in cathodic current density are observed for long-term NAB. This is not the case for the fresh and aged samples. The cause of this is not clear, but might be due to oxidizing or reduction of the elements in the protective oxide layer. The fresh and aged samples will have a more homogenous surface compared with the long-term, due to a less complex oxide layer. It must also be mentioned that the polarization curve of long-term NAB was recorded manually, resulting in some variations in the test setup.

5.1.2 Analysis of corrosion rates

The corrosion current density of freely exposed long-term NAB in natural seawater was found to be 1,5 mA/m^2 by extrapolating the linear regions of the polarization curves, as seen in Figure 4.13. This corresponds to a uniform corrosion rate of 0,0019 mm/year, calculated from Faradays law given in Equation C.3 in Appendix C. This value is a little lower than the corrosion current density of 2,0 mA/m^2 in SSW reported by Schüssler [17], and the reported corrosion rate in natural seawater of 0,015 mm/year [23]. Individual variations in the experimental conditions might be the reason for the variation in test results. The corrosion current density obtained from LPR measurements was found to be 1,4 mA/m^2, see Table 4.5, by the Stern Geary Equation in Equation (C.1), indicating a good correlation between the two electrochemical methods.

Higher corrosion rate can be observed for fresh NAB in SSW compared to long-term NAB in Table 4.5. The corrosion rate is found to be 33 times higher for fresh NAB compared to long-term NAB, and is in good agreement with earlier work. Schüssler found that the corrosion rate decreased by a factor of 20-30 in the presence of a protective oxide layer [17]. The fresh samples were only exposed one hour in SSW prior to testing, and the time required to form a fully matured oxide layer is reported to be 2-3 months [18]. However, after one week of exposure to SSW the corrosion rate decreased by a factor of approximately three compared to one hour in SSW. This indicates that the initial film forms relatively quickly over the first couple of days, contributing to a certain protection of the underlying metal. As observed from the SEM images in Figure 4.22, a dark grey layer can be observed in between a grey matrix. EDS analysis showed that the main constituents in this layer are oxygen, aluminium and

copper, while elsewhere on the surface, oxygen was not detected. This supports the observations of initial formation of an oxide layer in SSW.

5.2. The effect of sulphide-pollution

5.2.1 Open circuit potentials and pH measurements

The measured OCP in sulphide-polluted SSW shows an interesting behaviour. When sulphide is added to SSW, the OCP dropped immediately to more negative values. As the sulphides react with copper to form Cu_2S, according to Equation (2.9), the OCP increases to a maximum value (steady state). From Figure 4.2, a relatively fast increase in potential is observed until the potential reaches steady state after approximately 9 hours and 19 hours in 10 ppmW and 100 ppmW sulphide-polluted SSW, respectively. The addition of $Na_2S \cdot xH_2O$ revealed a basic solution in the range of 8,3-9,6 depending on the sulphide content, as seen in Table 4.1. Na_2S is the conjugate base of the weak acid HS⁻, making Na_2S a strong base. The pH dropped to the pH of SSW after one week. Actually, the pH of SSW was reached during the first day, indicating that all the added sulphides had reacted with copper, i.e. all sulphides were consumed. Schüssler also reported an increase in OCP to more positive potentials when sulphide was added, due to the reduction of free copper ions in the electrolyte [4].

The steady state OCP in 100 ppmW is more negative than OCP in 10 ppmW sulphide-polluted SSW, as can be seen in Figure 4.2. This trend has been reported in the literature for copper alloys in 3% NaCl solution [26]. From Figure 4.1 it can be seen that the steady state OCP is not reached in sulphide-polluted SWW after one hour. The reaction between copper and sulphide is still in progress. However, in SSW the steady state OCP is reached relatively quickly.

5.2.2 Potentiodynamic polarization curves

The main difference between fresh NAB in pure SSW and sulphide-polluted SSW is the rate of charge transfer reactions of oxygen reduction, as seen in Figure 4.5 and Figure 4.7. In sulphide-polluted SSW the charge transfer reactions are accelerated, and the limiting cathodic current density is reached faster. This result is in agreement with the mechanism reported in

the literature [4]. The corrosion process becomes totally diffusion controlled, and is therefore sensitive to flow velocity. This trend is, however, not observed for aged NAB in sulphide-polluted SSW, as can be seen Figure 4.9. The sulphide attack seems to be dependent on the sample treatment.

The cathodic current density increases with increased sulphide content for aged NAB, as seen in Figure 4.9. For fresh NAB the limiting cathodic current density is approximately similar, independent of the sulphide content, as can be seen in Figure 4.8. Conversely, the anodic current density seems to decrease with higher sulphide content for both fresh and aged NAB. This is not in agreement with the observations found in literature, where the anodic current density was found to increase for higher concentrations of sulphide [26]. The corrosion properties in sulphide-polluted seawater are highly influenced by experimental conditions, and might be the reason for wide scatter in the observations [4].

The cathodic polarization curves of long-term NAB in 10 ppmW sulphide-polluted SSW, given in Figure 4.11, show an interesting behaviour. It seems like that the limiting cathodic current density is reached relatively fast, but as the potential decreases to more negative values, the cathodic current density starts to increase at about -510 mV and -396 mV with and without a MF, respectively. This is approximately –340 mV from OCP in both cases. The reason for this is not clear, but might be due to a shift to other cathodic reactions than oxygen reduction. A possible cathodic reaction is hydrogen reduction, but in aerated seawater this reaction normally happens at potentials lower than -800 mV vs Ag/AgCl. Hydrogen reduction reaction is for that reason not likely to occur in this case. The most reliable explanation is that the condition in the electrolyte is not constant, and that the limiting cathodic current density is not reached.

5.2.3 Analysis of corrosion rates

Table 4.5 shows relatively good correlations between the corrosion current densities of NAB obtained from LPR measurements and polarization curves. However, this is not true for the values found in 10 ppmW sulphide-polluted SSW without a MF for fresh and long-term NAB, as seen in Table 4.5. The reason might be due to the uncertainty of the construction of

overvoltage curves. The discussion of corrosion rate in this section is based on the values obtained from polarization curves, due to less uncertainty.

For long-term NAB, the corrosion current density increased by a factor of eight when placed in 10 ppmW sulphide-polluted SSW with an applied MF, compared to long-term NAB in natural seawater (1,5 mA/m^2). This indicates the incorporation of sulphides in the oxide layer, resulting in lower protection of the underlying metal. The corrosion rate of NAB after one week of immersion in sulphide-polluted SSW is actually lower than for fresh NAB in SSW. This is assumed to be due to the formation of a surface film, consisting of Cu_2S according to Equation 2.9, which will reduce the corrosion rate of NAB. Although being porous, the film will protect the underlying metal to some degree. This layer has been reported to be relatively thick, acting as a barrier for diffusion of oxygen to the surface, and hence decreases the rate of the cathodic reaction [26]. The corrosion rate decreases when the sulphide content is increased from 10 ppmW to 100 ppmW, as seen in Table 4.5, indicating a better protective layer. XRD characterization of the corrosion products from testing in 100 ppmW, see Figure 4.29, sulphide-polluted SSW revealed corrosion products mainly consisting of aluminium oxide, copper chloride and copper sulphide. In accordance to this analysis, it seems like Cu_2S will be present on the surfaces. Since NAB contains iron, the XRD analysis should be performed with fixed slit conditions to give more reliable information.

5.2.4 Surface characterization

Visual inspection revealed big differences in sample appearance after immersion in different sulphide content, as observed in Figure 4.14. The pictures are taken after one week of immersion. The sample surface was covered by a black film, which was poorly adhered to the metal and easily scratched off, after immersion in 1 ppmW sulphide-polluted SSW. After immersion in 10 ppmW sulphide-polluted SSW, the sample surface was covered by white, blue/greenish and brown corrosion products. Corrosion craters, up to about 200 μm deep, were observed beneath the white corrosion deposits, as can be seen in the 3D picture in Figure 4.19. From this figure it seems like the craters are quite wide, indicating that the craters to grow peripherally rather than laterally. This is in accordance with the pitting-like mechanism of NAB suggested by Lucey, showed in Figure 2.7 [27]. After immersion in 100 ppmW

sulphide-polluted SSW, the sample surface was covered by black, green and red brown corrosion products, but no corrosion craters were observed in 3D light microscope.

After cleaning, the sample appearance was quite similar for NAB immersed in 1 ppmW and 10 ppmW sulphide-polluted SSW, as seen in Figure 4.14 d) and e). A slightly darker appearance was observed after immersion in 10 ppmW, indicating the presence of an inner adherent layer. The corrosion products formed in sulphide-polluted seawater have been reported to consist of a porous outer layer and an inner strongly adherent layer of Cu_2S [4]. The sample immersed in 100 ppmW sulphide-polluted SSW showed a quite different appearance after cleaning, compared to the two others. A dark red surface with some black spots was observed in Figure 4.14 f). The red colour resembles a Cu_2O film. SEM images of the corroded surfaces after immersion in 10 ppmW and 100 ppmW sulphide-polluted SSW, shown in Figure 4.24, showed grooves from grinding. This was not evident after immersion in SSW and natural seawater, indicating a less protective layer after immersion in sulphide-polluted SSW. The EDS analysis of the corroded surfaces revealed a low content of oxygen, as seen in Figure 4.25 and Figure 4.26. No sulphide was detected either, and the EDS analysis is not in agreement with the observations from XRD analysis.

The sample appearance of long-term NAB after one week of immersion in 10 ppmW sulphide-polluted SSW, revealed a markedly change compared to the appearance right after immersion in natural seawater. This difference can be seen in Figure 4.15. Exposure in 10 ppmW sulphide-polluted SSW revealed a black film on the surface as shown in Figure 4.15 b). Greenish and red brown corrosion products, indicating atacamite and Cu_2O, were also observed on the greater part of the surface. Several corrosion craters were observed on the surface by 3D light microscopy, see Figure 4.18, indicating selective phase attack. SEM images of the corroded surface revealed a very rough surface, as showed in Figure 4.27 a), and several corrosion craters were found. This is in agreement with the observation by 3D light microscopy. A close up picture of one corrosion crater is present in Figure 4.27 b), where it appears quite wide. As mentioned above, Lucey reported that a pitting-like mechanism tends to occur beneath the corrosion deposits, resulting in a wide crater rather than deep [27].

5.3 The effect of magnetic field

5.3.1 Open circuit potentials

The measured potential-time values of fresh samples in Figure 4.1 indicate that a MF had no effect on OCP in pure SSW. In sulphide-polluted SSW, a weak shift to more negative values is observed in the presence of a MF upon immersion. However, after one hour of exposure the difference in OCP is only 8 mV, and the potential tends to increase with quite similar slope. It can be concluded that the MF had limited effect on OCP in sulphide-polluted SSW.

The effect of a MF is more pronounced for long-term samples in both natural seawater and sulphide-polluted SSW, as shown in Figure 4.3 and Figure 4.4, respectively. The steady state OCP is shifted in the cathodic direction, i.e. negative direction, upon application of a MF. In the literature, the reported effects of a MF on OCP of metals are controversial. The observations in this work are not in accordance with reported observations of iron and zinc immersed in KNO_3, where the OCP changed to more positive values when applying a MF [43]. However, the observations are in accordance with the reported change in OCP for Nd-Fe-B magnets in 3,5 % NaCl solution, where the OCP changed to more negative values when the samples were magnetized [44]. No available literature was found on the effect of a MF on OCP of copper alloys. These observations encourage further investigation of the effect of a MF on OCP of NAB, as it appears that a MF causes a shift in OCP.

The OCP of NAB in natural seawater in the presence of a MF was -220 mV upon immersion, as shown in Figure 4.3. A sharp noble shift in OCP to approximately -190 mV can be observed after eight days, and is assumed to be due to the formation of a protective Cu_2O film, as shown in Equation (2.5). Contrary to NAB immersed in natural seawater without a MF, only one noble shift in potential is observed in the presence of a MF. This might indicate that Cu_2O is stable. It was, however, not possible to differentiate between the two samples with and without a MF by any methods used for surface characterization after immersion in natural seawater.

5.3.2 Potentiodynamic polarization curves

Based on the observations from Figure 4.5 and Figure 4.7, the MF will not have a great affect on the polarization behaviour of fresh NAB in pure SSW or in 10 ppmW sulphide-polluted SSW. Only a slightly lower limiting cathodic current density is observed in the presence of an applied MF. This is not in accordance with available literature. Several authors have reported that a MF will cause an increased convection in the electrolyte, resulting in a decrease in the thickness of the Nernst diffusion layer [35, 38, 40]. This will cause an increase in the limiting cathodic current density, according to Equation (2.12). An aquarium pump was used in all experiments performed in the Corrosion Lab, preventing stagnant conditions. The test cell involving a MF contained approximately 2 litre electrolyte, and the aquarium pump might have suppressed the induced convection caused by the MF. This will be a source of error if the MF affects the transport of oxygen to the electrode surface. Oxygen molecules are paramagnetic, and the transportation of oxygen towards the electrode surface should therefore be affected by a MF [44]. If the MF affects charge transfer reactions, the aquarium pump should not be a source of error. The main contribution to the increased convection is the Lorentz force, but it has been reported to be 6-7 orders in magnitude smaller than the diffusion force arising from the concentration gradient [47]. The typical values of the magnetic forces acting in aqueous electrolytes are very small compared to the forces of migration and diffusion, as seen in Table 2.2. Probably, the driving force for diffusion and electromigration will exceed the magnetic forces listed in Table 2.2 in this case.

The polarization curves recorded for long-term NAB in 10 ppmW sulphide-polluted SSW showed quite similar trend, as observed in Figure 4.11. The big difference is the shift in OCP to more negative values in the presence of a MF, as discussed in section 5.3.1. A lower cathodic current density is observed in the presence of a MF also in this case.

5.3.3 Analysis of corrosion rates

The corrosion current density was found to be higher for fresh NAB placed in a MF than without a MF, as seen in Table 4.5. A MF is reported to increase the limiting cathodic current density, due to induced convection in the electrolyte. However, this is not true in this case due to observations from the polarization curves, see section 5.3.2. The accelerated corrosion

might be due to increased rates of charge transfer reactions. Further investigation is required to support this observation.

5.4 Sources of error

The potentiostat was quite sensitive to noise, especially at low current, and the noise was removed in Excel prior to plotting. In this work, two different test setups were used for electrochemical measurements, i.e. with and without an applied MF. The test cell involving a MF contained less electrolyte than the test cell without a MF. The use of an aquarium pump may be a source of error in tests involving a MF. In some tests, several samples were placed in the same container, due to limited test setup. This procedure has to be improved. In this work, sulphide content of 1, 10 and 100 ppmW were investigated. This is quite small quantities, and uncertainties are related to the weight out procedure of $Na_2S \cdot xH_2O$.

5.5 Suggestions for further work

More testing is required to document the synergy effects of MF and sulphide-pollution on corrosion behaviour of NAB in seawater. The strength of the MF should be increased, and the tests should be performed with different orientation of the electrode surface with respect to the magnetic flux lines. It would also be interesting to study the effect of higher sulphide content. Sulphide can also be added to SSW multiple times (cyclic) to examine the effect on OCP. Sulphide should be added while the sample is polarized to -50 mV vs Ag/AgCl, which is the potential of NAB when galvanic coupled to AISI 316. Potentiostatic experiments should be performed in both the anodic and cathodic regime, to see if there is any change in the anodic or cathodic current with and without MF.

To be able to make strong conclusions, the experimental conditions should be as similar as possible in all tests, and several replicates for each test conditions are recommended. The corrosion process in sulphide-polluted seawater is strongly influenced by the experimental conditions, and a rotating disc electrode should be used for electrochemical measurements. This will provide more reliable polarization curves. The effect of sulphide-pollution on corrosion behaviour is also dependent on the content of oxygen. Tests in both aerated and

deaerated sulphide-polluted SSW should be performed. It would also be interesting to run tests in more operational like environment, e.g. lower temperature and longer time frame. In this work, long-term experiments were only performed in natural seawater. In further investigation, long-term experiments should also be performed in sulphide-polluted seawater, along with the application of a MF.

6 Conclusions

The corrosion behaviour of NAB in natural seawater, pure and sulphide-polluted SSW was investigated. The effect of an applied MF in the range of 0,15-0,28 Tesla was also studied. Results from the experimental work revealed the following remarks:

- A protective oxide layer was developed on the surface of NAB after nine weeks of immersion in natural seawater. The corrosion current density was found to be 1,5 mA/m^2 without a MF.
- Two sharp noble shifts in OCP were observed for NAB during exposure in natural seawater, indicating the formation of a protective oxide layer. Only one sharp noble shift in OCP was observed in the presence of a MF.
- The corrosion rate of NAB increased by a factor of 33 for fresh NAB compared to long-term NAB in unpolluted seawater.
- The MF had limited effect on OCP for fresh NAB in both pure and sulphide-polluted SSW.
- The MF had an effect on OCP for long-term NAB both in natural seawater and sulphide-polluted SSW. The OCP was shifted in the negative direction in the presence of a MF.
- The corrosion rate of NAB increased in the presence of a MF. However, a slightly lower limiting cathodic current density was observed in a MF.
- OCP was shifted to more positive values when sulphide was added to SSW, due to the formation of copper sulphide.
- The addition of sulphide to SSW revealed a basic solution in the range of 8,3-9,6 depending on the sulphide content.
- The rate of the charge transfer of the oxygen reduction reaction increased when sulphide was added to SSW.
- The corrosion rate of fresh NAB increased in sulphide-polluted SSW.
- The corrosion rate of NAB was found to be higher in 10 ppmW than 100 ppmW sulphide-polluted SSW after one week of immersion.
- Several corrosion craters were observed beneath the corrosion deposits after immersion in 10 ppmW sulphide polluted SSW.

7 References

1.   Meight, H., *Cast and Wrought Aluminium Bronzes Properties, Processes and Structure* 2000, London.

2.   Oakley, R.S., J.C. Galsworthy, and G.S. Fox, *Long-term and accelerated corrosion testing methods for cast nickel-aluminium bronzes in seawater*, in *Corrosion behaviour and protection of copper and aluminium alloys in seawater*. 2007, Woodhead Publishing. p. 119-127.

3.   Association, C.D., *Aluminium Bronze Alloys Corrosion Resistance Guide* **80**.

4.   Schüssler, A. and H.E. Exner, *The corrosion of nickel-aluminium bronzes in seawater—II. The corrosion mechanism in the presence of sulphide pollution.* Corrosion Science, 1993. **34**(11): p. 1803-1815.

5.   Powell, C. and P. Webster, *Copper Alloys for Marine Environments* 2012. **206**.

6.   Metall, O., *Material spec. omc 65025018, Nickel-Aluminium Bronze.* 2008.

7.   Wharton, J.A. and K.R. Stokes, *The influence of nickel–aluminium bronze microstructure and crevice solution on the initiation of crevice corrosion.* Electrochimica Acta, 2008. **53**(5): p. 2463-2473.

8.   Al-Hashem, A. and W. Riad, *The role of microstructure of nickel–aluminium–bronze alloy on its cavitation corrosion behavior in natural seawater.* Materials Characterization, 2002. **48**(1): p. 37-41.

9.   Solberg, J.K., *Aluminiumbronse*, in *Teknologiske metaller og legeringer*. 2014. p. 263-264.

10.   Wharton, J.A., et al., *The corrosion of nickel–aluminium bronze in seawater.* Corrosion Science, 2005. **47**(12): p. 3336-3367.

11.   Neodo, S., et al., *Electrochemical behaviour of nickel–aluminium bronze in chloride media: Influence of pH and benzotriazole.* Journal of Electroanalytical Chemistry, 2013. **695**(0): p. 38-46.

12.   Culpan, E.A. and G. Rose, *Microstructural characterization of cast nickel aluminium bronze.* Journal of Materials Science, 1978. **13**(8): p. 1647-1657.

13.   Bardal, E., *Korrosjon og korrosjonsvern.* 1985: Tapir Akademiske Forlag.

14.   Barik, R.C., et al., *The Environmental Factors Affecting the Performance of Nickel Aluminum Bronze.* 2004, NACE International.

15.   Barik, R.C., J.A. Wharton, and R.J.K. Wood, *Galvanic corrosion of nickel-aluminium bronze coupled to titanium or Cu-15Ni alloy in brackish seawater*, in *Corrosion behaviour and protection of copper and aluminium alloys in seawater*. 2007, Woodhead Publishing

7 References

16.   Moon, S.M. and S.I. Pyun, *The corrosion of pure aluminium during cathodic polarization in aqueous solutions.* Corrosion Science, 1997. **39**(2): p. 399-408.

17.   Schüssler, A. and H.E. Exner, *The corrosion of nickel-aluminium bronzes in seawater—I. Protective layer formation and the passivation mechanism.* Corrosion Science, 1993. **34**(11): p. 1793-1802.

18.   Johnsen, R., *Experience with the use of copper alloys in seawater systems on the Norwegian Continental Shelf,* in *Corrosion behaviour and protection of copper and aluminium alloys in seawater.* 2007, Woodhead Publishing p. 62-72.

19.   Al-Hashem, A., et al., *Cavitation Corrosion Behavior of Cast Nickel-Aluminum Bronze in Seawater.* Corrosion, 1995. **51**(5): p. 331-342.

20.   Zhang, X.-F. and L. Fang, *The effect of stacking fault energy on the cavitation erosion resistance of α-phase aluminum bronzes.* Wear, 2002. **253**(11–12): p. 1105-1110.

21.   Stachowiak, G.W. and A.W. Batchelor, *11 - Abrasive, Erosive and Cavitation Wear,* in *Engineering Tribology (Third Edition),* G.W.S.W. Batchelor, Editor. 2006, Butterworth-Heinemann: Burlington. p. 501-551.

22.   Dieter, G.E., *Strengthening Mechanisms* in *Mechanical Metallurgy* 1988.

23.   Tuthill, A., *Guidelines for the use of copper alloys in seawater.* NiDI Publication, 1988. **12003**.

24.   Wood, R.J.K., *Erosion-corrosion interactions of copper and aluminium alloys,* in *Corrosion behaviour and protection of copper and aluminium alloys in seawater.* 2007, Woodhead Publishing. p. 19-44.

25.   Reddy, A.V., et al., *Correlation between erosion behaviour and stacking fault energy in copper alloys.* Acta Metallurgica, 1984. **32**(9): p. 1305-1316.

26.   Rahmouni, K., et al., *Corrosion of copper in 3% NaCl solution polluted by sulphide ions.* Corrosion Science, 2005. **47**(12): p. 3249-3266.

27.   Lucey, V.F., *Developements Leading to the Present Understanding of the Mechanism of Pitting Corrosion of Copper.* Br. Corros. J. , 1971. **7**.

28.   Al-Hajji, J.N. and M.R. Reda, *The corrosion of copper-nickel alloys in sulfide-polluted seawater: the effect of sulfide concentration.* Corrosion Science, 1993. **34**(1): p. 163-177.

29.   El-Sayed, N.H. and M.M. El-Rabiei, *Effect of sulfide pollution on the stability of Cu–Al–5Ni alloy in 3.5% NaCl solution.* Egyptian Journal of Petroleum, 2014. **23**(2): p. 163-168.

30.   Eiselstein, L.E., et al., *The accelerated corrosion of CuNi alloys in sulphide-polluted seawater: Mechanism no. 2.* Corrosion Science, 1983. **23**(3): p. 223-239.

31.   Kelly, E.J., *Magnetic Field Effects on Electrochemical Reactions Occuring at Metal/ Flowing- Electrolyte Interfaces.* Electrochem. Soc. , 1977. **124**(7): p. 987-994.

32.   Chiba, A., et al., *The effects of magnetic fields on the corrosion of aluminum foil in sodium chloride solutions.* Corrosion Science, 1994. **36**(3): p. 539-543.

33.   M.E, G., S. G.H, and M. I.A.S, *Effect of a Magnetic Field on the Rate of Diffusion-Controlled Corrosion of Metals* 1982. **17**(1): p. 36-37.

34.   Hinds, G., J.M.D. Coey, and M.E.G. Lyons, *Influence of magnetic forces on electrochemical mass transport.* Electrochemistry Communications, 2001. **3**(5): p. 215-218.

35.   S.R, R., G. K.M, and W. H.S, *Electrochemically Generated Magnetic Forces. Enhanced Transport of a Paramagnetic Redox Species in Large, Nonuniform Magnetic Fields* J. Am. Chem. Soc., 1998. **120**: p. 13461-13468.

36.   Tacken, R.A. and L.J.J. Janssen, *Applications of magnetoelectrolysis.* Journal of Applied Electrochemistry, 1995. **25**(1): p. 1-5.

37.   Weier, T., et al., *Confinement of paramagnetic ions under magnetic field influence: Lorentz versus concentration gradient force based explanations.* Electrochemistry Communications, 2007. **9**(10): p. 2479-2483.

38.   Roubidoux, J., B. Mishra, and D.L. Olson, *Measurement of the Effect of Magnetization on Hydrogen Cracking Susceptibility of Pipeline Steels.* 2010.

39.   Nisancioglu, K., *Corrosion basics and engineering.*

40.   Tacken, R.A. and L.J.J. Janssen, *Applications of magnetoelectrolysis* Journal of Applied Electrochemistry, 1995. **25**: p. 1-5.

41.   Lu, Z. and W. Yang, *In situ monitoring the effects of a magnetic field on the open-circuit corrosion states of iron in acidic and neutral solutions.* Corrosion Science, 2008. **50**(2): p. 510-522.

42.   Devos, O., et al., *Is There a Magnetic Field Effect on Electrochemical Kinetics?* J. Phys. Chem. A, 2000. **104,**: p. 1544-1548.

43.   Coey, J.M.D. and F.M.F. Rhen, *Magnetic Field Induced Modulation of Anodic Area: Rest Potential Analysis of Zn and Fe.* J. Phys. Chem. C, 2007. **111**: p. 3412-3416.

44.   Costa, I., et al., *The effect of the magentic field on the corrosion behaviour of Nd-Fe-B permanent magnets.* Journal of Magnetism and Magnetic Materials, 2003. **278**: p. 348-358.

45.   Johnsen, R., *Cathodic Protection.* 2011.

46.   ASTM, *D 1141-98 Standard Practice for the Preparation of Substitute Ocean Water.* 2013.

47.   Bund, A., et al., *Magnetic field effects in electrochemical reactions.* Electrochimica Acta, 2003. **49**(1): p. 147-152.

Appendices

Appendix A Material datasheet

OSHAUG METALL

COPPERSTORM®

MATERIALSPESIFIKASJON OMC 65025018	MATERIAL SPEC. OMC 65025018
NIKKELALUMINIUMBRONSE	NICKEL-ALUMINUM BRONZE
Utg. C, 2010	Issue C, 2010

Denne spesifikasjon beskriver	This specification identifies
Støpt NiAl-Bronse CuAl10Fe5Ni5	Cast NiAl-Bronze CuAl10Fe5Ni5
iflg. NS-EN 1982:2008.	according to EN 1982:2008.

For krav som ikke er spesifisert
nedenfor gjelder NS-EN 1982:2008.

Navn	Castings EN 1982 - CuAl10Fe5Ni5-C - GS	
Designation		Castings EN 1982 - CuAl10Fe5Ni5-C - GS
Leveringsform	Sandstøpt gods	
Form of Delivery		Sand cast
Leveringstilstand	Støpt emne	
State of Delivery		As cast

Mekaniske egenskaper					Mechanical properties
Strekkfasthet / Ult. tensile strenght	R_m	min.	650	N/mm^2	
Flytegrense / Yield strength	$R_{p0,2}$	min.	250	N/mm^2	
Forlengelse / Elongation	A_5	min.	18	%	
Hardhet / Hardness		min.	140	HB	

Kjemisk sammensetting % [1] [2]   Chemical composition % [1] [2]

	Al	Cr	Cu	Fe [3]	Mg	Mn	Ni [3]	Pb	Si	Sn	Zn
min	9,0		79,0	4,0		0,5	4,5				
max	10,0	0,005	81,5	5,0	0,04	1,0	5,5	0,02	0,05	0,08	0,20

1) Sum Cr, Mg, Pb, Si, Sn, Zn og andre ikke angitte 0,3% maks.	1) Total content of Cr, Mg, Pb, Si, Sn, Zn and other not mentioned, shall not exceed 0,3%
2) H^2-innholdet i blokker ≤ 1ppm.	2) Content of H^2 in ingots ≤ 1ppm.
3) %Ni / %Fe	3) %Ni / %Fe

Erstatter: Utg. B	15.4.2010	Replaces: Issue B

Appendix B Open circuit potentials

Sample #	OCP [mV]		Sample #	OCP [mV]	
	Before	**After**		**Before**	**After**
1	-223	-240	**19**	-254	-151
2	-211	-224	**20**	-256	-154
3	-223	-234	**21**	-230	-150
4	-226	-232	**22**	-270	-65,63
5	-226	-209	**23**	-275	-64,41
6	-213	-198	**24**	-769	-80,68
7	-274	-202	**25**	-773	-75,18
8	-250	-203	**26**	-220	-190
9	-245	-198	**27**	-229	-150
10	-219	-182	**28**	-229	-150
11	-260	-209	**29**	-229	-49,5
12	-272	-206	**30**	-229	-45,4
13	-221	-200	**31**	-229	-50,7
14	-222	-200	**32**	-229	-46,5
15	-221	-207	**33**	-229	-169
16	-222	-209	**34**	-229	-113
17	-226	-189	**35**	-229	-172
18	-230	-188			

Appendix C Calculations

The corrosion current density, i_{corr}, can be calculated by Stern Geary equation given in Equation (C.1) [39]:

$$i_{corr} = \frac{b_a |b_c|}{2.3(b_a + |b_c|)R_P} \qquad \text{(C.1)}$$

where b_a and b_c are the anodic and cathodic Tafel slope, respectively, estimated from the polarization curves. R_P is the polarization resistance measured by LPR measurements, and is given in Equation (C.2) :

$$R_P = \frac{\Delta E}{\Delta I} A \qquad \text{(C.2)}$$

where $\Delta E/\Delta I$ is the slope of the curve obtained from LPR measurements, and A is the area of the sample.

The corrosion rate, CR, can be calculated from i_{corr} by Faradays law given in Equation (C.3):

$$CR = \frac{M}{nF\rho} i_{corr} \qquad \text{(C.3)}$$

where M is the molare mass, ρ is the density, n is the number of electrons transferred and F is the Faradays constant. The value used in this work can be seen in Table C.1.

Table C.1 Values for the parameters used to calculate the corrosion rate by Faradays law.

Parameter	Value
M [g/mole]	59,5 [14]
ρ [g/cm^3]	7,6 [1]
n	2
F [C/mole]	96485

Appendix D Potentiodynamic polarization curves

Figure D.1-D.15 present the potentiodynamic polarization curves of NAB under different experimental conditions, according to the test matrix in Table 3.5. The parallel tests for each condition are plotted in the same figure. The notation sample corresponds to the test matrix given in Table 3.5.
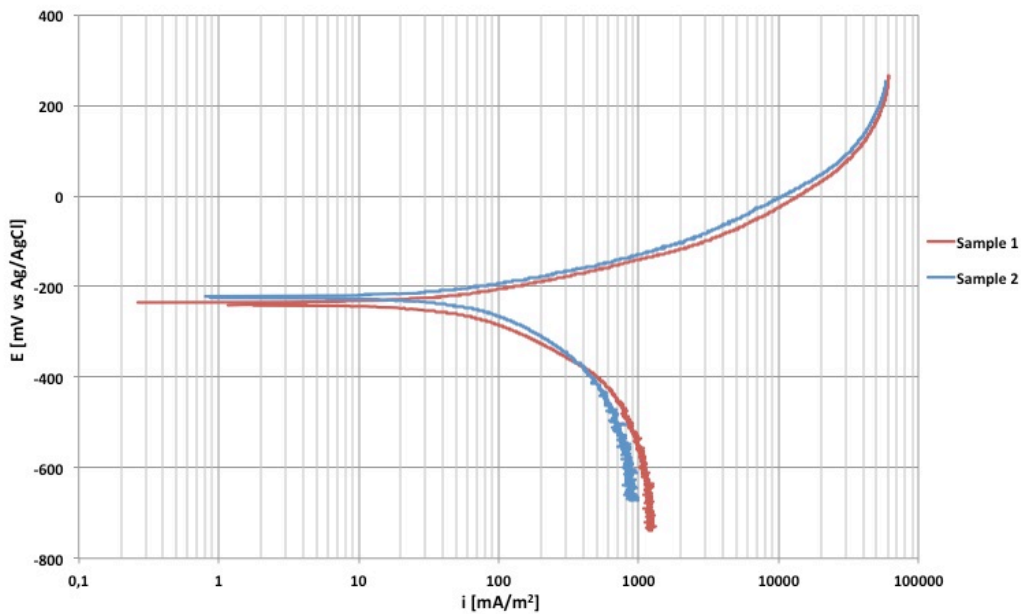

Figure D.1 Polarization curves of fresh NAB in SSW without an applied MF.

Figure D.2 Polarization curves of fresh NAB in SSW with an applied MF.
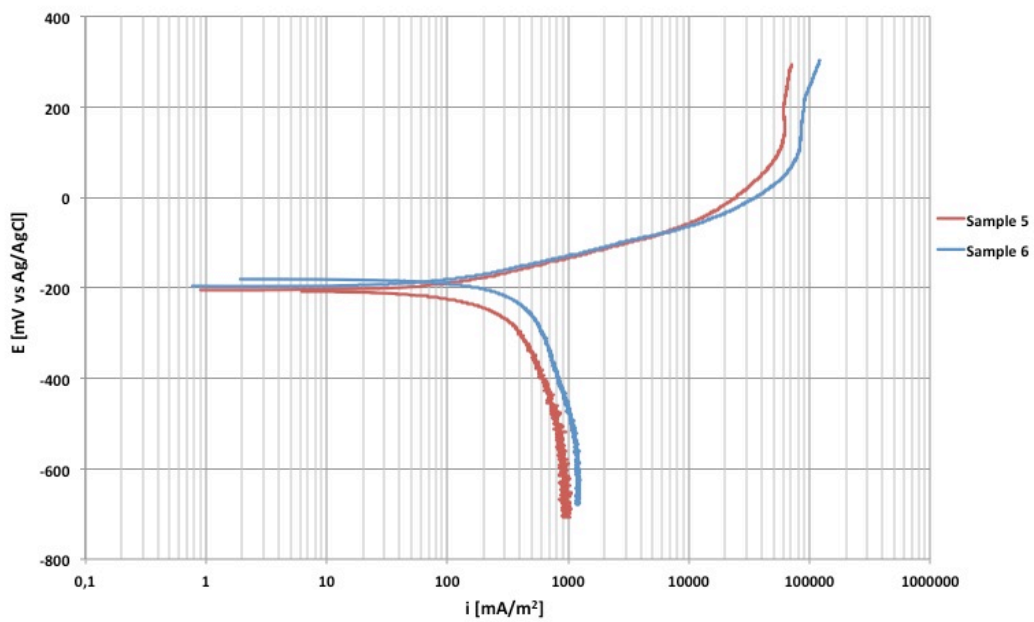
Figure D.3 Polarization curves of fresh NAB in 1 ppmW sulphide-polluted SSW without an applied MF.
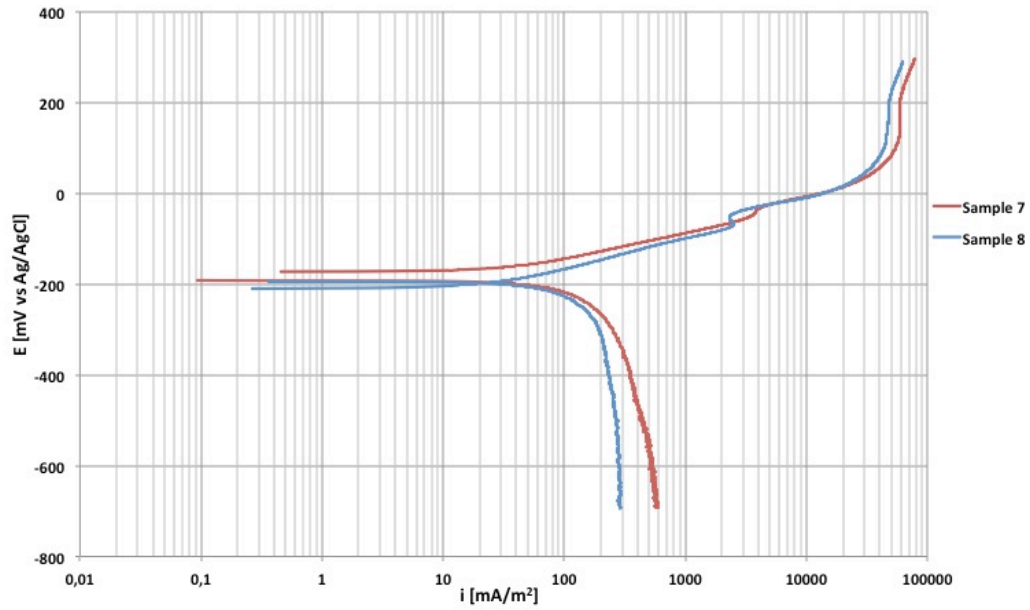
Figure D.4 Polarization curves of fresh NAB in 10 ppmW sulphide-polluted SSW without an applied MF.
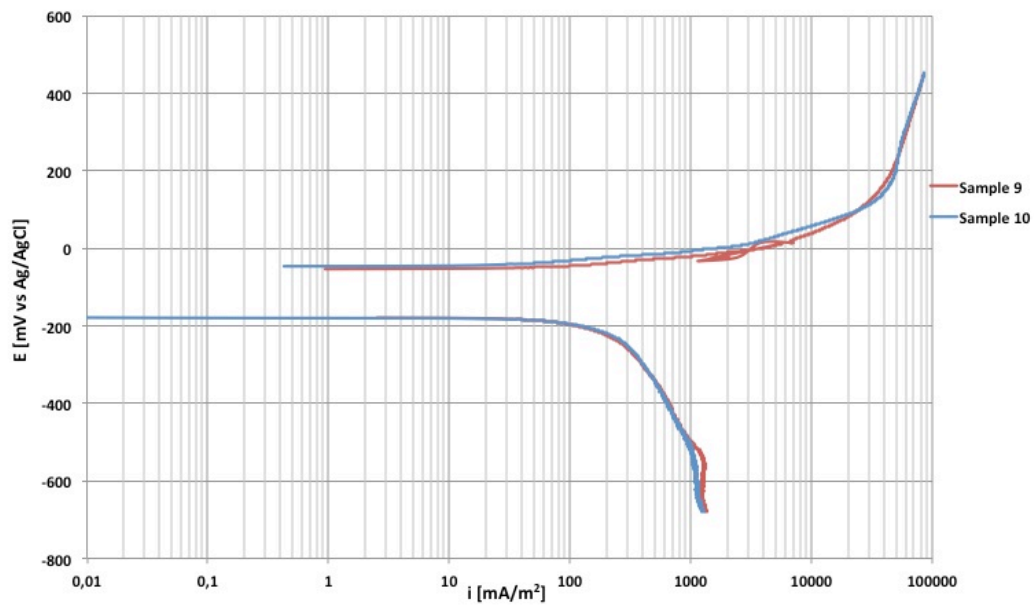
Figure D.5 Polarization curves of fresh NAB in 100 ppmW sulphide-polluted SSW without an applied MF.

Appendix D Potentiodynamic polarization curves
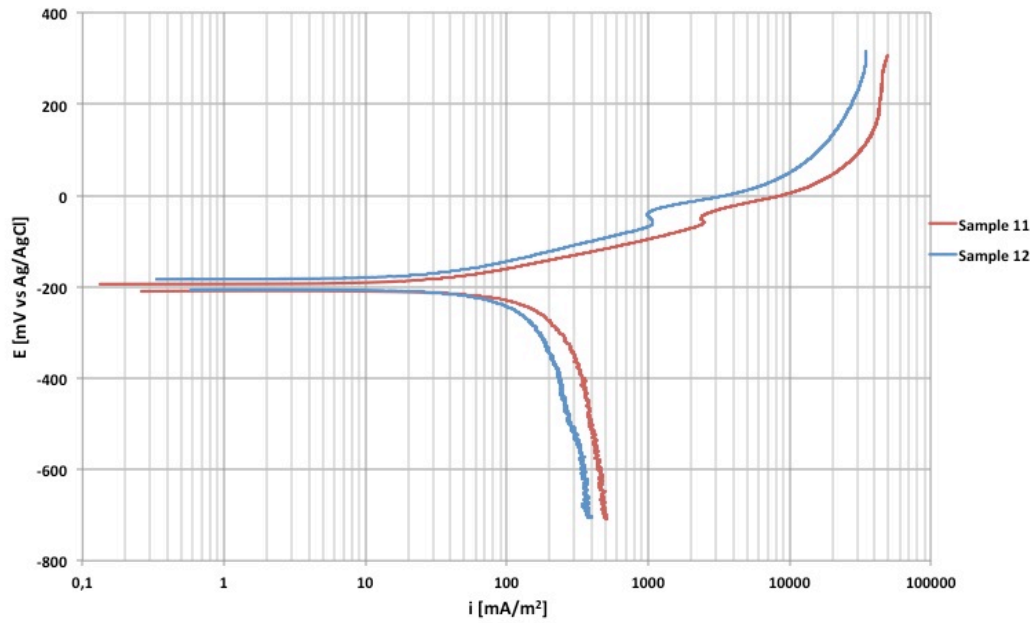
Figure D.6 Polarization curves of fresh NAB in 10 ppmW sulphide-polluted SSW with an applied MF.
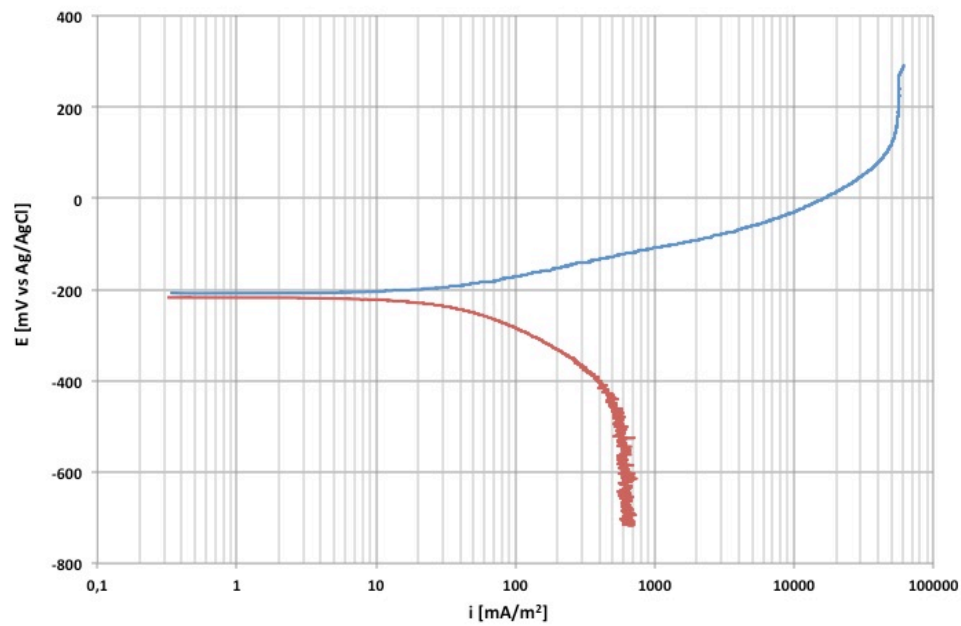
Figure D.7 Polarization curve of aged NAB in SSW without an applied MF (sample 13).
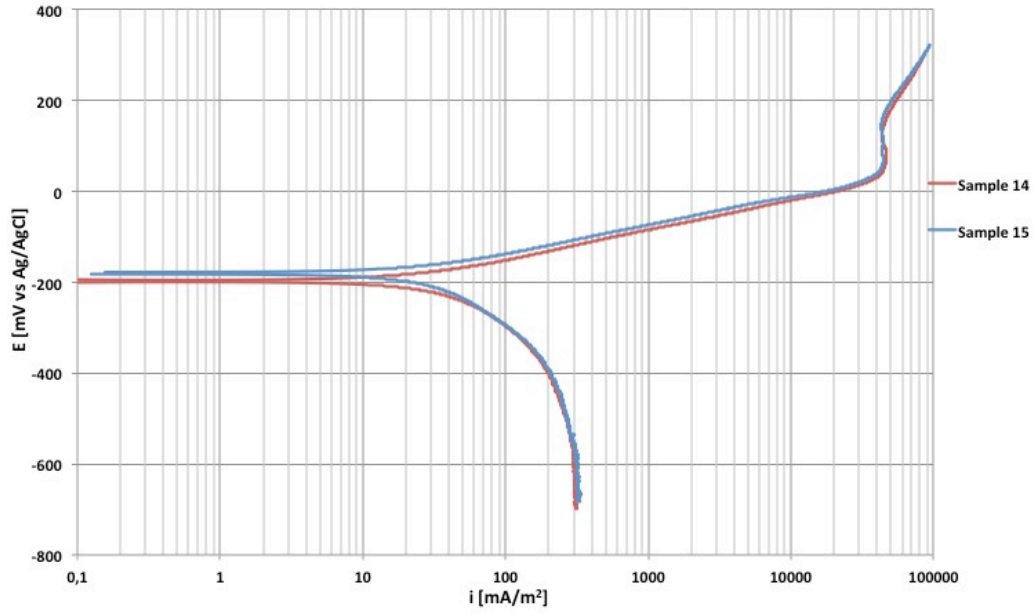
Figure D.8 Polarization curves of aged (SSW) NAB in SSW with an applied MF.
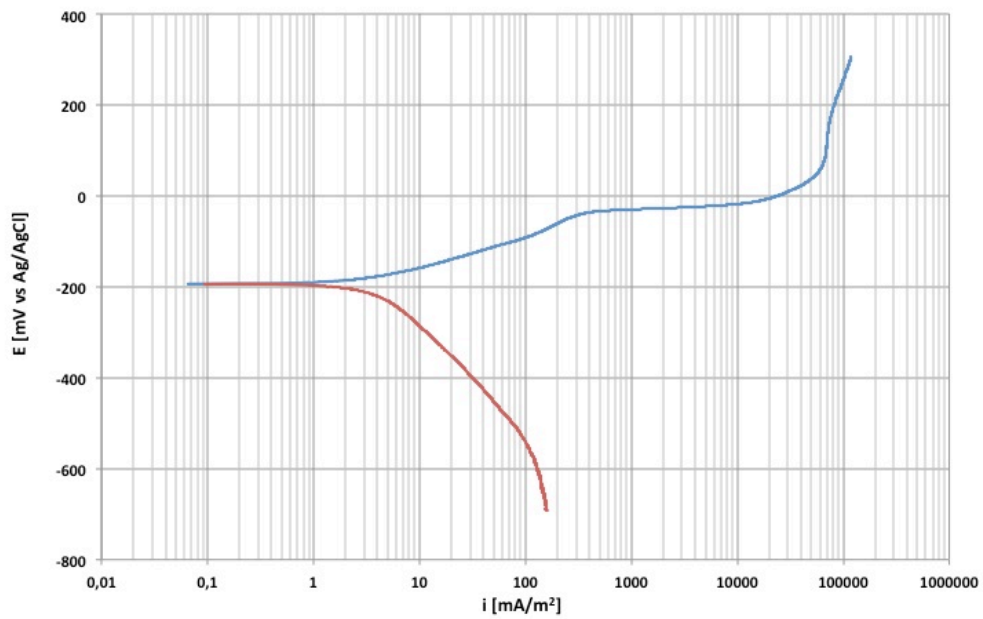
Figure D.9 Polarization curve of aged (1 ppmW S) NAB in 1 ppmW sulphide-polluted SSW with an applied MF (sample 17).
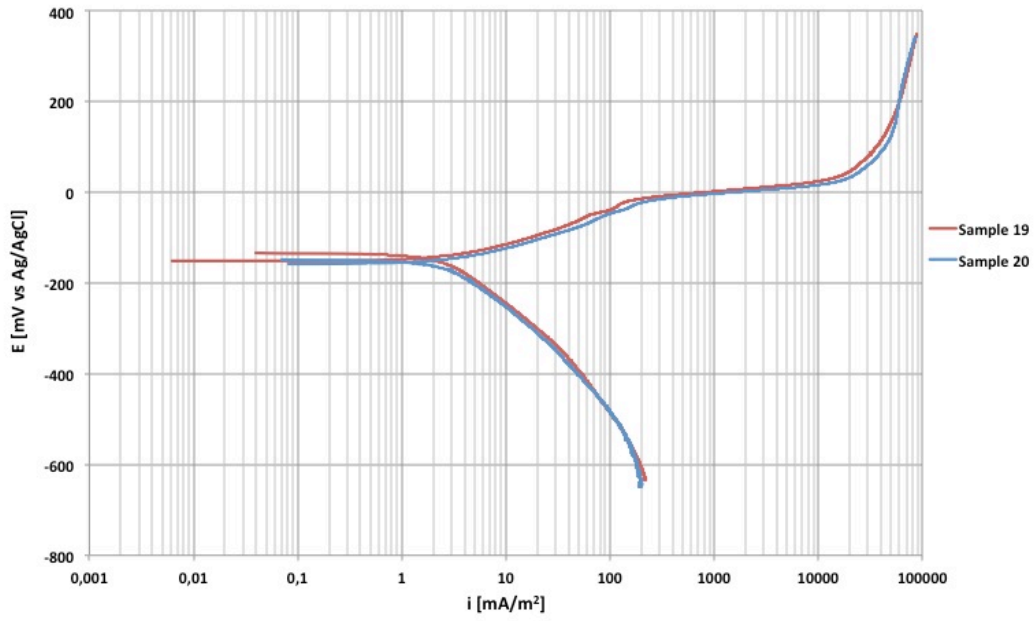
Figure D.10 Polarization curves of aged (1 ppmW S) NAB in 1 ppmW sulphide-polluted SSW without an applied MF.
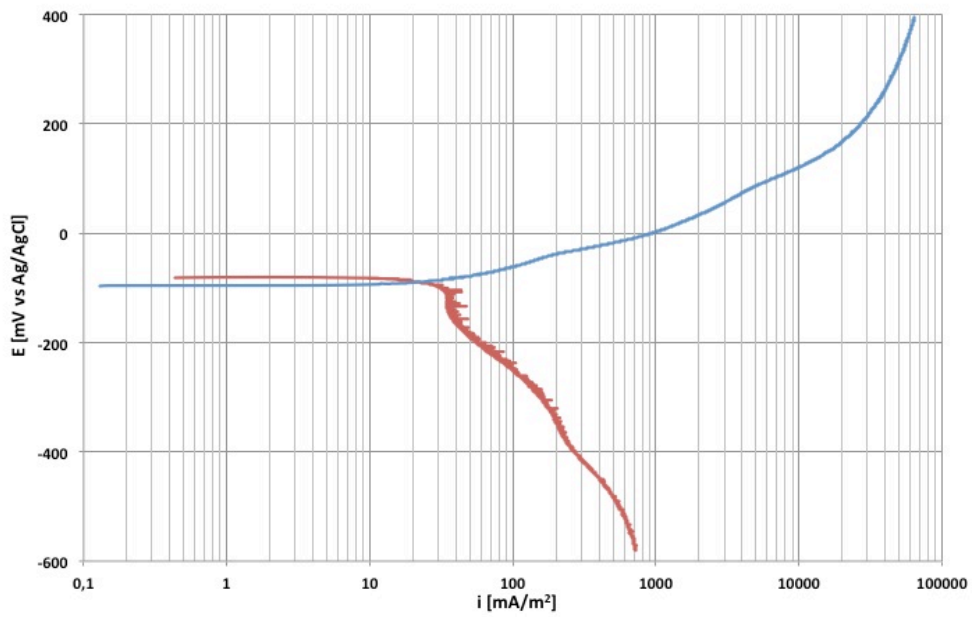
Figure D.11 Polarization curve of aged (10 ppmW S) NAB in 10 ppmW sulphide-polluted SSW without an applied MF (sample 22).
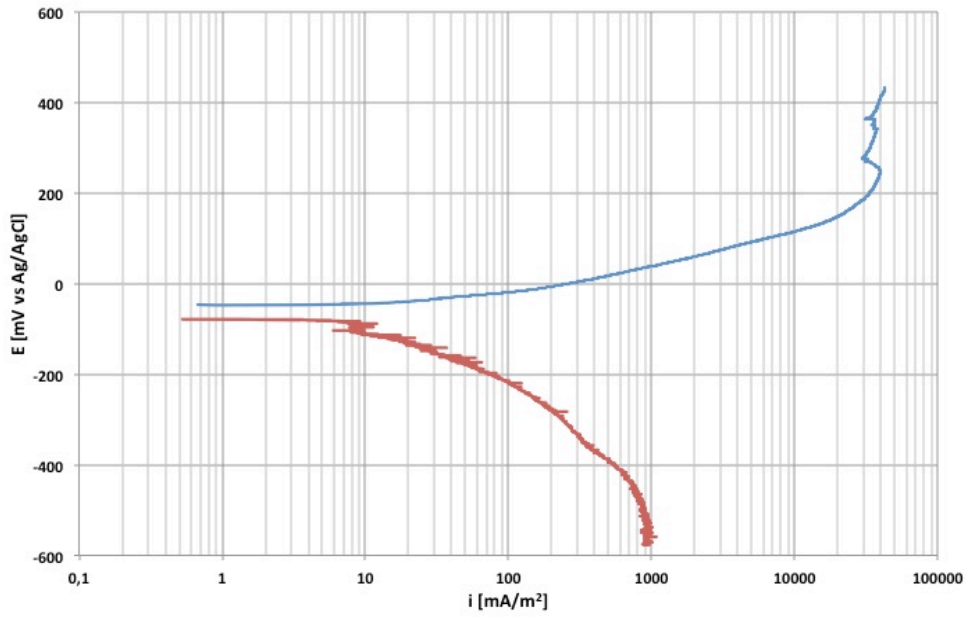
Figure D.12 Polarization curve of aged (100 ppmW S) NAB in 100 ppmW sulphide-polluted SSW without an applied MF (sample 24).
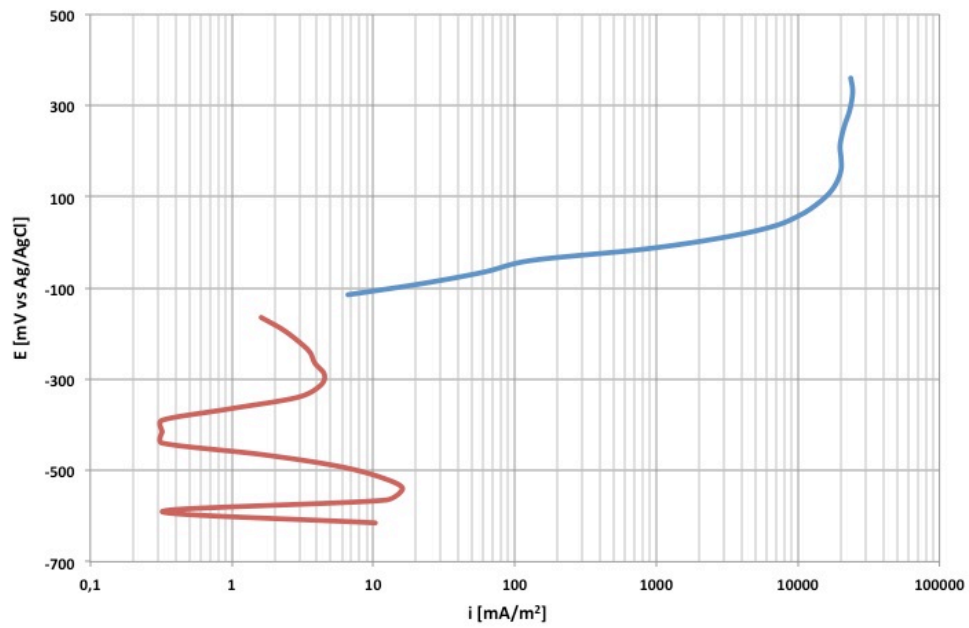
Figure D.13 Polarization curve of long-term NAB immersed in natural seawater without an applied MF (sample 28).
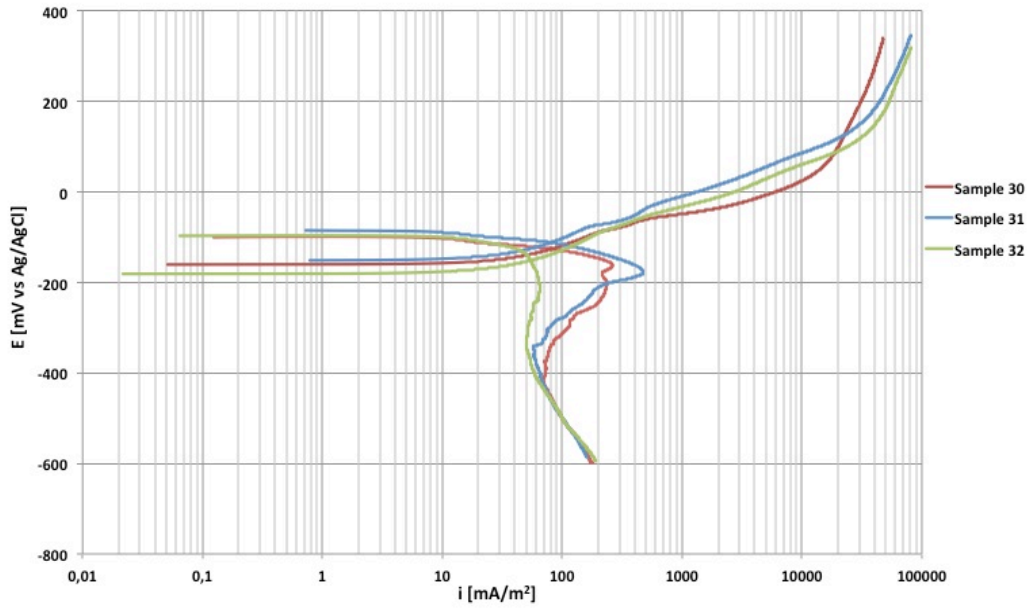
Figure D.14 Polarization curves of long-term NAB immersed in 10 ppmW sulphide-polluted SSW without an applied MF.
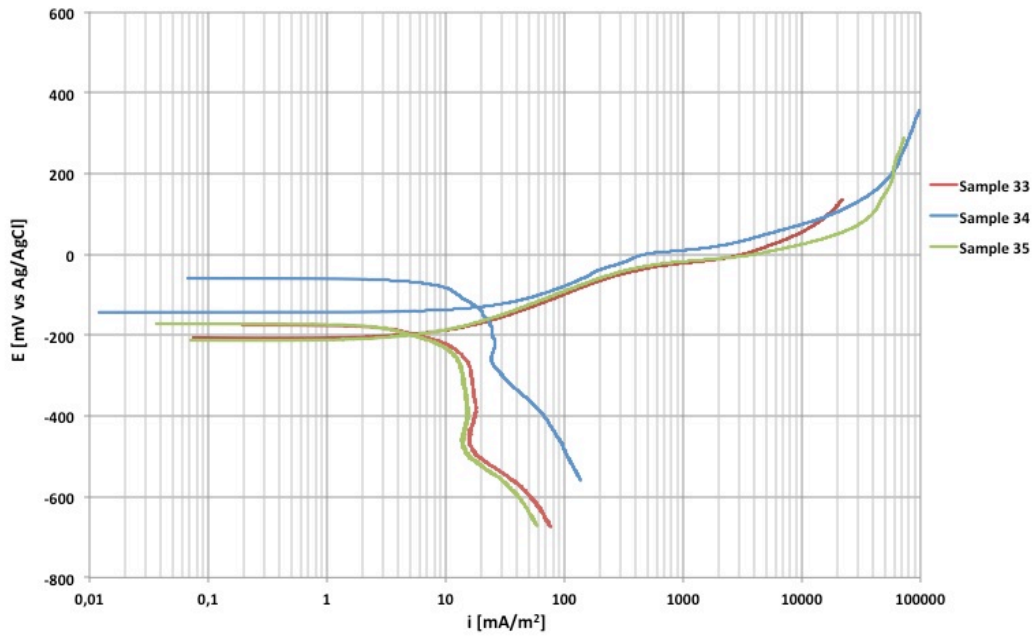
Figure D.15 Polarization curves of long-term NAB immersed in 10 ppmW sulphide-polluted SSW with an applied MF.

Appendix E LPR measurements

Figure E.1-E.8 show the LPR measurements and corresponding linear regression used to find the slope. The polarization resistance, R_p, was calculated from Equation C.2. If parallel test were performed, the LPR measurements are plotted in the same figure. The notation sample corresponds to the test matrix given in Table 3.5.
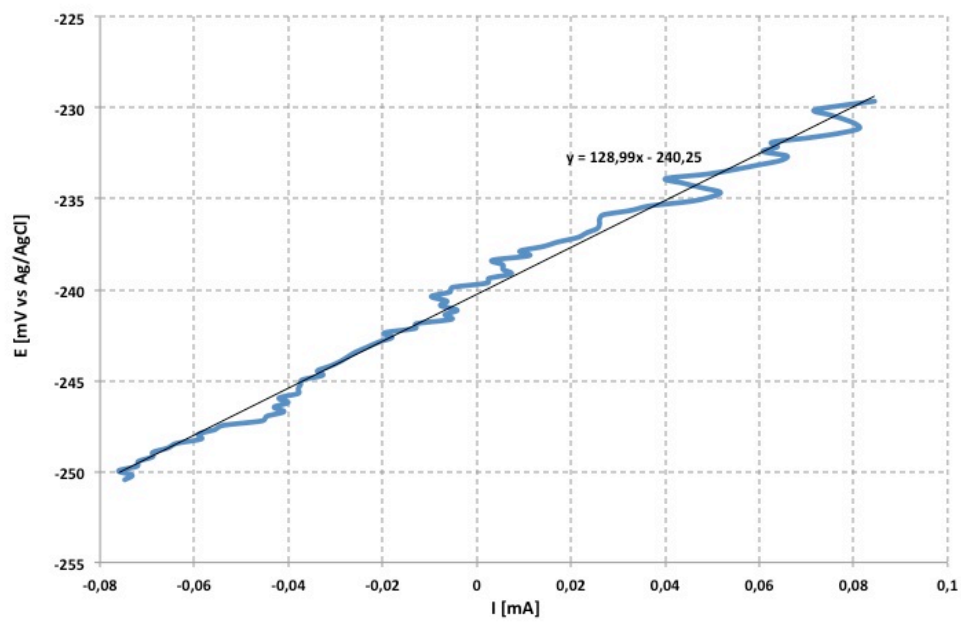
**Figure E.1 LPR measurement of fresh NAB in SSW without an applied MF (sample 1).**

Figure E.2 LPR measurements of fresh NAB in SSW with an applied MF.
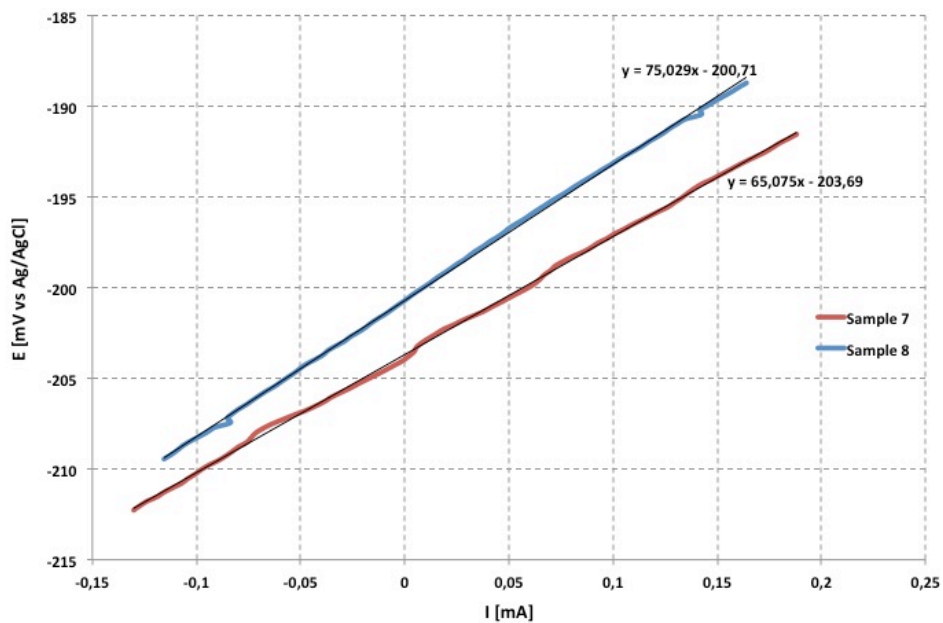
Figure E.3 LPR measurements of fresh NAB in 10 ppmW sulphide-polluted SSW without an applied MF.
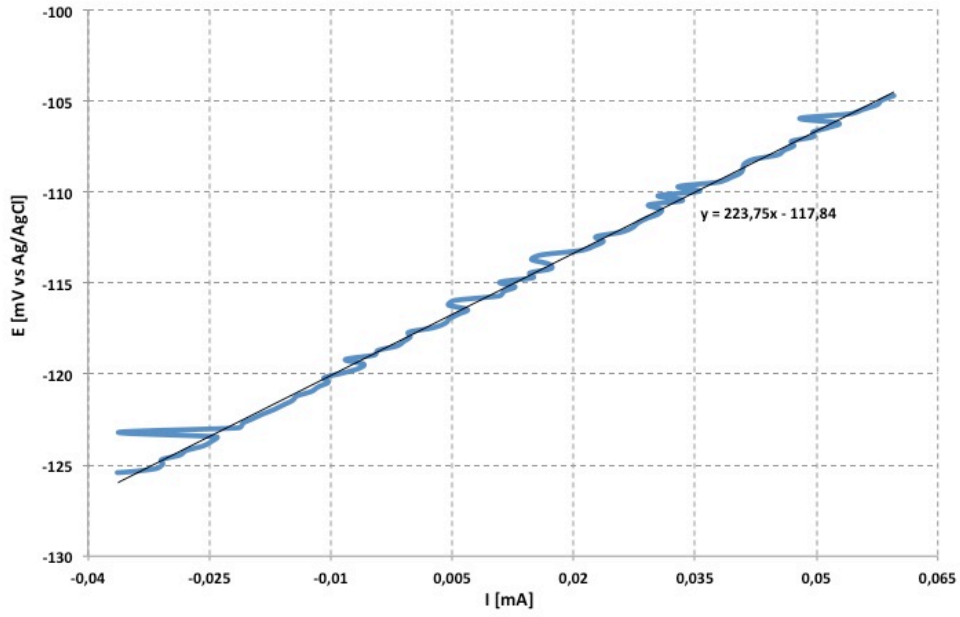
Figure E.4 LPR measurement of aged (10 ppmW S) NAB in 10 ppmW sulphide-polluted SSW without an applied MF (sample 22).
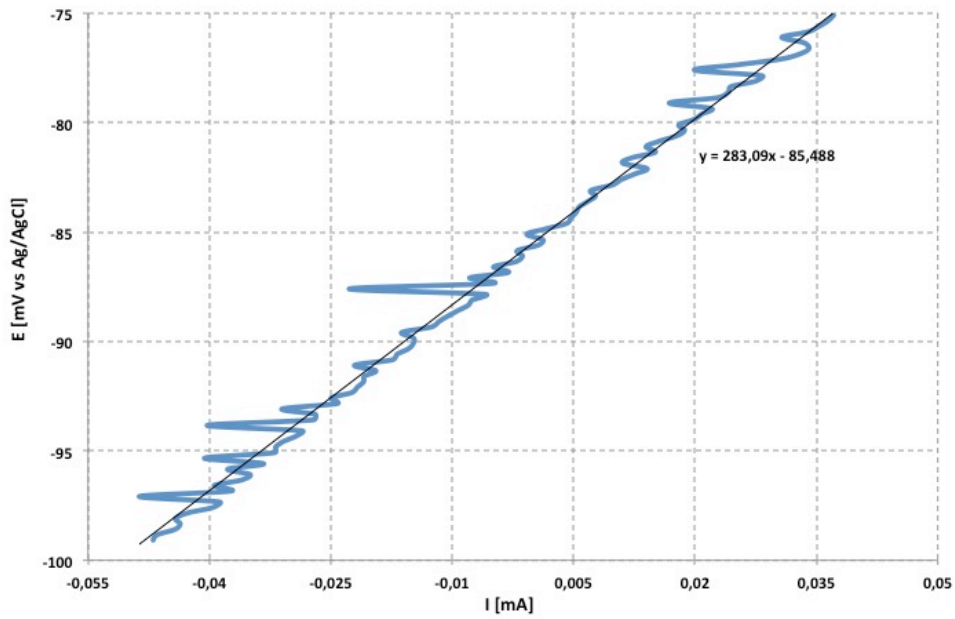
Figure E.5 LPR measurement of aged (100 ppmW S) NAB in 100 ppmW sulphide-polluted SSW without an applied MF (sample 24).

Figure E.6 LPR measurements of long-term NAB immersed in natural seawater without an applied MF.
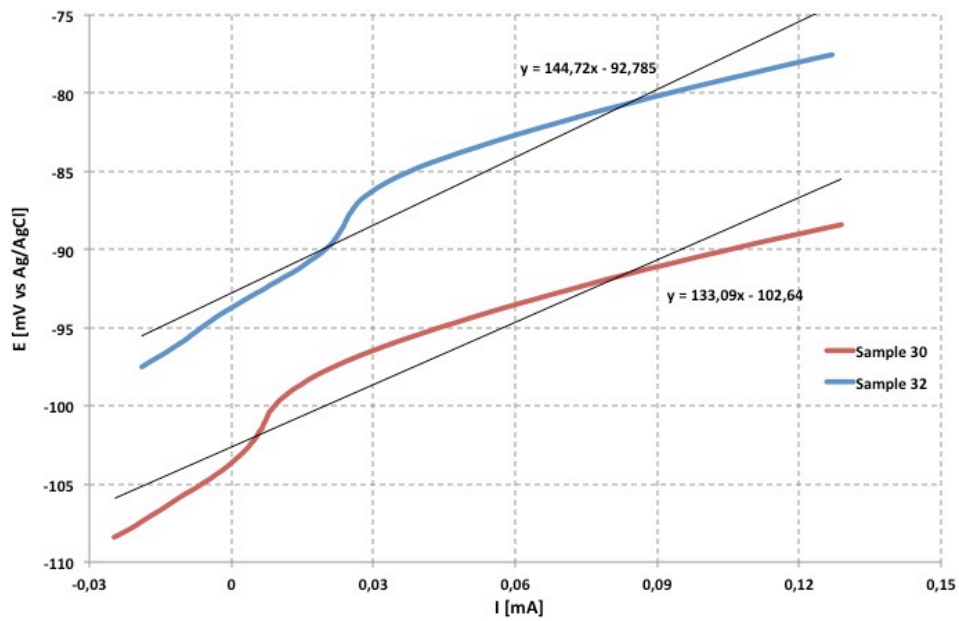
Figure E.7 LPR measurements of long-term NAB in 10 ppmW sulphide-polluted SSW without an applied MF.
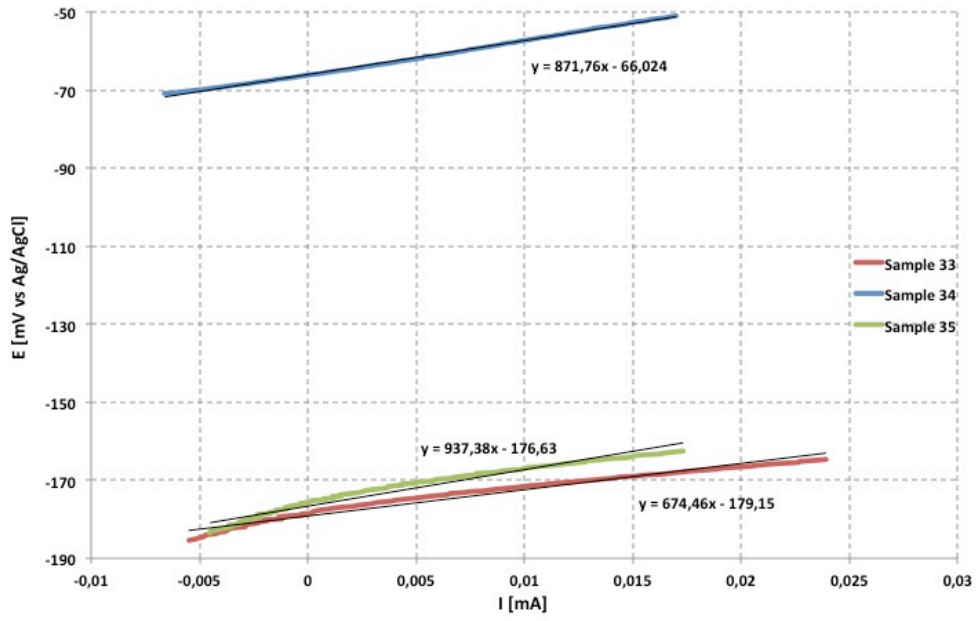
Figure E.8 LPR measurements of long-term NAB in 10 ppmW sulphide-polluted SSW with an applied MF.

Appendix F Overvoltage curves

Figure F.1-F.11 show overvoltage curves of NAB under different experimental conditions, used to calculate the Tafel slope constants, b_a and b_c, and the corrosion potential, i_{corr}. The colored curves represent the polarization curves. The black, solid lines represent the extrapolation of the linear regions of the polarization curves. The dashed line shows the corrosion potential, i_{corr}. The notation sample corresponds to the test matrix given in Table 3.5.
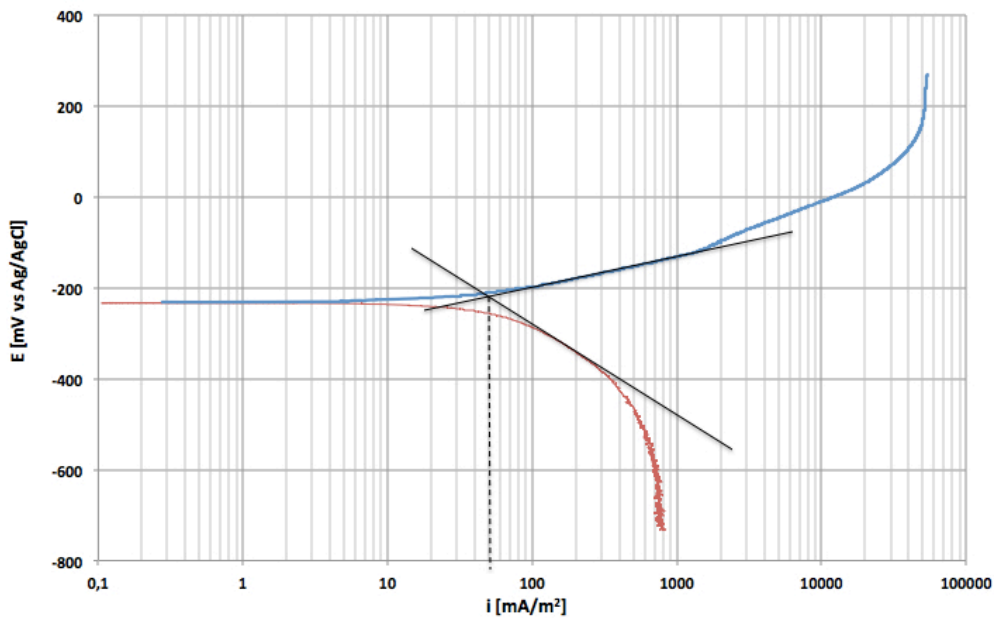
Figure F.1 Polarization- and overvoltage curves of fresh NAB in SSW with an applied MF (sample 3).
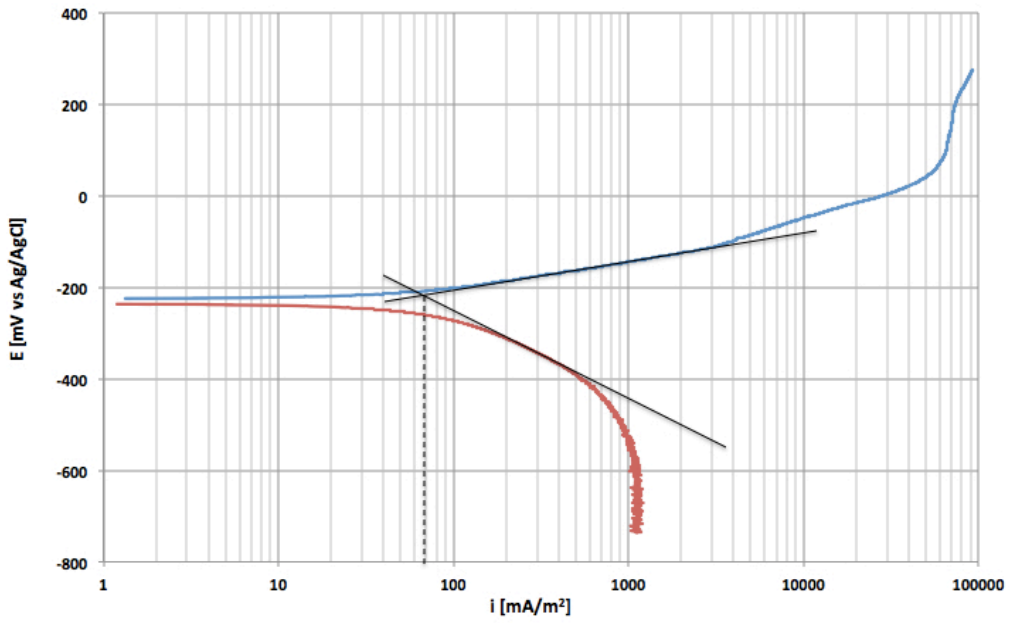
Figure F.2 Polarization- and overvoltage curves of fresh NAB in SSW with an applied MF (sample 4).
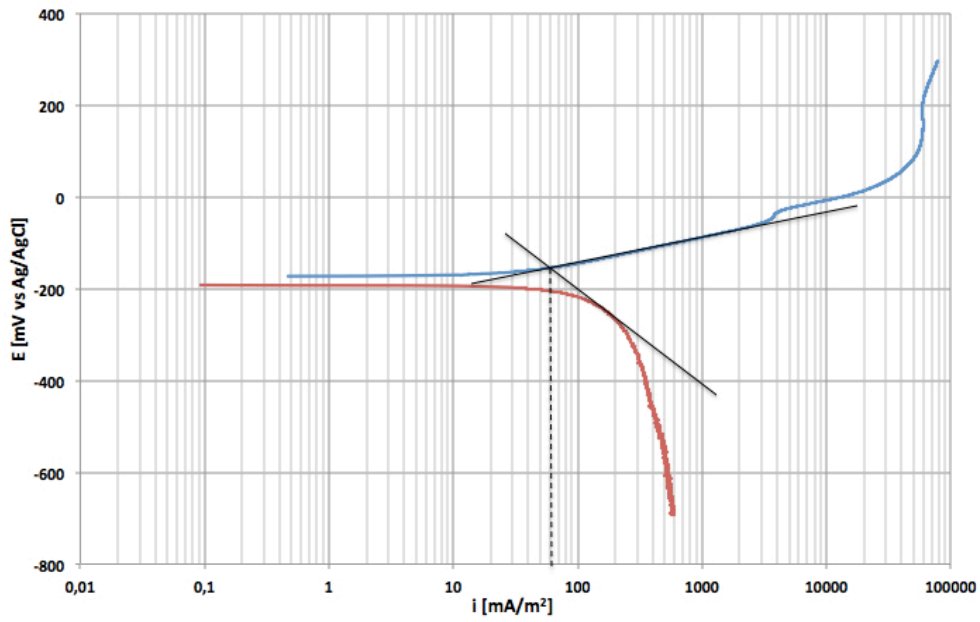
Figure F.3 Polarization- and overvoltage curves of fresh NAB in 10 ppmW sulphide-polluted SSW without an applied MF (sample 7).
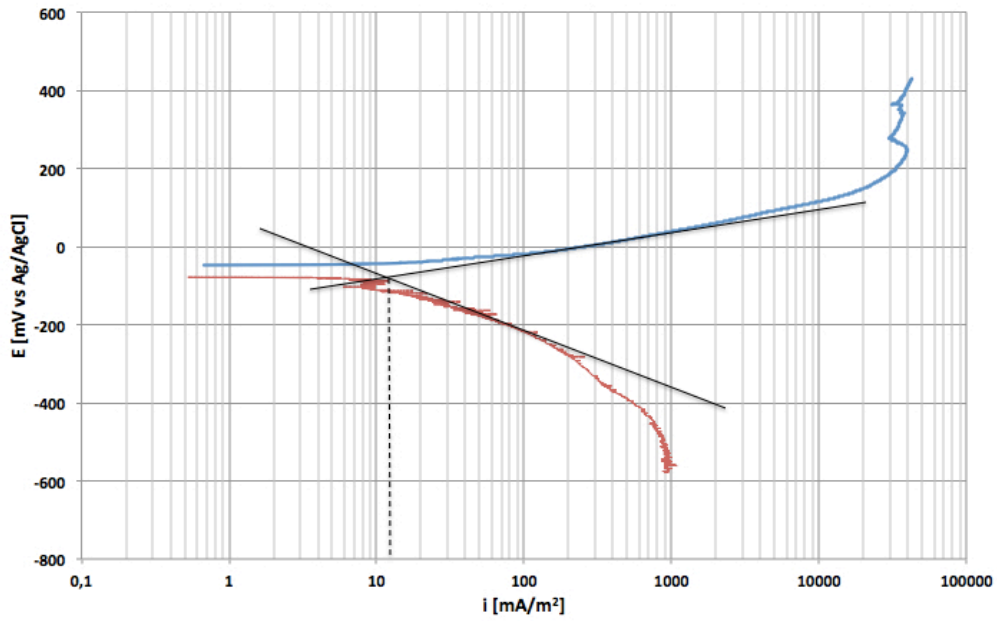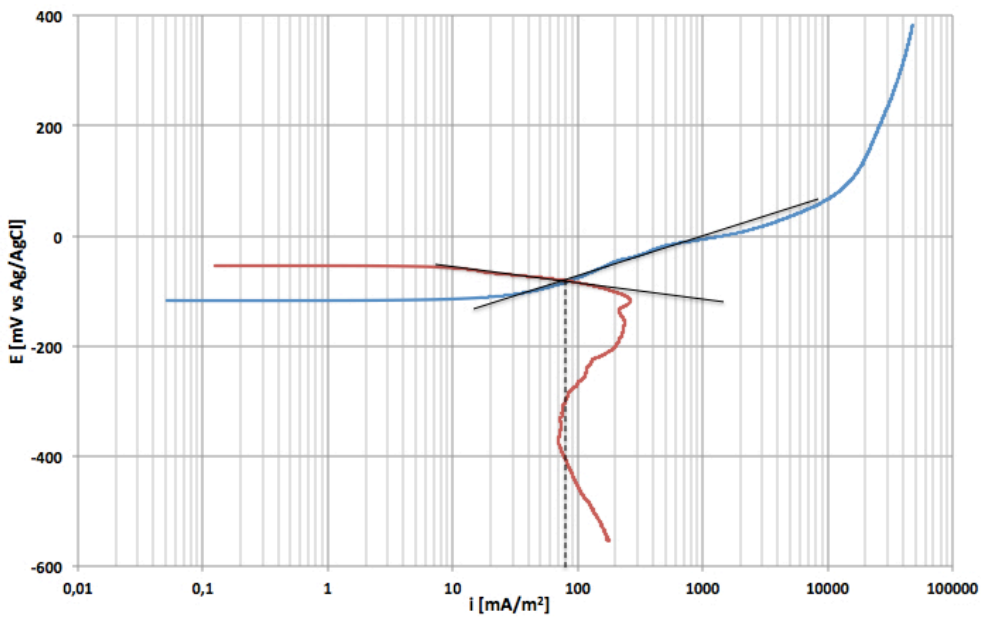
Figure F.4 Polarization- and overvoltage curves of fresh NAB in 10 ppmW sulphide-polluted SSW without an applied MF (sample 8).
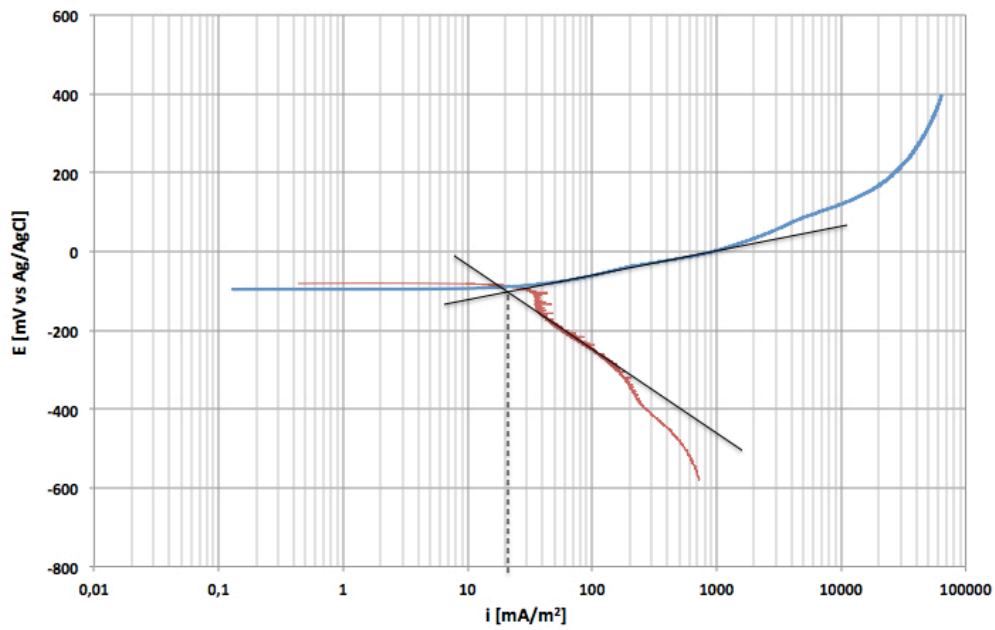
Figure F.5 Polarization- and overvoltage curves of aged (10 ppmW S) NAB in 10 ppmW sulphide-polluted SSW without an applied MF (sample 22).

Figure F.6 Polarization- and overvoltage curves of aged (100 ppmW S) NAB in 100 ppmW sulphide-polluted SSW without an applied MF (sample 24).

Figure F.7 Polarization- and overvoltage curves of long-term NAB in 10 ppmW sulphide-polluted SSW without an applied MF (sample 30).
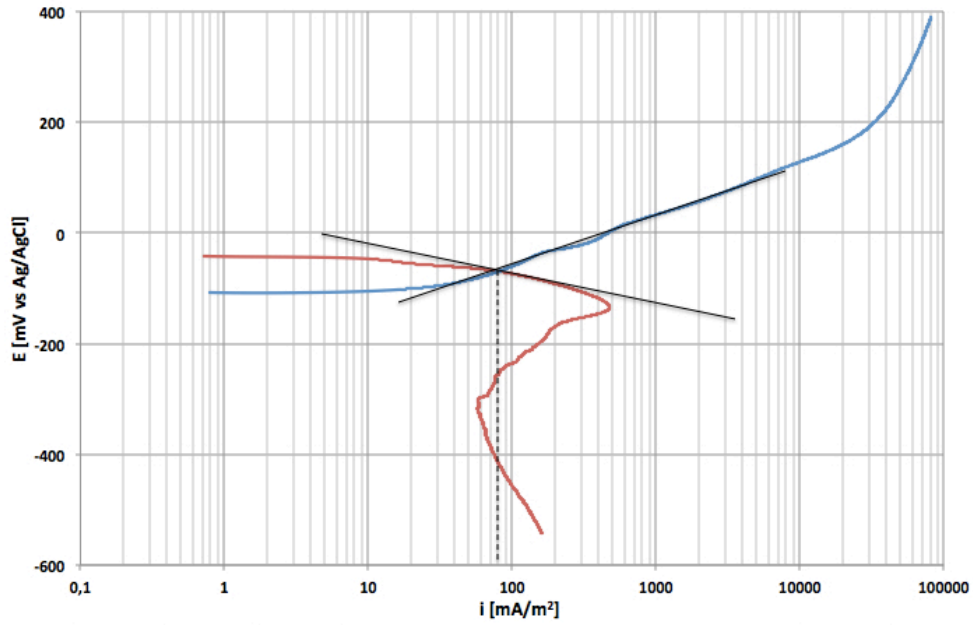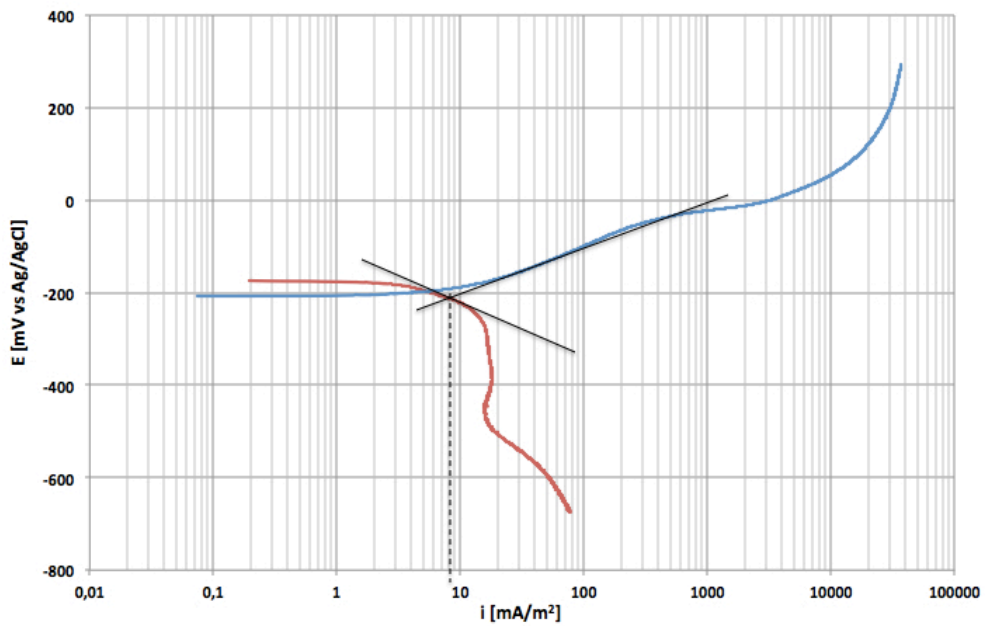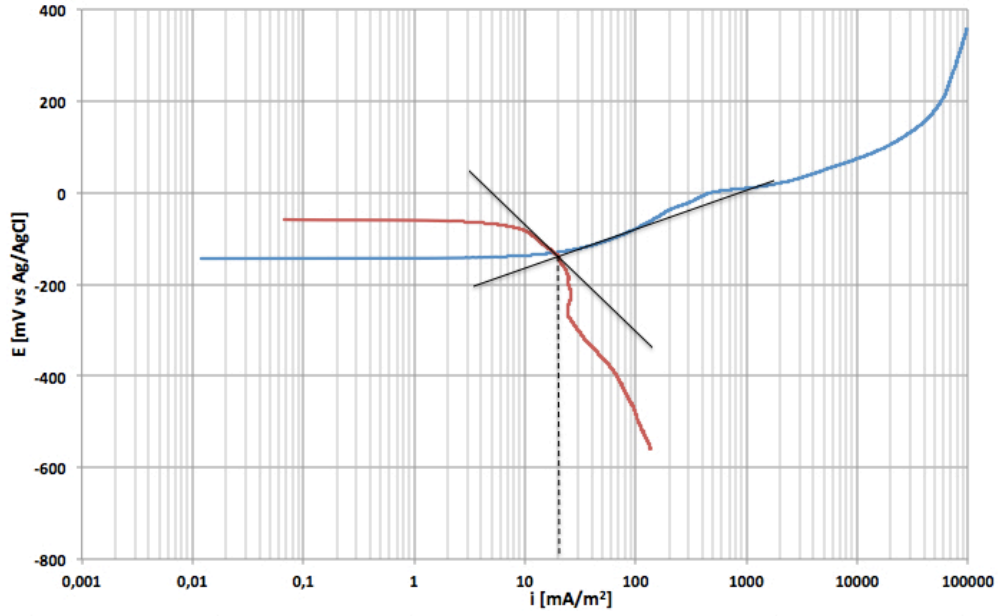
Figure F.8 Polarization- and overvoltage curves of long-term NAB in 10 ppmW sulphide-polluted SSW without an applied MF (sample 32).
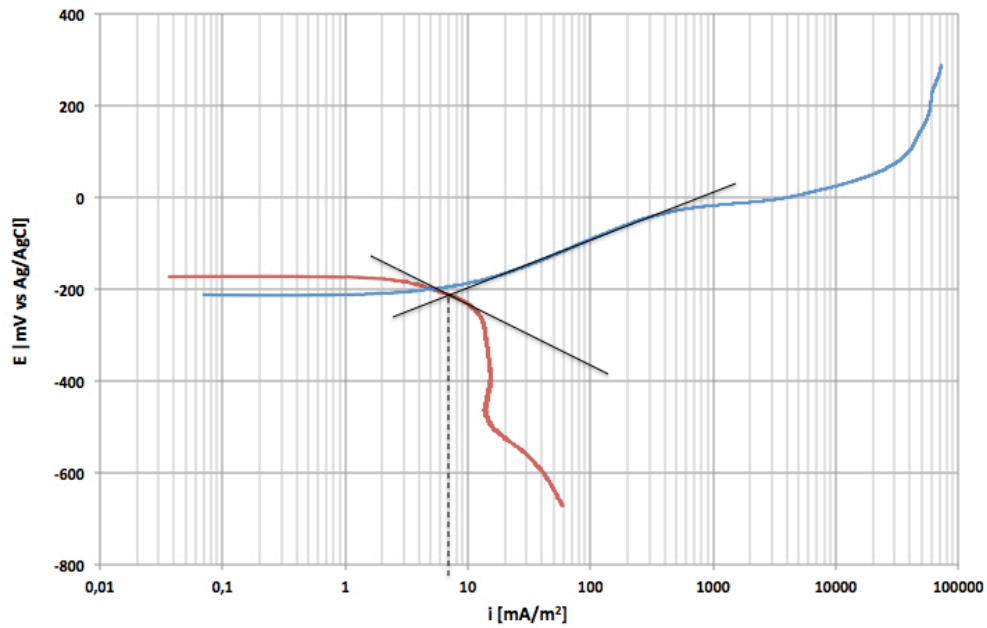

Figure F.9 Polarization- and overvoltage curves of long-term NAB in 10 ppmW sulphide-polluted SSW with an applied MF (sample 33).

Figure F.10 Polarization- and overvoltage curves of long-term NAB in 10 ppmW sulphide-polluted SSW with an applied MF (sample 34).

Figure F.11 Polarization- and overvoltage curves of long-term NAB in 10 ppmW sulphide-polluted SSW with an applied MF (sample 35).